CHARACTERISATION AND IMPROVEMENT OF THE PERFORMANCE OF A SMALL ANODE GERMANIUM WELL DETECTOR FOR ENVIRONMENTAL MEASUREMENTS

Thesis submitted in accordance with the requirements of the University of Liverpool for the degree of Doctor in Philosophy

By

OTOBONG THOMAS

May 2019

ACKNOWLEDGEMENT

Now that the final whistle has been blown to end this game and the scoreboard updated, it is time to acknowledge the efforts of persons who directly or indirectly contributed to this success story.

Firstly, I would like to thank Dr. Helen Boston for the supervision, guidance and support all the way through this research. Words are not enough to express my gratitude to Prof. Paul Nolan, for the advice and guidance from start to finish which helped in giving this work its "flavour". I would like to thank ProfEmer. Peter Appleby for providing the environmental standards for calibration of the detector and for the discussions we had. I would also like to thank Dr. Andy Boston for finding time to discuss and put me through some of the technical challenges I faced. A big thank you to Prof. Dave Joss. Dave was in the background pulling the strings to make sure this research ends well. It was Dave's idea to move on to this work when the previous suffered technical setback.

My express gratitude goes to Dr. Carl Unsworth and Dr. Dan Judson for their time and all the help. Carl was a source of intellectual excitation and inspiration to me. Thanks for always having time to accommodate my troubles.

To members of the nuclear physics group and the larger physics group, I had a good time with you all. To all my good friends, Will, Kevin, Ahmed, David, Stephen, Munerah, Ify and others not mentioned, our interactions and the encouragement made life a bit bearable while on this journey. You guys rock.

To members of Love Assembly led by Pastor Fola, who took care of my spiritual wellbeing throughout the years, a special thank you to you all. To the members of Love Assembly Football Academy who were not so happy to have me in the opposing side's defence, you can now rest, I was only on a visit and my time is spent.

A special also goes out to the Petroleum Technology Development Fund (Nigeria) for the sponsorship opportunity and to University of Port Harcourt, Nigeria for the support extended to me while studying.

I appreciate my parents and siblings for all the encouragement and prayers. To my special ones, “BEE”: my wife **B**animimbo-ofori, my princesses **E**liana, and **E**lsie, we share this success story.

The memories from Liverpool: the good, the bad and the very ugly will always be engraved in my heart. I will always cherish it as I move on to other endeavours.

Finally, “the deed is done”.

To God be the Glory.

ABSTRACT

The small anode germanium (SAGe) well detector is a HPGe detector designed with a small p+ contact at the centre of the crystal's base, while other surfaces including inside the well are surrounded by n+ contact to improve its energy resolution performance. It is useful in applications such as environmental studies and others, where small samples are routinely placed inside the detector's well for measurements. The study presented in this thesis is focused on the evaluation and characterisation of the GSW120 model SAGe well detector's performance and properties, with the view to develop and apply a background rejection algorithm, to reduce background influence on measurements carried out without shielding the detector.

Analogue electronics were used to measure the detector's noise performance, energy resolution and energy efficiency for variable sample fill height in the detector well. A comparison of energy efficiency performance of the SAGe well and a model B2825 broad energy germanium (BEGe) detector has also been made in this work for samples placed on the end cap of each detector.

Characterisation measurements were performed on the SAGe well detector using the Liverpool University automated scanning system and a fully digital data acquisition system. The detector was irradiated on its side with a highly collimated gamma-ray beam from a ^{137}Cs source while the front face was irradiated with an ^{241}Am source. The response for gamma-ray interactions at specific points in the detector was measured through coincidence trigger mode. The mean of signals at each interaction position was used to establish position dependent pulse shape information.

The geometry, electric and weighting potential of the SAGe well; the factors that determine the signal formation and signal pulse shape was simulated using the AGATA Detector Library (ADL). ADL was used to generate signal pulse from specific locations in the detector volume.

The energy resolution performance of the SAGe well is evaluated to be 0.59 keV at 47 keV, 0.62 keV at 60 keV, 0.71 keV at 122 keV and 1.77 keV at 1332 keV, etc, in good agreement with the manufacturer's measurements.

The evaluated efficiency performance of the detector shows a decreasing trend as the amount of sample is increased in the well. The best performance being with a small

amount of sample near the bottom of the well. For measurements carried out on the end cap, the BEGe detector performs better than the SAGe well at low energy and has a comparable performance at high energy. This is particularly important where large sample measurement consideration is to be made.

The charge collection times show strong variation with radius only at depths close to the p+ contact. The same effect is observed for the rise times of the signal pulses. At long radii, for depths close to the detector bottom, the pulse rise times are comparable with rise times of pulses from interactions near the top of the crystal.

The simulation results of the SAGe well electrical properties reveal that the bulk of the detector volume has weak electric potential compared to a 15 mm radius region, near the p+ contact. This is also true of the weighting potential characteristics. This has resulted in ambiguity in the position dependent signal pulse shape for interactions in the detector.

The pulse shape characteristics ambiguity has led to the conclusion that it is not feasible to implement events rejection for background reduction as proposed and as such shielding is recommended for use in sensitive measurements with the SAGe well detector.

Table of Contents

List of Tables

LIST OF FIGURES

Chapter One
INTRODUCTION

1.0 Introduction

The use of germanium-based detectors for gamma-ray spectroscopy has been in the forefront of the revolution in the advancement of nuclear physics technology. It is at the centre of many of the developments pushing the frontiers of nuclear applications. This has been made possible largely due to advances in digital electronics and the capabilities of recent data processing techniques that supports semiconductor gamma-ray detectors. One such development in germanium detector technology is the advent of well detectors, an extension to the coaxial design germanium detectors. High purity germanium (HPGe) well detectors are designed to provide maximum efficiency for small samples that are placed in the well because the sample is almost completely surrounded by active detector material. The shortcomings of the development of traditional HPGe well detectors have been an increase in the capacitance of the detector device that directly leads to increased electronic noise and loss of the detector's resolving power.

In order to improve the gamma-ray resolving power suffered by traditional well detectors, manufacturers developed detectors with electrode geometries targeted at improving this effect. One such detector is the small anode germanium (SAGe) well detector manufactured by Mirion Technologies (formerly Canberra Industries Inc). this detector uses a "point-like" geometry for one of its electrodes. This type of detector is particularly important in radioactive waste assay, environmental study, radio-isotope dating and fundamental nuclear physics. An example is the ^{210}Pb dating technique to track environmental changes over many years, using a time scale of the ^{210}Pb half-life of 22 years. This technique relies on the identification and measurement of the 47 keV gamma-ray peak from ^{210}Pb. In traditional well detectors, the identification and measurement of this low energy gamma-ray peak is limited by the detector's energy resolution that is restricted by its electrode geometry. Traditional well detectors can only look back about 150 years for ^{210}Pb dating but with more sensitive detectors, it is possible to look further back.

1.1 Motivation

In applications involving the measurement of low energy gamma-rays, the spectral quality of the full energy peak is often smeared with Compton scattered background events. This affects the sensitivity and detection capability of radiation detectors. This hampers the accurate quantification of the radioisotope present in the sample. Several works have been done in the AGATA project [Bos09, Goe13, Bru16, etc.], GERDA experiment [Var09, Ord10, Ago11] and others [Cre10, Coo11, etc.] with different degrees of success in the application of pulse shape analysis (PSA) to enhance the performance of the detectors used. The capabilities of PSA have been demonstrated in previous works as suggested above.

For measurements where the sample is placed in the well of the SAGe well detector, low energy photons will deposit all their energy near the crystal surface in the well. Background from external sources and Compton scattering will occur throughout the bulk of the crystal. It is possible to perform a selective discrimination of events through pulse shape analysis based on photon interaction position. This will improve the spectral quality of the low energy gamma-ray photopeak of interest thereby enhancing the detection and quantification of the radioisotope measured.

1.3 Thesis Overview

Characterisation and performance assessment measurements of the GSW120 model small anode germanium (SAGe) well detector have been performed. Analogue electronics were used to assess the detector's spectroscopic properties. The detector was mounted on a fully automated scanning table and scanned with a pencil beam of mono-energetic gamma-rays. Pulse shapes resulting from interactions of the gamma-ray with the detector crystal were fully digitised and analysed off-line. The measurements and analysis of the data had the following objectives:

- Evaluation of the spectroscopic performance of the SAGe well in terms of energy resolution.
- Evaluation of the SAGe well detector efficiency as a function of sample volume in the well and comparison of the absolute efficiency performance of the SAGe well to a broad energy germanium detector.

- Investigation of the signal pulse shape parameterisation as a function of interaction position.
- Simulation of the SAGe well detector electric field and pulses from single site interaction using AGATA Detector Library (ADL).
- Develop an algorithm for background event rejection using the pulse shape characterisation obtained from both experimental measurements and simulations.

Chapter Two of this thesis introduces the basic principles of radiation interaction in matter. It also gives a brief description of some fundamental principles of signal generation in solid state detectors. In Chapter Three, a brief description of the SAGe well detector is given. This is followed by a description of the processes followed and measurements performed to assess and characterise the SAGe well detector. The results of the analogue and digital measurements are presented and analysed in Chapters Four and Five. Finally, a summary of the outcome of the characterisation and performance optimisation attempt is presented in Chapter Six.

Chapter Two
BASIC PRINCIPLES OF GAMMA-RAY INTERACTIONS

2.1 Gamma-ray Interaction Mechanism

In gamma-ray spectroscopy, the detection and measurement of gamma-rays depends on their ability to interact with matter and the transfer of energy to electrons in the detector material. Gamma-rays do not directly ionise the material they are travelling through since it is massless and chargeless but rather, it interacts with an atomic electron losing some or all its energy to the electron. The excited electron moves through the detector material causing ionisation until all its energy is lost to secondary electrons.

Although, several interaction mechanisms exist, only three interaction processes are of principal importance for gamma-ray interaction in matter. These are, photoelectric absorption, Compton scattering and pair production. The relative importance of these processes in the energy range of 0 – 100 MeV as a function of atomic number is shown in Figure 2.1.

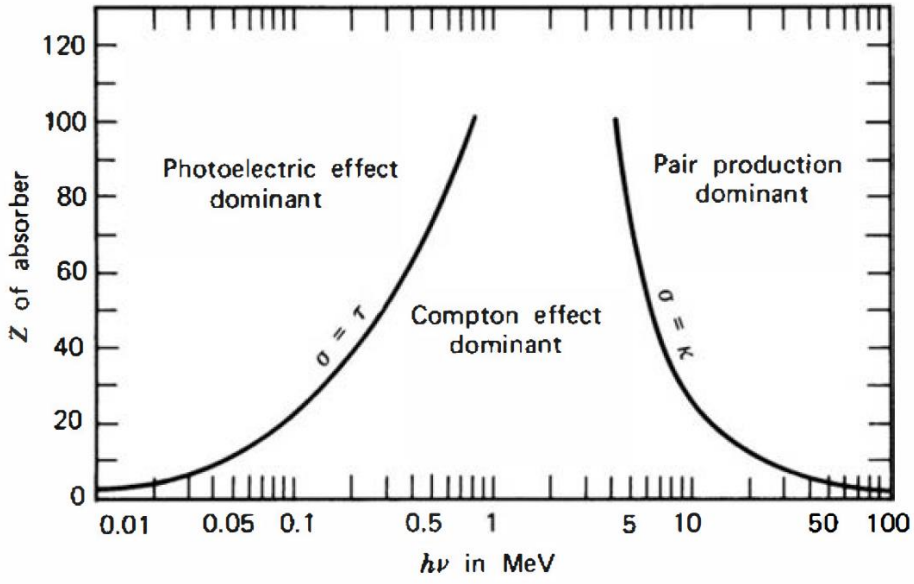

Figure 2.1: Relative importance of gamma-ray interactions due to photoelectric, Compton scattering and pair production [Kno10].

For a gamma photon of considerable energy, all these processes can come into play before the total attenuation of the gamma-ray intensity. In such a scenario, the total

attenuation, μ_{tot}, can be represented as the sum of the attenuation due to each of the interaction processes. That is,

$$\mu_{tot} = \mu_{pe} + \mu_{Cs} + \mu_{pp} \tag{2.1}$$

where, μ is the *linear attenuation coefficient* and the subscripts represent each of the interaction processes. For any material which a gamma-ray transmits through, the fraction of the photon that will interact in a given thickness, x, of the material is related to μ_{tot} by;

$$\frac{I}{I_0} = e^{-\mu_{tot}x} \tag{2.2}$$

where I_0 is the incident number of photons, I is the number of transmitted photons through the absorber material. The average distance the gamma-ray travels in the absorber before an interaction occurs called the *mean free path,* λ, can be used to characterise gamma photons. The *mean free path* is the reciprocal of the linear attenuation coefficient given by Equation 2.3.

$$\lambda = \frac{1}{\mu_{tot}} \tag{2.3}$$

2.1.1 Photoelectric Absorption

In the photoelectric absorption process, a photon disappears completely after undergoing interaction with an absorber material atom. This is shown schematically in Figure 2.2. The photon energy is transferred to an atomic electron in one of the bound shells leading to the ejection of the electron with a kinetic energy E_{e^-}, given by,

$$E_{e^-} = E_\gamma - E_b \tag{2.4}$$

where E_γ is the photon energy, E_b is the binding energy of the atomic shell. The recoil energy of the atom is negligible and therefore ignored in Equation 2.4. If the gamma-ray energy is sufficient, it is very likely that the photoelectron is ejected from the K shell of the atom. In germanium, the binding energy of this electron is 11 keV. The excited atom then de-excites either by redistribution of the excitation energy to the electrons left in the atom or by filling the vacancy with a higher energy electron.

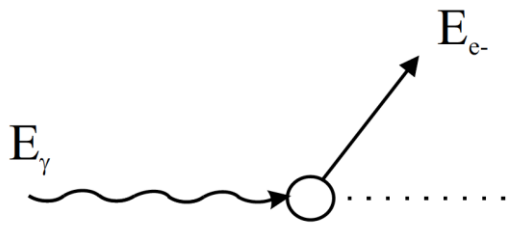

Figure 2.2: Schematic showing Photoelectric Absorption.

The redistribution of the excitation energy may result in the ejection of more electrons from the atom where a fraction of the gamma-ray energy is further transferred to the detector. In the case where a higher energy electron fills the vacancy left by the photoelectron, a characteristic X-ray is emitted. The X-ray may further undergo photoelectric absorption emitting more X-rays which are absorbed until all the energy from the gamma-ray is fully absorbed.

The probability, τ, that a gamma-ray will undergo photoelectric absorption varies with the gamma-ray energy, E_γ, and the absorber material atomic number, Z. This variation is a complicated relationship but can be expressed as;

$$\tau \propto {Z^n}/{E_\gamma^m} \tag{2.5}$$

where, n varies between 4 and 5 [Kno10] and values of 3 and 3.5 [Gil08, Dav52] has been quoted for m. The photoelectric attenuation coefficient, μ_{pe}, in Equation 2.1 can then be derived as,

$$\mu_{pe} = \tau \times \rho \times \frac{N_A}{A} \tag{2.6}$$

where ρ is the absorber material density, N_A is Avogadro's constant and A is the average atomic mass. Photoelectric absorption is the principal interaction process in germanium (see Figure 2.1, Z = 32) for gamma-ray energies below 150 keV.

2.1.2 Compton Scattering

In Compton scattering, the interaction process occurs between an electron in the absorbing material and the incident gamma photon (Figure 2.3). Only part of the incident gamma photon energy is transferred to the atomic electron. The energy, E_e, gained by the recoil electron can be expressed as:

$$E_e = hv - hv' \tag{2.7}$$

where hv is the energy of the incident photon and hv' is the energy of the scattered photon. Linear momentum conservation can be applied in Figure 2.3 to derive an expression for the energy transferred to the recoil electron in Equation 2.8 as a function of the incident gamma-ray energy and the scattering angle, θ. This expression is given as,

$$E_e = hv \left\{1 - \frac{1}{[1+hv(1-cos\theta)/m_0c^2]}\right\} \quad (2.8)$$

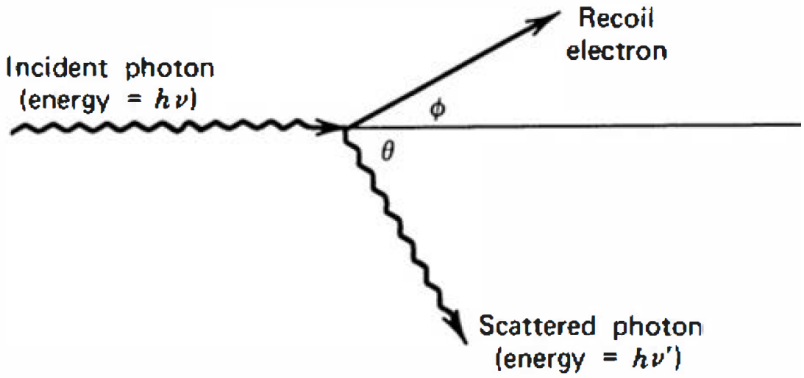

Figure 2.3: Compton Scattering of gamma photon.

where $m_0c^2$is the rest mass of the target electron in the atom. Equation 2.8 relates the transferred energy to the recoil electron and the scattering angle of the photon. If the scattering angle, $\theta = 0$, $E_e = 0$ and therefore no energy is deposited in the detector. If $\theta = 180^o$, i.e. the gamma-ray is backscattered, the term in the bracket in Equation 2.8 is less than 1 indicating that at no point would the full gamma-ray energy be transferred to the recoil electron. This presents two extremes which the energy transferred to the detector must fall between for all scattering angles.

Figure 2.4 illustrates the Compton scattering response function predicted by Equation 2.8. For all scattering angles, the absorption of the gamma-ray in the detector would always be less than 100% of the incident photon. If the binding energy of the electron is taken into account in Equation 2.8, the shape of the Compton response function alters at the maximum recoil energy as shown by the dotted line in Figure 2.4.

The probability of Compton scattering per atom of the absorber material is linearly dependent on the quantity of electrons available as target for the scattering process,

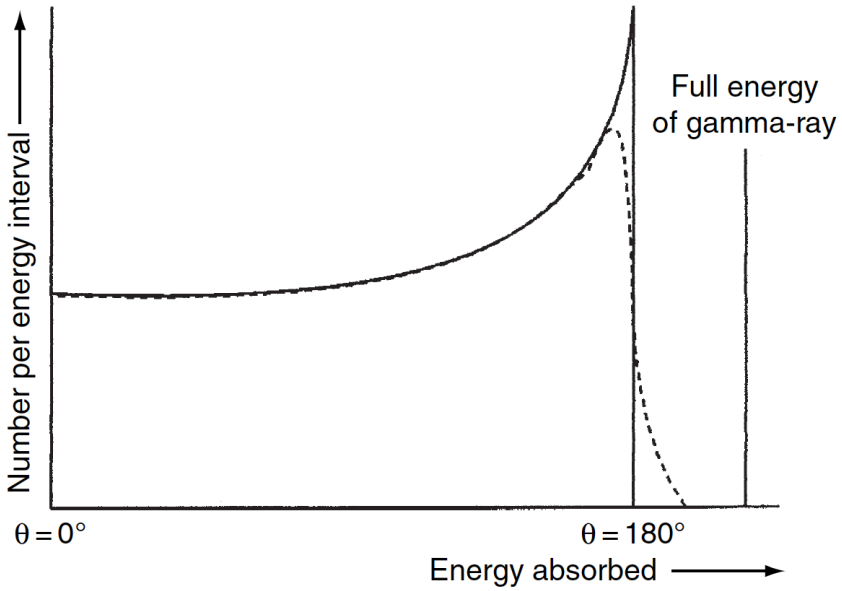

Figure 2.4: Energy transferred to an absorber by Compton scattering as a function of the photon scattering angle.

i.e., it increases as Z increases. The probability however decreases gradually with increasing energy [Kno10]. In germanium (Z = 32), Compton scattering is the dominant interaction process for gamma-ray energy range of about 200 keV to about 8 MeV as shown in Figure 2.1.

For a differential scattering cross section, $\frac{d\sigma}{d\Omega}$, the angular distribution of scattered gamma-rays is predicted by the Klein-Nishina formula to be,

$$\frac{d\sigma}{d\Omega} = Zr_0^2 \left(\frac{1}{1+\alpha(1-cos\theta)}\right)^2 \left(\frac{1+cos^2\theta}{2}\right)\left(1 + \frac{\alpha^2(1-cos\theta)^2}{(1+cos^2\theta)[1+\alpha(1-cos\theta)]}\right) \quad (2.9)$$

where $\alpha = \frac{hv}{m_0c^2}$, r_0 is the classical electron radius. The angular distribution is shown graphically in Figure 2.5. The figure illustration shows that as the gamma-ray energy increases, the probability of forward scattering increases significantly.

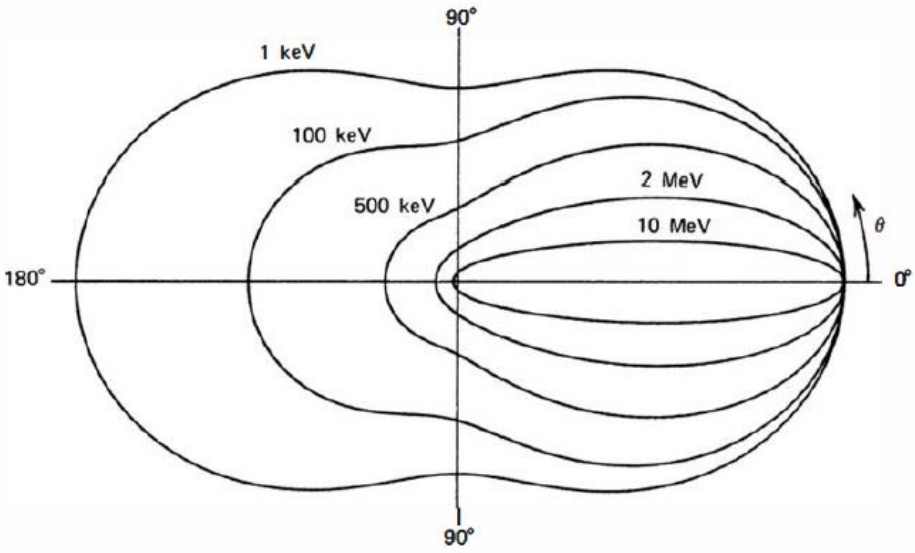

Figure 2.5: A polar plot showing the angular distribution of Compton scattered gamma-rays into a unit solid angle [Kno10].

2.1.3 Pair Production

Pair production results from the interaction of gamma-ray with the atom as a whole. The process is energetically possible if the gamma-ray energy exceeds a threshold energy twice the rest mass energy of an electron. However, pair production is unlikely to occur, or the probability of occurrence is small for gamma-ray energies just a few hundred keV above this threshold of 1.02 MeV. This interaction process must take place within the Coulomb field of a nucleus, leading to the disappearance of the gamma-ray and the creation of an electron-position pair. This pair share the excess gamma-ray energy which is the difference between the gamma-ray energy and 1.02 MeV. This shared energy is carried as the kinetic energy of the of each of the electron and positron, losing the energy to the detector medium [Gil08]. When the positron slows down to thermal energy in the absorbing medium, it meets an electron and annihilation occurs. The annihilation releases a double 511 keV photons as a secondary product of the pair production process. This process is illustrated in Figure 2.6.

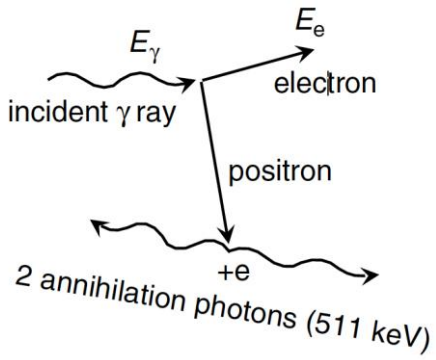

Figure 2.6: Pair production Mechanism

The magnitude of the probability of pair production per nucleus varies approximately as the atomic number of the absorber and its importance rises significantly with energy.

2.2 Semiconductors

Semiconductor materials can be classified in different ways based on certain criteria relating to their properties and applications. Criteria such as their grouping in the periodic table, magnitude of their energy band gap, electronic band structure, Crystal structure (i.e. crystalline, polycrystalline, amorphous), electronic properties are generally used to describe and understand the physics of semiconductors, [Yac04]. For example, group IV materials such as germanium and silicon are among the most important single-element semiconductors and these materials have diamond crystal structure show in Figure 2.7.

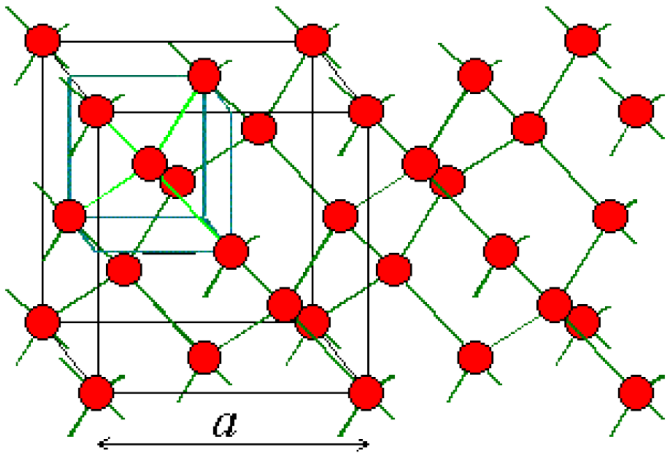

Figure 2.7: Diamond lattice structure of germanium (copyright Zeg11)

Most semiconductors used in various fields of application are in the form of bulk crystals or thin films [Yac04]. Bulk crystals are typically single crystals produced by techniques such as the Bridgman technique and the Czochralski pulling techniques. Other methods for single crystal growth exist but the Czochralski technique in its improved form is the most suitable for applications involving detector-grade material in order to have a very pure crystal. These methods of crystal growth are described by [Dha10, Uec14, Wan15, Yan15].

2.2.1 Band Structure

Electrons in the orbit of isolated atoms have discrete energy values. When these isolated atoms are brought very close, their electrons interact resulting in a combined system with electron energies slightly raised or reduced from the initial value. This forms an energy band replacing the discrete energy levels but within which there are a range of energy values.

Energy bands allowed for electrons in crystalline materials are established by the existence of well-defined periodic lattice structures in the solid. In pure materials, the energy of any of its electrons is restricted and must be confined to one of these bands [Kno10]. Outer shell electrons in crystalline materials occupy the lower energy band called the valence band. It is these outer shell electrons (valence electrons) located at specific lattice sites that determines the type of interatomic bonds. In Ge, its outer shell is half-filled with four valence electrons out of eight needed for a closed atomic shell, therefore, Ge atoms share electrons with its four nearest neighbours to form a covalent bond. Above the valence band, separated by a bandgap in insulators and semiconductors, is the conduction band. In the conduction band, electrons are free to move through the crystal contributing to the material's electrical conductivity. In conductors, the valence and conduction band overlap, therefore electrons require a small amount of energy to migrate into the conduction band. The size of the bandgap separating the valence band and conduction band is what determines if a material is classified as a semiconductor or an insulator. Insulators have bandgap typically above 5 eV [Kno10] and its electrons will require a considerably large amount of energy to cross the bandgap into the conduction band resulting in very low conductivity. The band structure of semiconductors and insulators are similar. The valence bands are

both full, but the bandgap is much smaller for semiconductors. The bandgap of semiconductors is of the order of 1 eV, similar to the energies that can be achieved by thermal excitation. The schematics of the bandgap of insulators and semiconductors is shown in Figure 2.8. In normal conditions, semiconductors have a small population of electrons in the conduction band and thereby exhibit some degree of conductivity. The probability, p, that an electron will be excited into the conduction band has a strong dependence on temperature, T. This temperature dependent probability is given by the expression,

$$p(T) \propto T^{3/2} \exp\left(-E_g/2kT\right) \tag{2.10}$$

where k is the Boltzmann constant and E_g is the energy bandgap. When the material is cooled, the number of electrons in the conduction band reduces. This in turn reduces the background current allowing for easy detection of extra excitation caused by interaction of a gamma-ray in the semiconductor detector material. This is the basis on which the semiconductor gamma-ray detector operates.

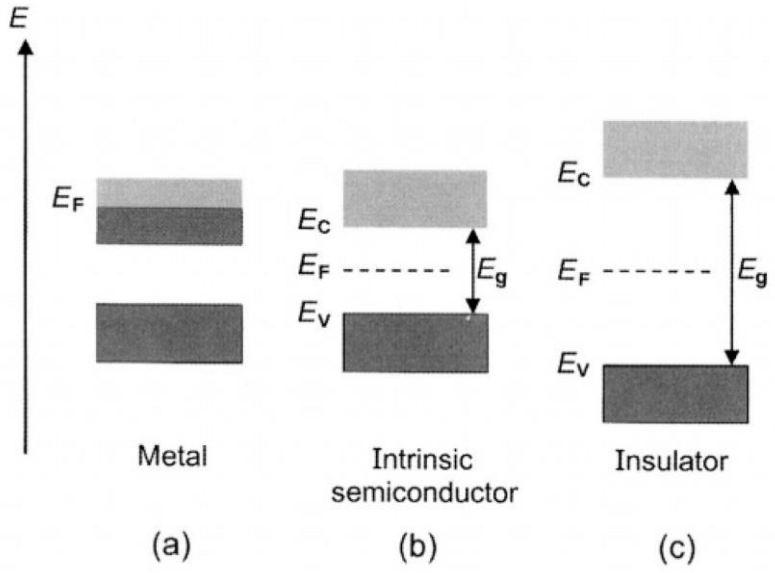

Figure 2.8: Band diagram for (a) metal, (b) an intrinsic semiconductor ($T = 0\ K$), and (c) an insulator. Darker regions represent filled bands while lighter region correspond to empty bands. The dashed lines show the Fermi level [Yac04]

2.2.2 Temperature Dependence of Energy Bandgap

An increase in temperature results in a decrease in the energy bandgap of the semiconductor. This can be explained by considering the fact that when thermal energy increases, atomic vibrations amplitude increases leading to an increase in interatomic spacing. The energy bandgap, E_g, of some semiconductor materials has been experimentally determined as a function of temperature, T, [Zeg11] as;

$$E_g(T) = E_g(0) - \frac{\alpha T^2}{T+\beta} \tag{2.11}$$

where, $E_g(0)$, α and β, are fitted parameters determined for common semiconductor materials: germanium, silicon and gallium arsenide as listed in Table 2.1. The bandgap of germanium is obtained from this temperature relationship to be $0.66\ eV$ at $300\ K$. The plot in Figure 2.9 shows the energy bandgap of germanium and silicon as a function of the temperature.

Table 2.1: Fit parameters for the determination of the energy bandgap of common semiconductor materials as a function of temperature.

	Germanium	Silicon	GaAs
$E_g(0)\ (eV)$	0.7437	1.116	1.519
$\alpha\ \left(\frac{meV}{K}\right)$	0.473	0.473	0.541
$\beta\ (K)$	235	636	204

2.3 Charge Generation Dynamics in Germanium Detectors

Electron hole pairs are created when gamma ray interacts in the active volume of the detector. The created electron hole pairs form a charge cloud whose volume is dependent on the type of radiation and magnitude of its energy. In germanium detectors, all the interactions of gamma-rays with the detector material are considered to be point-like interactions because of the short range of photoelectrons released when absorption of the photons occur irrespective of the energy. For example, a 100 keV photo-electron would have a range of 44 µm in germanium [Bru16]. Though statistically unlikely to occur, a 1 MeV photo absorption will produce photo electrons whose range in germanium is 1.2 mm.

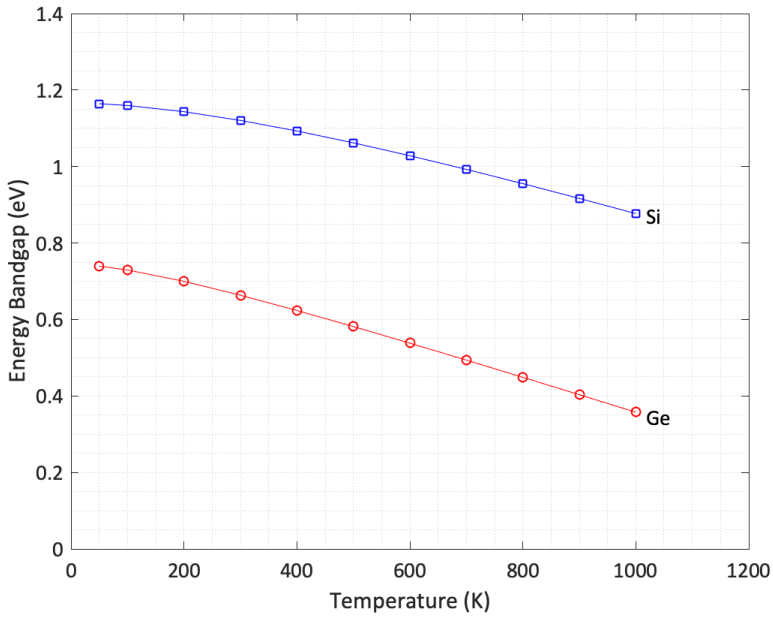

Figure 2.9: Temperature dependence of the energy bandgap of germanium (Ge) and silicon (Si).

At the instance when electron hole pairs are created, the external electric field causes a partial shielding leading to a slight delay in the separation of the electrons and holes, [Pau94]. This time delay, called plasma erosion time, τ_{pl}, given in Equation 2.12 is however negligible in large volume HPGe detectors due to their typical long charge collection times and the stopping power of photo-electrons in germanium. E_0 is the applied reverse biased field and $\frac{dE}{dx}$ is the average ionisation energy loss [Eng89] or stopping power along particle track.

$$\tau_{pl} \propto \frac{1}{E_0}\sqrt{\frac{dE}{dx}}. \tag{2.12}$$

The secondary particles generated from the ionisation of the semiconductor material by primary electrons have a direct impact on the detector performance. The ionisation energy, ϵ_{pair}, which is the average energy required to create an electron – hole pair is therefore an important parameter. For germanium and silicon at 77 K, ϵ_{pair} is 2.96 eV and 3.76 eV respectively. The average number of electron-hole pairs created per absorbed photon with energy, E, is given by,

$$\bar{N}_{pair} = \frac{E}{\epsilon_{pair}} \tag{2.13}$$

The statistical spread of the numbers of electron – hole pair does not follow simple Poisson statistics. This is because the creation of one pair is affected by the creation of other pairs. In order to describe the experimentally observed variance in the pair production, a correction factor known as the Fano Factor, F, is introduced [Fan47]. A range of this factor has been reported in the literature for germanium. In this work, the Fano Factor will be experimentally measured.

2.4 The p-n Junction

Intrinsic semiconductors are semiconductors that do not contain any impurities or defects. It is practically impossible to have such semiconductors because impurities are always left in the semiconductor intentionally or unintentionally. The type of semiconductor is therefore determined by the type of impurities (donors or acceptors) in excess in the semiconductor. Donors lose electrons to the host material while acceptors capture electrons from the host. That is donor impurities have higher valence than the atoms of the host material while acceptor impurities have lower valence than the host leading to incomplete covalent bonding in the semiconductor lattice. Semiconductors with excess donor impurities are called n-type while those with excess acceptors are called p-type semiconductors.

A p-n junction is formed when two semiconductor regions of opposite doping types are in thermodynamic contact. If this junction is formed in a single semiconductor, such is called a homojunction [Yac04]. Figure 2.10 shows a schematic of the p-n junction. The schematic illustration assumes uniformly doped p and n regions. When the contact is made forming the junction, Figure 2.10 (c), the electrons in the n-type region will migrate across into the p-type region while the holes in the p-type region migrate across the junction into the n-type region. The electrons and holes recombine as they encounter each other, thus leading to a depletion of charge carriers in the region around the junction forming a small depletion region on both sides of the junction. This results in uncompensated donors and acceptors in the n-type and p-type region respectively creating space-charge regions around the junction. There is a build-up of a potential, V_{bi}, around the junction stopping further diffusion of free charge carriers. The phenomenon produces an electric field that causes the charge carriers to drift in the opposite direction.

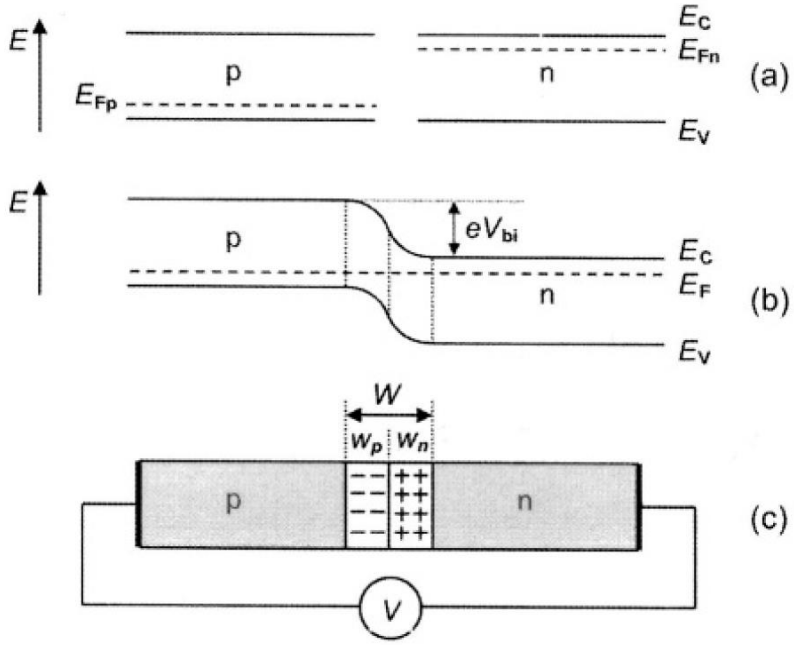

Figure 2.10: Illustration of the *p-n* junction: (a) energy diagrams of a p- and n-type semiconductor before junction formation, (b) energy diagram after junction formation (in thermal equilibrium), and (c) a p-n junction showing depletion.

The charge carriers therefore need an extra energy which can be applied externally to overcome the potential barrier in order to diffuse across the junction. If the external applied voltage is reversed biased, this widens the width of the depletion region further. The total width of the depletion region as a function of bias voltage is given by [Yac04],

$$W = \left(\frac{2\epsilon}{q}\left(\frac{N_A+N_D}{N_A N_D}\right)(V_{bias} - V_{bi})\right)^{1/2} \quad (2.14)$$

where N_A and N_D are the acceptor and donor concentration respectively while V_{bias} and V_{bi} are the reversed biased applied voltage and the built-in voltage respectively. ϵ is the dielectric constant of the medium.

The depletion region is made as large as possible to maximise the sensitivity of the region if the semiconductor p-n junction is to be used for radiation detection. In semiconductor detectors, the depletion width is extended through the full volume of the crystal by increasing the reverse bias voltage. The voltage at which the full volume is depleted is called the depletion voltage. Radiation detectors typically operate at

voltage larger than the depletion voltage to ensure that the charge drift velocity is saturated.

2.5 Electric Field

The electric field is an important area of consideration when studying solid state radiation detectors, as many detector properties depend on its configuration. In germanium detectors, the drift velocity of the charge carriers is determined by the electric field in the active volume of the detector. The understanding of the electric field configuration inside the detector is important when signal pulse properties such as shape and the timing behaviour are to be investigated. The efficiency of the charge collection process also relies on the electric field configuration.

The electric field strength varies across the active volume of a detector. This variation is dependent on the geometry of the detector and type of intrinsic region [Gil08]. For a given detector geometry, Poisson's equation given in Equation 2.14 must be solved to obtain the electric potential, φ.

$$\nabla^2\varphi = -\frac{\rho}{\epsilon} \tag{2.14}$$

where ϵ is the dielectric constant of the detector material. ρ, the charge density depends whether the detector is fabricated with a p-type or n-type material. The charge density in p-type germanium material is the product of the electronic charge and the density of the acceptor impurities.

In cylindrical coordinates, Equation 2.14 becomes

$$\frac{d\varphi^2}{dr^2} + \frac{1}{r}\frac{d\varphi}{dr} = -\frac{\rho}{\epsilon} \tag{2.15}$$

A well detector adds complexity to the formulation of a solution to the Poisson equation. A numerical solution can be found using a finite difference method [Bru16]. The AGATA Detector Library software is one of the available packages that can be used to simulate the electric field potential for germanium detectors. This is used in Chapter 5 of this work to simulate the electric field and weighting potential of the SAGe well detector.

2.6 Detector Performance Parameters

In gamma radiation interactions, gamma-rays always lose their energy to electrons and in the case of pair production, positrons. These particles will in turn lose their kinetic energies in the detector through scattering releasing secondary particles. These secondary particles are what forms the fundamentals of detector signal generation.

There are desired properties required for an ideal detector for gamma spectrometry. They can be summarised as;

- The signal output should be proportional to the deposited energy
- The detector should have good efficiency, i.e high Z.
- The charge collection process should be easy
- The energy resolution response should be good
- The operating parameters, temperature and stability over time should be good.
- It should be of reasonable cost and size.

The efficiency and energy resolution of the detector will be discussed here as this can easily be quantified.

2.6.1 Energy Resolution

Energy resolution is the outstanding characteristic of germanium detectors when they are used for gamma-ray spectroscopy. The energy resolution of germanium detectors is superior to other detectors in its ability to resolve closely spaced gamma-ray energies. The attained energy resolution of germanium detectors is determined by three factors;

- statistical distribution in the number of charge carriers produced
- charge collection efficiency and
- contributions from electronic noise.

The dominant factor of these three is dependent on the photon energy, the size and the detector's inherent quality. Typically, the full width at half maximum, ΔE, of a peak due to a monoenergetic gamma-ray can be expressed as [Kno10],

$$(\Delta E)^2 = (\Delta_C)^2 + (\Delta_s)^2 + (\Delta_N)^2 \qquad (2.16)$$

where ΔE is the value of the peak width that will be measured due to the effects of the three limiting factors mentioned above. $(\Delta_C)^2$, represents the contribution due to incomplete charge collections. This is most significant in large detectors. $(\Delta_s)^2$, represents the fluctuation in the number of charge carriers produced and is given by, $(\Delta_S)^2 = (2.355)^2 F\epsilon E$. The $(\Delta_N)^2$ term is the contribution from electronic noise. These individual terms are defined in Section 4.2.1 of this thesis. The energy resolution of the SAGe well detector used in this work has been measured and the contributing factors are assessed in Chapter four.

2.6.2 Efficiency

In gamma-ray spectroscopy, the radiation can only be measured if the detector material has the requisite properties such as high Z number in order to detect the radiation. The detector's efficiency can be assessed in different ways. The three main efficiency assessments are; Intrinsic efficiency, Absolute efficiency and relative efficiency.

- **Intrinsic efficiency, (ϵ_{int}),** is the ratio of the number of detected gamma-rays to the number of incident gamma-rays on the detector.
- **Absolute efficiency, ϵ_{abs},** is the ratio of the number of gamma-rays detected by the detector to the number emitted by the source. This efficiency has a dependency on the source detector geometry. It takes into account both the full energy and all the incomplete absorptions represented by the Compton continuum.
- **Relative efficiency:** this is defined as the ratio of the efficiency of the 1332 keV peak of any detector when the source is placed 25 cm from the detector to the efficiency of 3 x 3 inches NaI(Tl) for the same energy and distance. This can be calculated as [Gil08],

$$Relative\ efficiency = \frac{(net\ cps\ in\ 1332\ keV\ peak)\times 100}{(Bq\ of\ ^{60}Co\ at\ count\ time\ )\times 0.0012}\% \qquad (2.17)$$

2.7 Detector Preamplifiers

Preamplifiers are essential electronic components in a semiconductor detector system. In general, due to weak signals generated in semiconductor detectors, a

preamplifier must have low-noise characteristics. The signals must be amplified to be driven through the cable that connects the rest of the data processing chain. To avoid or reduce the impact of cable capacitance and other sources noise on the signal which affects the signal to noise ratio, the preamplifier must be mounted as close as possible to the detector. There are three types of preamplifier: voltage sensitive, current and charge sensitive preamplifiers. The charge-sensitive type preamplifier is generally used with semiconductor detectors [Leo94] due to the fact that the intrinsic capacitance of these detectors varies with changes in temperature. In Figure. 2.11, a simplified charge-sensitive preamplifier circuit is illustrated. The output voltage, V_{out}, can easily be calculated by,

$$V_{out} = -AV_{in} \tag{2.18}$$

where the total charge, Q, integrated on the feedback capacitor, C_F, is:

$$Q = V_{in}[C_{in} + (A+1)C_F] \tag{2.19}$$

If $A >> (C_{in} + C_F)/C_F)$ is assumed [Kno10], then, the amplitude of the output pulse is proportional to,

$$V_{out} \cong -{}^{Q}/_{C_F} \tag{2.20}$$

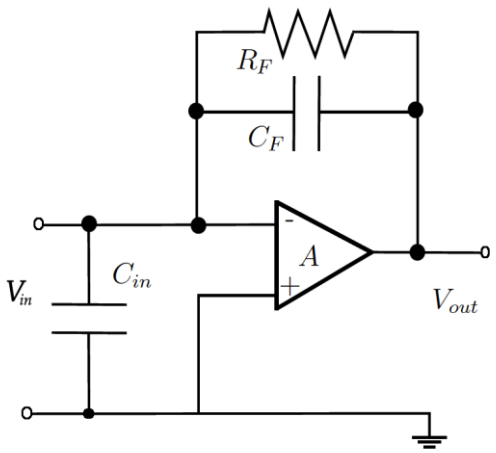

Figure 2.11: A simplified circuit diagram of a charge-sensitive preamplifier. The resistor, R_F is connected in parallel to discharge the capacitor C_F resulting in an exponential tail pulse.

Equation 2.20 shows a total dependence of the output pulse on the total integrated charge carried by the input pulse and no dependence on the detector or input capacitance. The assertion from Equation 2.20 that changes in input capacitance do not have a significant effect on the output voltage only holds as long as the time

constant, τ_c, given by the product $R_F C_F$ is long compared with the duration of the input pulse. A resistor, R_F, is connected in parallel to discharge the capacitor, C_F, resulting in a pulse signal with an exponential decay tail. The decay rate of the tail of the output pulse is determined by, τ_c. Figure 2.12 illustrates the response of a Canberra 2002c model charge sensitive preamplifier to an input test pulse. The kink on the failing edge of the output has been determined through measurement to be a function of the pulse width.

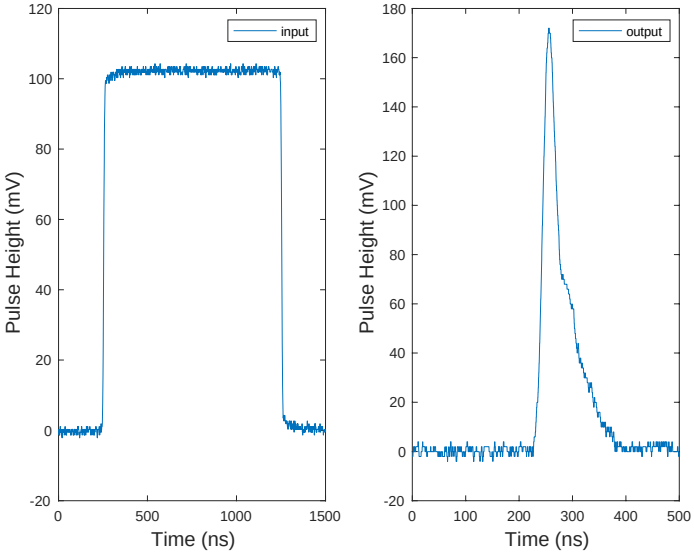

Figure 2.12: A simplified circuit diagram of a charge-sensitive preamplifier. The resistor, R_F is connected in parallel to discharge the capacitor C_F resulting in an exponential tail pulse.

2.8 Scintillation Detectors

Bismuth Germanate, (BGO) detectors were utilised in the scanning of the SAGe well detector in coincidence mode and as such it is worth to mention the properties of scintillation detectors. Generally, scintillation detectors are always coupled to photosensitive devices and amplifiers. The desired properties of scintillation detectors are:

- High efficiency for conversion of charged particles and gamma-rays into detectable light.
- The light yield should be linear and proportional to deposited energy.
- Efficient light collection. It should be transparent to its own light emission.

- It should have a short decay time for fast signal generation
- It should have good optical quality
- Its refractive index should be comparable to that of glass to permit efficient light coupling to light sensors.

BGO ($B_4Ge_3O_{12}$) has a high atomic mass and with its high density of 7.13 g/cm^3 due to bismuth (Z = 83), it is a very efficient gamma-ray absorber. BGO's are easy to handle and use due to its mechanical and chemical properties. It can be use in a rugged terrain where the fragility and hygroscopic nature of NaI(Tl) is called into question, even though it has a low light output compared to NaI(Tl).

Chapter Three

DETECTOR CHARACTERISATION METHODOLOGY

3.0 Introduction

The characterisation of a Small Anode Germanium (SAGe) well detector has been systematically performed to investigate its properties and response to photon interactions. SAGe well detectors are designed for applications such as environmental radioactivity studies, radio-bioassay, geologic and oceanographic studies [Mi16a], typically involving low activity small samples, emitting low energy radiation. A detailed understanding of the detector's properties such as energy resolution, energy efficiency, charge collection processes and the factors that affects these properties could lead to implementation of an algorithm to significantly improve its spectroscopic performance. To achieve these goals, both experimental investigation and simulation of the detector's response and performance have been carried out in the Liverpool University radiation laboratory. The measurements for the experimental investigation of the detector properties were carried out using both analogue and digital systems. This chapter covers the description of the detector configuration and features, data acquisition and analysis processes including a brief description of some of the important electronic components and features that enabled a robust assessment of the detector characteristics.

3.1 SAGe Well Detector Description and Specification

The SAGe well detector is a commercially available low capacitance germanium well detector manufactured by Mirion Technologies (formerly Canberra Industries Inc). The low capacitance associated with the detector's small anode technology translates to small capacitive noise contributions leading to an improved energy resolution. According to the manufacturer, the achieved energy resolution performance is similar to that of semi-planar detectors [Mi16b], [Mi16c] and better when compared to existing coaxial and traditional well detectors at low and medium gamma-ray energies. The SAGe well detector is a p-type elongated semi-planar detector type with a re-entrant well ("blind hole") in the front face [Ade15]. The schematic of the SAGe well showing dimensions for the model GSW120 used in this work is shown in Figure 3.1.

The entire surface area of the detector crystal is covered by the lithium-diffused n+ contact with the exception of the well and an area on the rear face of the detector. The contact inside the well was replaced during reprocessing of the detector with "a stable contact" [Ade16] by the manufacturer. The detector had an elevated background compared to ORTEC well detectors in the Liverpool laboratory. A boron-implanted p+ signal electrode (shown in red on Figure 3.1) sits on the rear of the detector surface. It covers approximately $172\ \mathrm{mm}^2$ of the rear surface area and it is physically separated from the n+ contact by a passive annular groove of about $8.5\ \mathrm{mm}$ wide (blue area in Figure 3.1). Gold and indium are used as ohmic contacts to create good physical contacts on the p+ and n+ electrodes respectively.

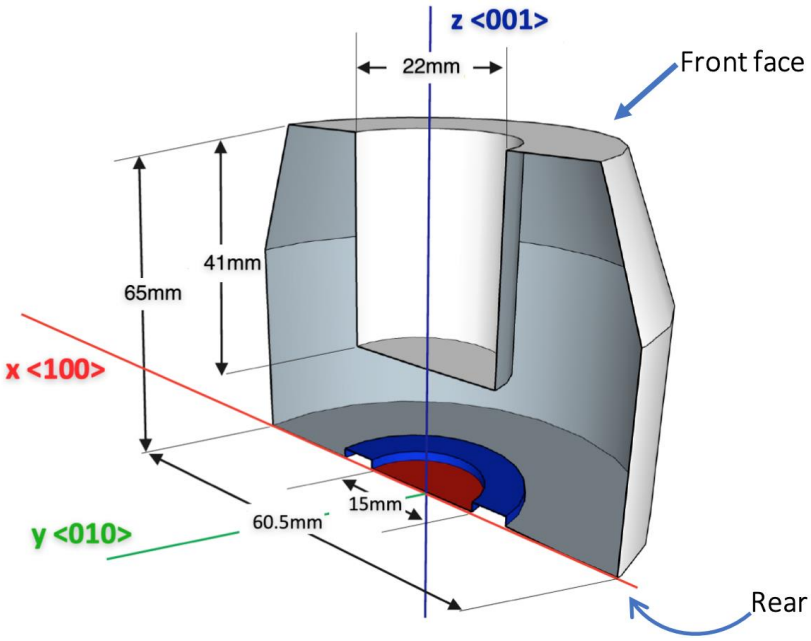

Figure 3.1: A schematic showing the physical features of the SAGe well crystal used in this work sliced along the x axis (red). The y and z axes are shown in green and blue respectively. The p+ signal electrode surface is shown on the rear face of the crystal in red and the passivated region surrounding it in blue. The remaining crystal surface area, including inside the well is covered by the n+ signal electrode crystal. (adapted from [Uns19]).

The physical properties and dimensions of the SAGe well (model GSW120) used in this work are presented in Table 3.1. The detector crystal, cooled at cryogenic temperature of $77\ \mathrm{K}$ with liquid nitrogen, LN_2, is encapsulated in vacuum within an aluminium cryostat of $82.55\ \mathrm{mm}$ end-cap diameter. The manufacturer states that the GSW120 have a minimum active volume of $120 \times 10^3\ \mathrm{mm}^3$ and it guarantees an energy

resolution performance of $0.75\ \text{keV}$ at $122\ \text{keV}$ and $2.0 - 2.2\ \text{keV}$ at $1332\ \text{keV}$ gamma-ray energy [Mi16a].

Table 3.1: Parameters and dimensions of the SAGe well detector crystal (model GSW120).

Crystal	
Type	Germanium
Length(mm)	65.32
Diameter(mm)	60.48
Well Depth(mm)*	40.80
Well Diameter(mm)*	21.60
Groove (Passive region)	
Inner Diameter(mm)	14.80
Outer Diameter(mm)	31.60
Depth(mm)	1.20
Impurities (cm^{-3})	
Front end**	2.37×10^{10}
Rear end**	2.98×10^{10}
Taper	
Length(mm)	31
Crystal diameter (mm)	reduced by $20\ \text{mm}$ on front end
Voltage (High)	
Depletion Voltage (V)	-4700
Operating Voltage (V)	-5000

* slight changes in dimension after reprocessing. **linear variation of impurity from top to bottom along z-axis is assumed.

3.2.0 Analogue Measurements

The Dewar attached to the detector upon receipt was filled with liquid nitrogen and the detector was left for 5hrs for the crystal to cool down before it was connected, powered on and measurements taken. The initial set up and measurement involves connection to, and measurements with an analogue acquisition system that consists of an ORTEC 671 spectroscopic amplifier [Ort1], an ORTEC ASPEC-927 multichannel

analyser [Ort2], a digital oscilloscope and a NIM module for HV power supply. The block diagram of this setup is shown in Figure 3.2. The detector is powered on and the high voltage bias is gradually increased to the operating voltage at a step of 100V while watching the response of the detector output signal through the digital oscilloscope. Since the detector has not been in operation since leaving the manufacturer laboratory to arriving at Liverpool laboratory, it was allowed to stabilise on full operating voltage before actual measurement commenced.

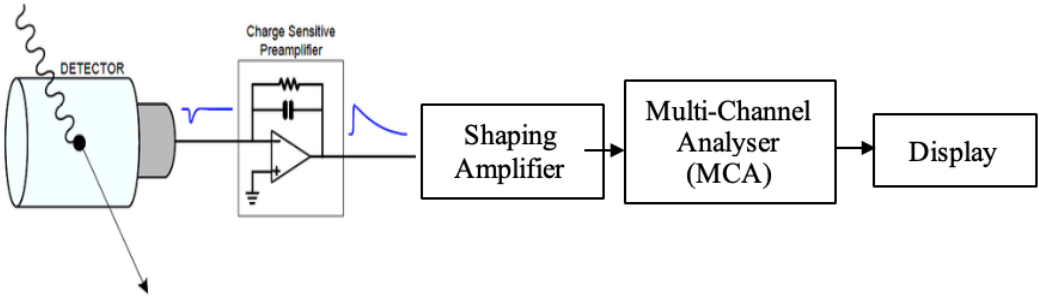

Figure 3.2: Block diagram of the analogue signal processing chain. The detector is connected to an analogue shaping amplifier.

3.2.1 Shaping Time and Preamplifier Noise Performance.

In pulse height spectroscopy, it is important to use the best practicable settings in the measurement electronics in order to obtain good results. The shaping time from the pulse processing electronics directly affects the detector resolution obtained [Kno10]. The shaping time should be longer than the rise time of the longest pulse expected from gamma-ray interactions in the detector. If the equivalent circuit time constant of the pulse processing electronics set is too short compared to the rise times of pulses from the detector, this will lead to incomplete charge collection. A compromise between the shaping time and the resolution is always reached if the detector is to be used for high count rate measurement [Gil08].

In order to determine the best amplifier shaping time for the analogue measurements, an uncollimated ^{60}Co gamma-ray source was alternately placed at the front and rear of the detector and the energy resolution of the 1.3 MeV full energy peak at different amplifier shaping times has measured. The shaping time that gave the best resolution with reduced ballistic deficit and pile-up was then used for further measurements. The

manufacturer recommended a shaping time between 4 – 10 µs for the GSW120 SAGe well detector.

Baseline noise and preamplifier gain measurement were also carried out as part of the performance pre-test of the SAGe well detector. The baseline fluctuations arise from several sources such as from external interference, electronic components, etc [Spi98]. The resultant effect of the modulation of the noise being superimposed on the signal which ultimately contributes to the detector resolution. The noise level is particularly important for low energy measurement such as in environmental applications because this affects the signal-to-noise ratio. The baseline noise, υ_{no}, is given by [Spi98]:

$$\upsilon_{no} = \upsilon_{ni}(1 + {C_D}/{C_f}) \tag{3.1}$$

where, υ_{ni} is the input noise voltage and C_D and C_f are the detector capacitance and feedback capacitance in the preamplifier circuit.

The signal-to-noise ratio of the detector can then be expressed as:

$$\frac{Q_s}{Q_{ni}} = \frac{Q_s}{C\upsilon_{ni}} \tag{3.2}$$

where, Q_s is the input signal charge, Q_{ni} is the equivalent input charge noise and C the equivalent capacitance.

The baseline noise level can be measured using a digital oscilloscope without a source present. To assess the noise level in the detector signal, the output of the charge-sensitive preamplifier was passed into a digital oscilloscope that was terminated at a high impedance of $1\mathrm{M}\Omega$. The amplitude of the baseline fluctuation was then measured directly with the oscilloscope.

The preamplifier noise performance can be assessed by first measuring the system gain. The system gain is defined as the voltage output per electron volts input [Gil08]. To determine the system gain, a pulse height from a known monoenergetic gamma-ray source is acquired by the oscilloscope. The height of this pulse of known energy is measured. The ratio of the pulse height to the energy gives the system gain, i.e.;

$$system\ gain,\ G_s = \frac{height\ of\ signal\ pulse, V_p\ (V)}{Energy, E_p\ (eV)} \tag{3.3}$$

The preamplifier noise, $FWHM_{noise}$ can then be calculated by the Equation,

$$FWHM_{noise} = 2.35 \times {}^{V_{rms}}/_{G_s} \quad (3.4)$$

where, V_{rms}, is the root mean square noise voltage at the linear amplifier output measured with the oscilloscope.

3.2.3 Detector Energy Calibration

In any spectroscopy analysis, energy calibrations must be performed with sources of known energies and activities before measurements are taken to identify and quantify a sample's radionuclide content. The interactions recorded by the multichannel analyser (MCA) must be properly calibrated into energy bins. To perform this energy calibration, uncollimated ^{241}Am and ^{152}Eu point sources were placed centrally at 10 cm from the detector endcap. The MCA gain settings through the Maestro software interface [Ort3] was adjusted such that the 1408 keV appears at about two-third of the MCA channels. The calibration was done such that the energies were binned at approximately 0.25 keV/channel.

3.3 Energy Resolution Measurement

The success of nuclear physics applications such as environmental radiometric research relies on the accurate identification and quantification of emitted radiation. In environmental studies, measurement down to the lowest possible detection limit is very important [Bri15]. Therefore, the energy resolution performance of radiation detectors used in such applications is as vital as the efficiency of the detector.

The energy resolution achieved in a germanium-based spectrometer is determined by three factors [Kno10]: statistical variations in the number of charge carriers generated, fluctuations in charge collection efficiency and contributions from electronic noise.

Gamma radioactive point sources (^{210}Pb, ^{241}Am, ^{152}Eu) emitting energies ranging from 47 keV to 1408 keV [see Appendix B for source information] were used to measure the energy resolution performance of the SAGe well detector, GSW120. The measurements were taken with individual sources positioned on the detector axis (z <001>, Figure 3.1) at a distance of 10 cm from the end-cap. An ^{152}Eu energy spectra measured with SAGe well detector is shown in Figure 3.3. The energy resolution is measured as the Full Width at Half Maximum, (FWHM) of full energy photo peak.

FWHM for gamma-rays with emission probability above 2% were considered in the measurement.

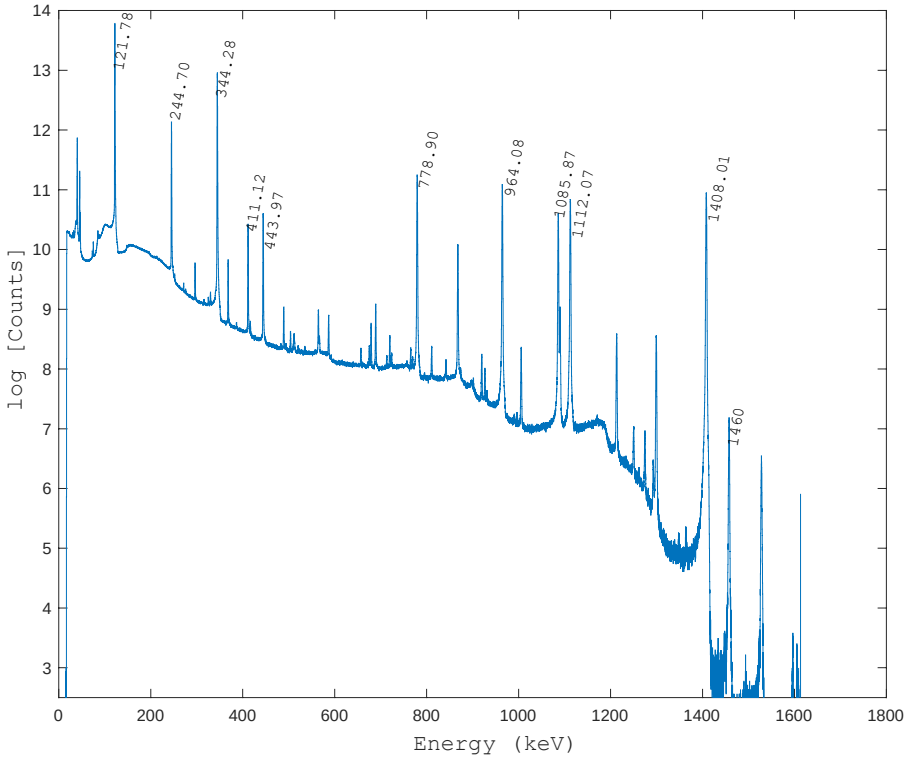

Figure 3.3: An ^{152}Eu energy spectrum measured with the GSW 120 SAGe well detector. The uncollimated point source with an activity of 119 kBq is placed centrally at a distance of 10 cm from the end-cap.

3.4 Efficiency Measurement and SAGe well Performance Assessment

The efficiency response of the SAGe well detector was determined with known samples placed inside the detector well. For the efficiency measurements, the detector was placed in a cylindrical lead cask having a lead thickness of about 10cm (Figure 3.4) in the Liverpool University Environmental Radiometric Laboratory (ERL).

Sample Description

The sample is a University of Liverpool Environmental Radioactivity Research Centre (ERRC) standard source which is a powdered mixture of radionuclides prepared by absorption of aqueous standard sources on ion exchange resin (C_4H_6) and dried at low temperature. Although, the initial radionuclide contents (^{137}Cs, ^{210}Pb, ^{241}Am, ^{60}Co, ^{109}Cd, ^{139}Ce, ^{57}Co, ^{113}Sn, ^{85}Sr, ^{88}Y) of the ERRC standard source covered a wide range of gamma-ray energies, most of these radionuclides (^{109}Cd, ^{139}Ce, ^{57}Co, ^{113}Sn, ^{85}Sr, ^{88}Y) are undetected because the source had undergone at least ten half-lives since the

sample was prepared approximately 14 years before this current investigation (see details in Appendix B).

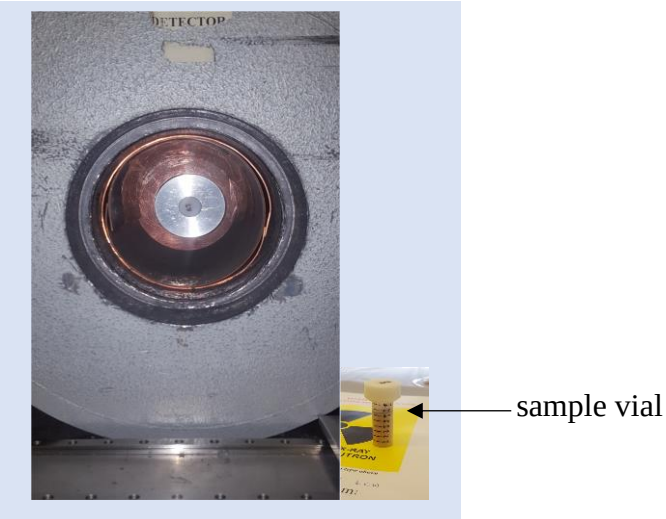

Figure 3.4: A photo of the SAGe well detector inside the lead shield in preparation for measurement in the University of Liverpool's Environmental Research Laboratory. The sample vial is shown on the side.

Calibration Activity and Detector Efficiency Determination

Six aliquots from the prepared mixture were filled in a 10 mm diameter sample vial labelled LCW1-6 to a height of 4 cm. The activities of radionuclides estimated for the LCW1 - LCW6 after comparison with other well standards are used as the ERRC calibrated well detector standards. The calibration activities in Bq/kg of these LCW well standards were dated 16th May 2003 and therefore needed activity correction. The information on calibration source radionuclide activities are in Appendices B and C.

A potential pitfall in environmental measurement with well detector samples is the significance of self-absorption of low energy gamma-ray photons within the sample [App92]. Self-absorption is accounted for by multiplying the measured counts (practical detection efficiency) by the self-absorption correction factor, f, given by,

$$f = e^{-km\mu_m} \tag{3.5}$$

where m is the mass of the sample, μ_m is the mass attenuation coefficient and k is a geometrical coefficient. The geometrical coefficient, k is related to the sample height, h, and radius, a, by the expression

$$k = \frac{0.133}{a^2}\left(h/a\right)^{-0.687}. \quad (3.6)$$

A detailed description of the derivation of the self-absorption correction factor given in Equation 3.5 can be found in [App92]. The nominal efficiency [App04] of the SAGe well defined as the detection efficiency in the absence of self-absorption is given by

$$\varepsilon(h) = \hat{\varepsilon}(h) f(h) \quad (3.7)$$

where $f(h)$ is defined in Equations 3.5 and 3.6 and $\hat{\varepsilon}(h)$ is the practical detection efficiency defined as the efficiency of the detector for a given mass of sample containing radionuclide emitting gamma-ray photons. Others, [Fur13, Bel15 and Iur18] have further suggested other methods for self-shielding correction in cylindrical samples in well-type detectors. Some of these suggestions are based only on simulations.

Efficiency variation with sample height

The same procedure described above is taken to determine the efficiency characteristics of the SAGe well as a function of sample height in the well. In this measurement, another set of sample aliquots in 10 mm diameter sample vials labelled LCWA1 - LCWA8 filled to a height of 4 cm each were prepared. The mass of these samples was measured to an accuracy of 1/1000th of a gram with a digital weighing scale. Measurement of counts were taken for each of the sample aliquots for 24 hours. A mean count rate of the 8 sample aliquots was formed from the self-absorption corrected count rates of each of the aliquots.

The ratio of individual radionuclide count rate in each aliquot and the mean count rate was used to determine and select sample aliquots based on the consistency of its ^{210}Pb, ^{241}Am and ^{137}Cs content. The aliquots with minor variation in the selection criteria (LCWA1, LCWA4, LCWA5 and LCWA7) were used to investigate the detector efficiency-height characterisation.

The selected aliquots were turned into a beaker and thoroughly mixed with a spatula. Dividing the total activities of the selected sample aliquots by its total mass yields the specific activity in Bq/kg. To investigate the effect of sample fill height on detection efficiency of the SAGe well detector, a 16 mm diameter sample vial of known mass

was prepared and used for the measurement. For each fill height, Figure 3.5, the sample was weighed, and the activity calculated by taking the product of the mass and the specific activity of the selected aliquots. The sample holder was placed in the detector well and counts taken for 24 hrs. The sample fill height with its corresponding sample mass used to determine the efficiency – height performance assessment of the detector for different energies are given in Table C3 (Appendix C).

Figure 3.5: A cross section of the SAGe well detector crystal (blue) with various height of the sample (purple) in the well. The corresponding weight of each height is indicated.

3.5 Detector Efficiency Simulation with MCNP

The SAGe well detector efficiency response was simulated using the Monte Carlo N-Particle (MCNP) transport code. First the detector and sample geometry were modelled with the MCNP5 version. The manufacturer provided very basic information

on the detector dimensions in Table 3.1 and constituent materials. This was used for the MCNP input for the detector geometry model. The modelled SAGe well detector viewed with the visual editor provided in the MCNP5 package is shown in Figure 3.6. The sample matrix material was modelled as C_4H_6 as suggested by the Coordinator of ERRC that prepared the sample. A cylindrical volume source was then used to simulate the SAGe well efficiency response. The efficiency was obtained from the pulse height distribution tally (F8 tally) score [Wer17]. The GSW SAGe well MCNP simulation script is presented in Appendix D.

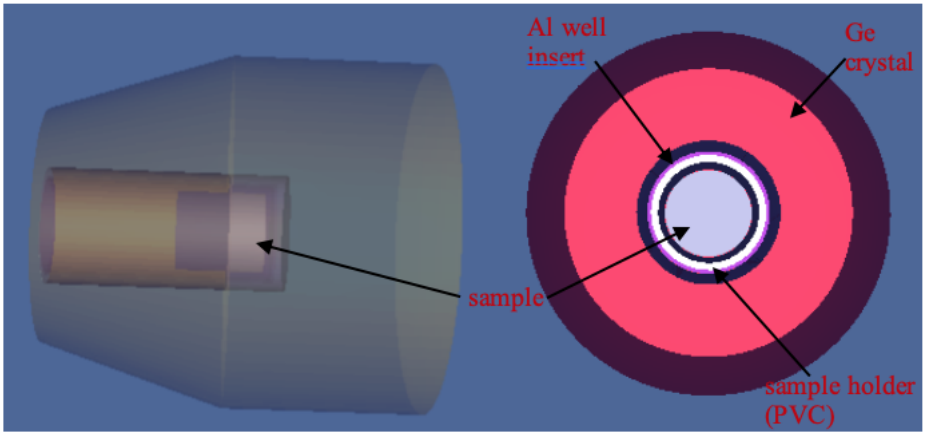

Figure 3.6: MCNP model of the GSW120 SAGe detector geometry used for efficiency simulation. The side view geometry is made transparent to show the sample inside the well. The efficiency is simulated with various sample heights inside the well.

3.6 SAGe well Efficiency Comparison with a BEGe detector

The measured absolute efficiency of the SAGe well detector has been compared to that of a broad energy germanium (BEGe) detector. The BEGe detector BE2825 model was used for this comparison. This BEGe detector has a crystal thickness of 25 mm. This means that the thickest crystal section of the SAGe well is about 2.5 times the size of the BEGe. The measurement was done with a 4 cm diameter sample holder placed on the detector endcap. The sample holder was filled with a different mass of the sample for each measurement done, Figure 3.7. This enables a direct assessment of the efficiency performance of both detectors when measurements are performed with samples placed on the endcap of the detector.

The measured absolute efficiency of the BEGe detector has also been compared to measurements done inside the GSW120 detector well.

The importance of such a comparison is necessary given that environmental samples range in sizes. Therefore, the correct detector should be selected for the measurement of a given sample.

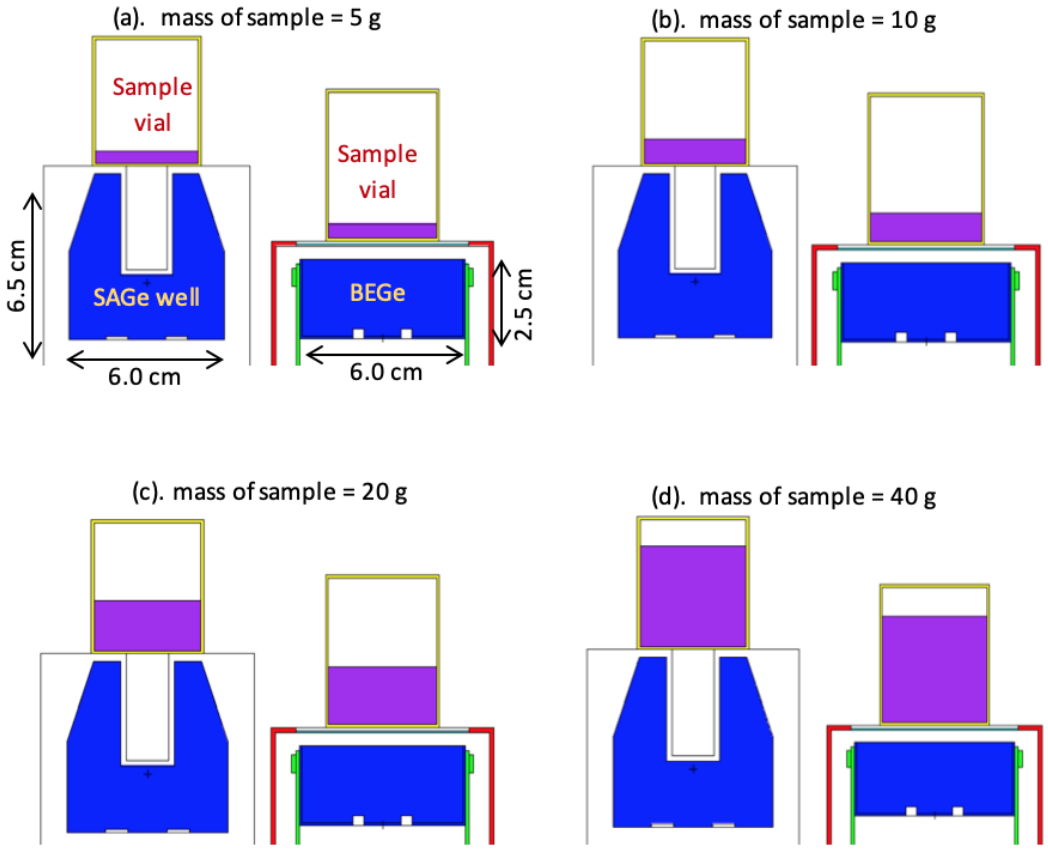

Figure 3.7: A cross section of the SAGe well and BEGe detectors showing different masses of samples placed on the top (front face) for each set of measurement done to compare each detector's relative performance. The geometry and the relative sizes of both detectors is shown in the diagram. The sample on each of the detector is shown in purple.

3.7 Bias Voltage Investigation

The bias voltage and electric field directly affect the charge collection process in the detector. The pulse height from fully absorbed radiation within the depletion layer of a semiconductor detector will rise with applied voltage where the bias voltage and electric field is low [Kno10]. The charge carriers created are either trapped or recombined along its tracks leading to incomplete charge collection due to the low detector bias and electric field. As the electric field increases, the fraction of charge

collected increases. The charge collection is completed with the pulse height reaching its maximum at a sufficiently high electric field with no further variation when the bias voltage is increased.

Anomalous spectroscopic response has been reported [Var09, Ago11, Har14] within a small voltage range below the depletion voltage in BEGe detectors. These reports prompted the investigation of the SAGe well detector's spectroscopic response at different bias voltage.

Measurements with ^{241}Am and ^{137}Cs radioactive sources have been made to investigate how the peak position, energy resolution (FWHM) and the count rate is affected by the bias voltage. By increasing the bias voltage from $500\ \mathrm{V}$ to $5000\ \mathrm{V}$ in steps of $100\ \mathrm{V}$, the of 60 keV and 662 keV (from ^{241}Am and ^{137}Cs respectively) energy spectra for each voltage increment were acquired, stored and analysed using MASETRO-32 [Ort3].

For peak centroid position shift, uncalibrated energy spectra were used for both energies measured. Using the peak centroid position for the fully biased detector at $-5\ \mathrm{kV}$ as a reference peak position, the shift in peak centroid position, $\Delta P(\%)$, as the bias voltage varied was calculated using

$$\Delta P(\%) = \frac{P_{5000} - P_V}{P_{5000}} \times 100 \tag{3.8}$$

where P_{5000} is the peak centroid position measured when the detector is biased at its operating voltage of $-5\ \mathrm{kV}$ and P_V, the peak centroid position at biased voltage V.

The effect of varying the bias voltage on the energy resolution (FWHM%) and count rate was investigated with calibrated energy spectra of the ^{241}Am and ^{137}Cs peaks.

3.8 Digital Measurements

The pulses from the preamplifier were digitised to enable the investigation of pulse shape from interactions in the detector volume. There are several advantages of digitising the detector signal over analogue measurements. Whereas analogue measurements can be used to determine the energy of the interacting radiation, detector resolution, energy efficiency and timing information, no spatial interaction information is available through these measurements. Signal pulse digitisation delivers huge benefits compared to the analogue approach. The benefits are [Ca13];

- enhanced stability and reproducibility
- system can be reprogrammed, and algorithm tailored to specific application
- information of the signal along the entire acquisition chain is preserved
- better correction of baseline fluctuation, pile-up, ballistic deficit, etc.
- it is flexible and all processes are performed in a single board.

3.8.1 Digital Acquisition System

The output signal from the preamplifier is an analogue waveform that has to be transformed into a digital dataset for processing. The digital acquisition system (DAQ) that is used in this work is a CAEN v1724 waveform digitiser. It is a 14-bit, 100MS/s waveform digitiser having an 8-channel VME module and optical readout [Ca13]. A block diagram showing the digital pulse acquisition chain is shown in Figure 3.8.

The digitiser is an acquisition system with no or negligible dead-time. The analogue signal from the charge sensitive preamplifier is fed to the input of the digitiser module. The signal is continuously sampled at a rate of $100\ \mathrm{MS/s}$ by a flash analogue to digital converter (flash ADC) to transform from an analogue to digital (A/D) data stream. The digital data stream is held in an on-board First-in/First-out (FIFO) memory buffer. This translates to $10\ \mathrm{ns}$ sample size with a 14 bit precision. The digitised signal is processed

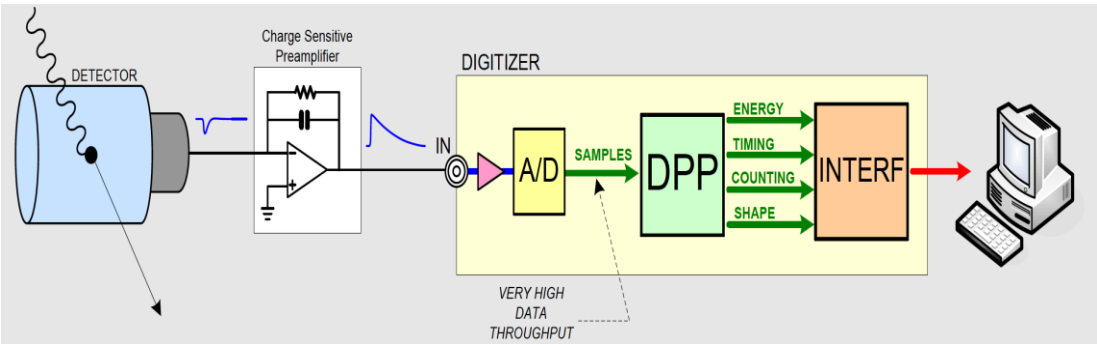

Figure 3.8: Block diagram of a digitiser-based spectroscopy system [Ca13]. Analogue to digital (A/D) conversion is done at the input of the digitiser. A field programmable gate array (FPGA) performs an online digital pulse processing (DPP) to extract information from digitised signals.

on-line by the field programmable gate array (FPGA) and also stored for off-line processing. The FPGA is a programmable logic device with characteristics such as configurable logic blocks, configurable interconnections, configurable input/output

blocks, RAM, etc. The on-line digital pulse processing (DPP) is performed in the FPGA by applying filters and algorithms to perform digital pulse height analysis (DPHA) for energy calculation, extraction of baseline and time stamp etc. The filters programmed into and implemented inside the FPGA whose layout is shown in Figure 3.9 includes the following;

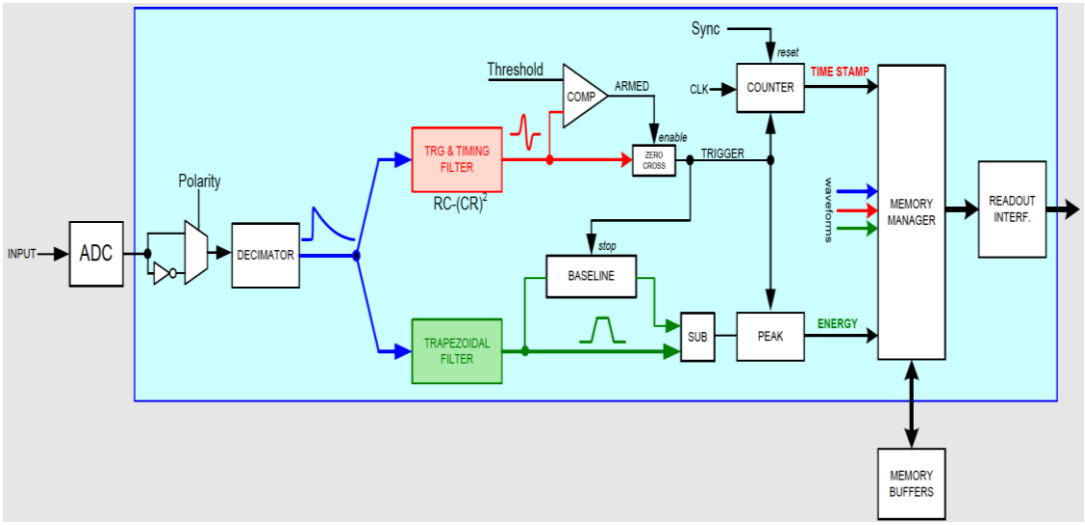

Figure 3.9: Block Diagram showing the processing chain and the filters that are programmed into and implemented inside digitiser's FPGA.

- decimation
- trigger and timing filters
- trapezoidal filter
- Baseline restorer
- Pile-up rejector and live time correction

Decimation is applied in the case where the signal is slow in order to scale down the sampling frequency by a factor of 2, 4, or 8. Since the output signal from the Canberra 2002c model charge sensitive preamplifier attached to the GWS120 detector has a fast leading edge with a long exponential tail [Can04], no decimation filter is applied for the data acquisition and therefore, the decimator is set to 0 for this characterisation work.

A trigger is generated by the trigger and timing filter (TTF) once the input signal is identified. The TTF also calculates a time stamp for the identified signal. Once a trigger signal is received, the sampling process is paused, and the content of the FIFO memory

is written to disk for storage and off-line processing. The trace length written for each signal in this experiment is 1024 samples (i.e. ~ 10 µs in length). In the digitiser registry, a pre-trigger value is set such that the rising edge of the signal was centred in the 1024 sample range.

The trapezoidal filter (Energy filter) also known as the Moving Window Deconvolution (MWD) performs the energy calculation by transforming the digitised input signal into a trapezoidal shaped signal. The difference between the trapezoid baseline and the flat top is proportional to the energy deposited in the detector. A detailed description of the operations of the digitiser and the functions of individual filters can be found in the digital pulse height analyser user manual [Ca13].

Apart from the MWD energy calculations, the energy can be derived from a simple subtraction of the charge pulse average baseline from the pulse height, a method called baseline difference (BLD). In this work, the average baseline is calculated by taking the mean of 250 samples from samples number 50 – 300 on the acquisition window corresponding to 0.5 µs to 3 µs region of the signal trace. Similarly, the pulse height is also calculated by taking the mean of 250 samples from sample number 600 to 800 corresponding to 6 µs to 8.5 µs region on the signal trace. The BLD energy is the difference between these two averages. To check the validity of both energy calculation methods, gain-matched energy spectrum of ^{152}Eu from both methods are compared in this work.

3.8.2 Detector Scanning Method

The University of Liverpool detector characterisation system is used to acquire the data employed to evaluate the pulse shape information of the SAGe well detector. The system consists of a 1 GBq ^{137}Cs radioactive source that is mounted inside a large block of lead, Pb, with a 160 mm long tungsten, W, collimator having an outer diameter of 10 mm and an inner diameter forming a 1 mm hole ensuring that the emission from the isotropic source is collimated into a 1 mm pencil beam. This is mounted on an automated linear stepper motor that can be moved in two dimensions to a precision of 0.1 mm. The scanning system assembly is combined with the digital acquisition system described in section 3.8.1 to capture and analyse charge signals online or

offline. This setup allows for the investigation of a detector's position-dependent response by probing the crystal with the 662 keV collimated gamma-rays [Dim09].

There are two modes in which the scanning system can be operated: singles or coincidence mode. Both modes of operation work on the same fundamental principle for data acquisition but with differences in the way the system is triggered. The digitiser is set to trigger on receipt of a signal from the SAGe well in the singles mode whereas, in coincidence mode, the system is set to trigger when a signal is received from the BGO.

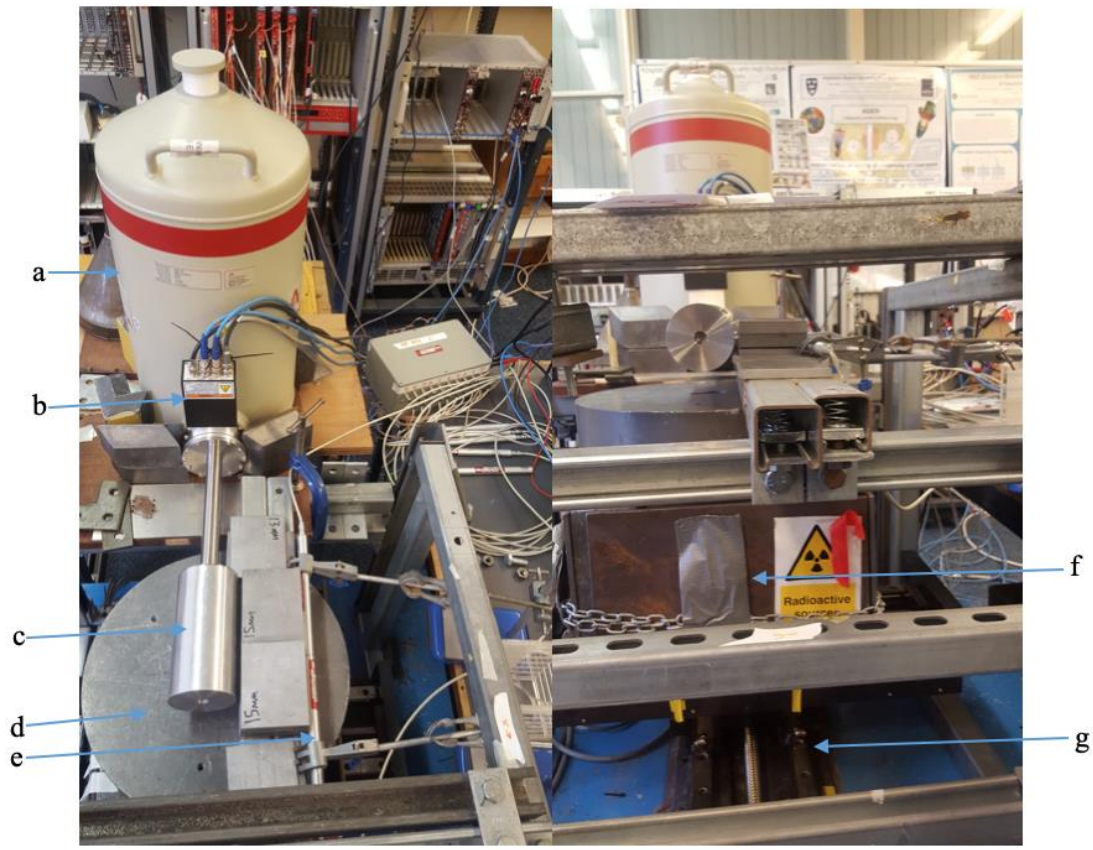

Figure 3.10: Top and side view of the SAGe well detector mounted on the Liverpool University scanning system assembly for singles and coincidence scanning of the SAGe well detector. (a) LN_2 Dewar, (b) preamplifier, (c) Al cryostat housing Ge crystal, (d) Collimated Pb block, (e) BGO for coincidence setup, (f) Pb block housing 1 Gb ^{137}Cs and (g) automated linear stepper motor. See Figure 3.11 for a schematic example of a valid event that deposits approximately 374 keV energy in the Ge detector and 288 keV in the BGO.

3.8.3 Singles Scan Method

In the singles scan mode of operation, the collimated gamma-ray beam is moved by the stepper motor along a predefined 2-dimensional format across the whole detector allowing for a front face or side scan of the detector. The information on the collimated beam position is obtained from the linear stepper motor, therefore, allowing for the identification of the xy position of the first interaction of the gamma-

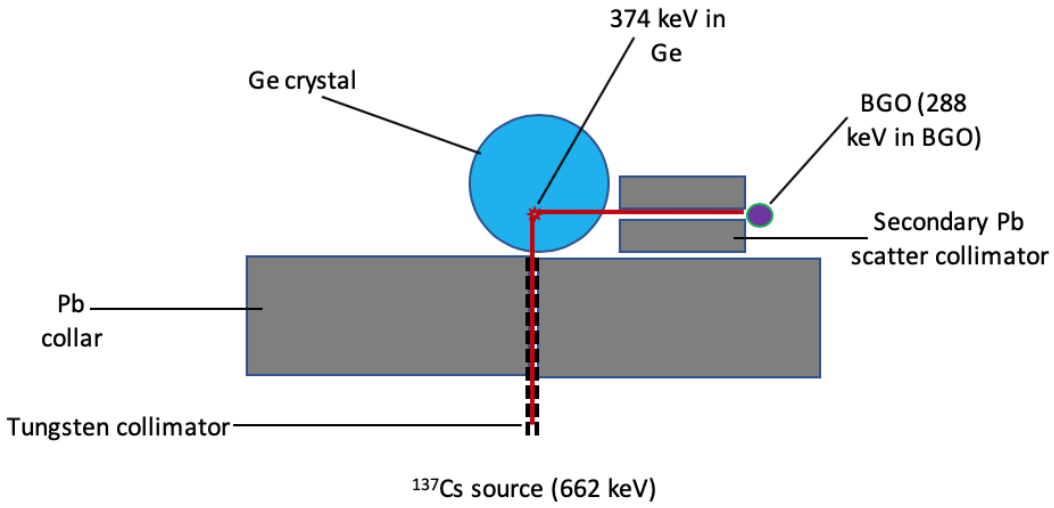

Figure 3.11: A schematic of the scanning table setup shown in Figure 3.10. The source, Pb collar and primary collimator are moved by the stepper motor in x-y direction. In coincidence mode, the red line indicates an example path of a 90° Compton scattered gamma-ray to the BGO.

ray. Localisation of the gamma-ray interaction position in the detector is not possible in the singles scan mode since no information on the z direction can be obtained and also no determination on the number of interactions that occurred before full energy deposition is available. Although this mode is limited on the positional information of the interaction position, the position, shape and orientation of the detector crystal with respect to the scanning system spatial frame can still be established from the singles scan data.

3.8.4 Coincidence Scan Method

In addition to the setup described in section 3.8.3, a secondary set of collimators in conjunction with Bismuth Germanate (BGO) detectors is used to provide spatial constraints in the measurement (Figure 3.10 and 3.11). The secondary collimator is formed by two sets of lead blocks of thickness 30 mm separated by plastic spacers to

form a 1.5 mm gap between them. The gap is lined with two BGO scintillation detectors placed head to head with each other (see Figure 3.10 and 3.11) to form a single line of BGO covering the length of the SAGe well detector cryostat. This setup ensures that only 90^o Compton scattered gamma-rays through the secondary collimation would be identified in one of the BGO detectors at a defined z direction. The digitising electronics are configured such that it is only triggered when gamma-ray interactions occur in the BGO detectors. All events in which interactions occurred in both the BGO and SAGe well detectors within a $150\ ns$ coincidence time window are read out and stored. The localisation of single-site interaction positions in three-dimensions is obtained by the combination the BGO detector and the primary beam position.

A mean is formed from the signals recorded for each position in order to enhance the detector response information by reducing the effect of random electronic noise on the data. The rate of coincident interactions is always less than 2% for a 100 events per minute coincidence trigger rate [Uns19] but this rate also varies with position. Due to the low rate of occurrence of 662 keV Compton scattered coincidence events, it is time consuming to perform online data processing and analyses. The data acquired from the coincidence scan measurement is therefore sorted and analysed offline.

For a fixed gamma-ray energy, scattering interactions allow for a fixed amount of energy to be transferred for each scattering angle [Gil08]. In the case of the 662 keV gamma-ray used to irradiate the SAGe well detector, at 90^o scatter, only 374 keV energy is deposited in the Germanium detector and 288 keV is scattered out and deposited in one of the BGO detectors (Figure 3.11). All the events captured in both the BGO and SAGe well detector are shown in Figure 3.12. In order to reduce the number of signals written out and stored, an energy filter is applied on the data to only extract signals that have energy range of 340 keV to 400 keV in the SAGe well detector and 220 keV to 350 keV in the BGOs. This is the region enclosed by the red box in Figure 3.12. The 90^o Compton scattered events deposited energy in both the SAGe well and BGO lies within this region. During offline signal processing, all interaction events with energies $374 \pm 4\ \mathrm{keV}$ in the SAGe well with corresponding energies of $288 \pm 30\ \mathrm{keV}$ in the BGO are extracted and used for the analyses in this work.

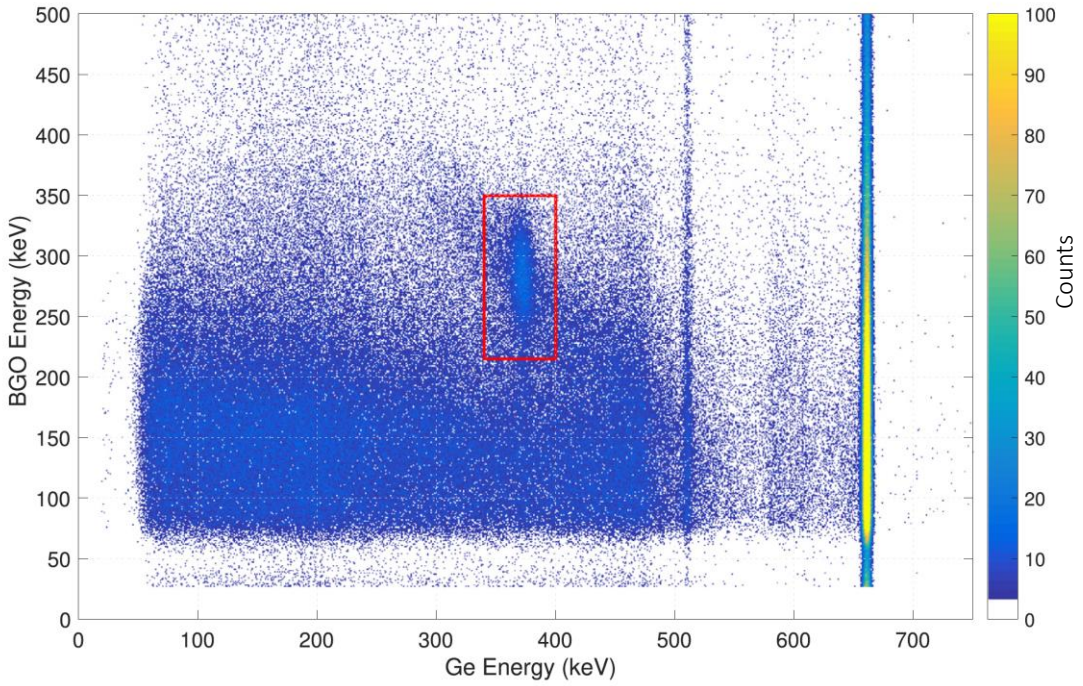

Figure 3.12: Energy deposited in the SAGe well and BGO detectors during the coincidence scan. The feature enclosed within the red box (horizontal range 340 – 400 keV, vertical range 220 – 350 keV) represents the area of 90^o Compton scattered events leaving 374 keV and 288 keV in the SAGe well and BGO respectively. The pronounced vertical lines represent the 662 keV full energy events and 511 keV annihilation photons in the SAGe well with random events in the BGO detectors.

3.9 Rise Times and Charge Collection Times

The rise times and the charge collection times of the GSW120 detector being characterised have been measured for different interaction positions. The information used to calculate the signal pulse rise time is from both the singles and coincidence scan of the front face and side of the detector. The rise time and charge collection time information are left for presentation in Chapter Five.

Chapter Four

EXPERIMENTAL AND SIMULATION RESULTS

4.0 Introduction

Experimental measurements have been used to assess the characteristics and performance of the SAGe well detector. The detector efficiency response has also been simulated with the Monte Carlo N-Particle (MCNP) code and the results have been compared with experimental results.

In this chapter, the results from the experimental measurement and MCNP simulation will be presented. The results from the singles and coincidence scan are not presented here but in Chapter Five for contextual relevance.

4.1 Shaping Time, Baseline Noise and System Gain Assessment.

The measurement to determine the best amplifier shaping time for the analogue measurements yielded a time of $6\mu s$. This shaping time was arrived at by examining the measured resolution for different shaping times. A $6\mu s$ shaping time is a sufficient time to accommodate the longest charge collection time for the SAGe well detector. This is in agreement with the shaping time suggested by the manufacturer.

The baseline fluctuation for this detector has been measured to be $4\ \mathrm{mV_{pp}}$ (i.e. from peak to peak). The system conversion gain determined using Equation 3.3 is $181.3\ \mathrm{mV/MeV}$ for a signal terminated at high impedance of $1\ \mathrm{M\Omega}$. The practical implication of the system gain value is a pulse height output of $8.5\ \mathrm{mV}$ and $11\ \mathrm{mV}$ for $47\ \mathrm{keV}$ and $60\ \mathrm{keV}$ gamma-ray energies respectively, for typical radionuclides (^{210}Pb and ^{241}Am) in environmental studies. The signal to noise ratio, $\mathrm{S/N}$, of the range of 4 - 5 in this case is therefore poor for measurements at this low energy range. To address this potential measurement issues for low energies, the preamplifier is equipped with two conversion gain settings [Can04]: 1X and 5X. For a preamplifier gain setting of 5X, the system conversion gain is measured to be $869\ \mathrm{mV/MeV}$ for signals terminated at high impedance, that is, an increment of a factor of about 5 compared to the signals measured with a gain setting of 1X. The slight deviation from a factor of 5 increment is likely due to discrepancy in the signal baseline measurement.

4.2 Energy Resolution Results

The energy resolution also known as the full width at half maximum, FWHM, (please refer to section 3.3) performance of the SAGe well has been assessed for various energies. Table C7 in Appendix C gives the values of the measured FWHM for full energy photopeak from the analogue system, moving window deconvolution (MWD) and baseline difference (BLD) methods. These values are plotted in Figure 4.1. A quick look at the plots show that the measurement with the analogue system gives a better energy resolution than the results from the digitised data sets. A comparison of the FWHM of energy peaks measured by the trapezoid filter (MWD) and the simple baseline difference (BLD) method is in agreement for low energy determination but significantly different at high energy. These differences in the FWHM values between

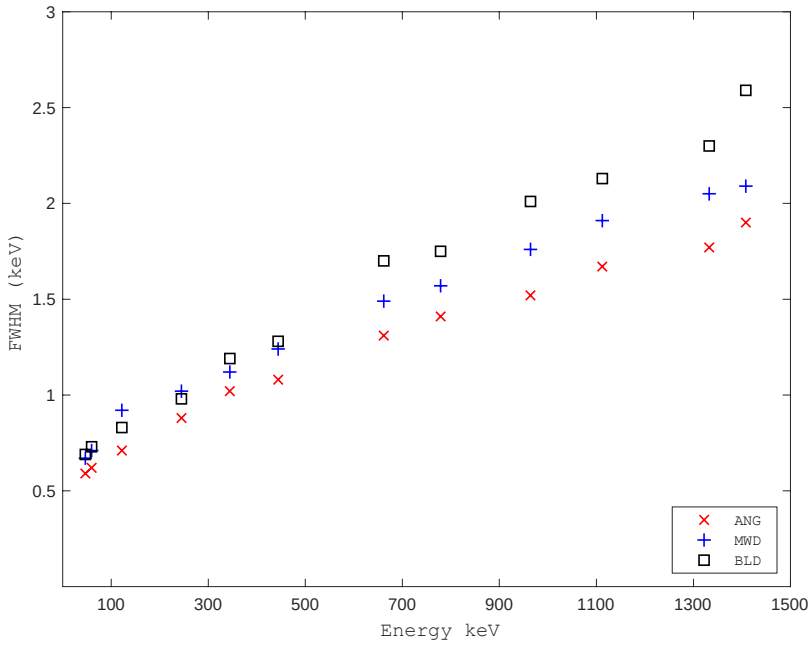

Figure 4.1: Comparison of FWHM measured with the analogue system (ANG), moving window deconvolution (MWD) and baseline difference energy from the digital acquisition system. At low energy ($47\ keV$ and $60\ keV$), the MWD and BLD measured FWHM are in agreement. The FWHM measured with analogue system gives a better result.

MWD and BLD is a result of the way the individual method calculates the energy information carried by each signal pulse. While BLD calculated energy is a simple subtraction of the average signal pulse baseline from the average of a number of signal samples at maximum pulse height, a referral is made to the details of the digitiser trapezoid filter energy calculation in [Ca13], [Jor93] and [Jor94]. In order to

understand the results, first the MWD and BLD calculated energy spectra are overlain in Figure 4.2 for $60\ keV$ and $662\ keV$ full energy peak.

It is seen on the plot that both spectra for $60\ keV$ are well matched, however, the $662\ keV$ energy peak calculated from the BLD method results in a pronounced tailing. At higher photon energy such as $662\ keV$ under study, Compton scattering is the predominant mechanism for energy transfer. The BLD method does not account for variations in charge collection time due to Compton scattered events depositing energy in more than one position (a multi-site interaction). The energy information carried by the charge pulse is underestimated and leading to the tailing on the low energy end of the full energy photopeak.

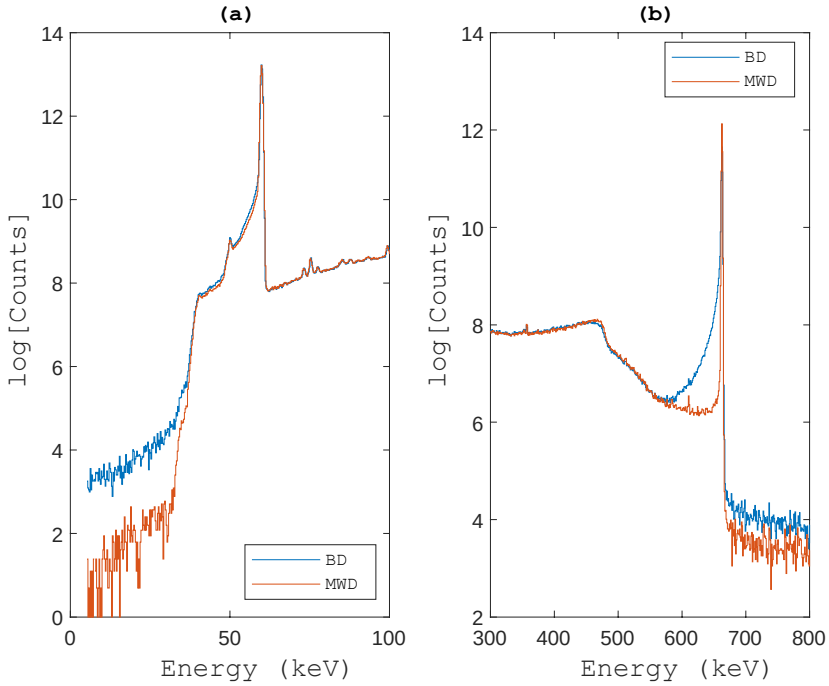

Figure 4.2: Full energy peak for (a) 60 keV and (b) 662 keV gamma-rays calculated by the moving window deconvolution (MWD) and baseline difference method. In (a) MWD and BLD methods correctly measures the 60 keV pulse height. In (b) energy deposition due to multi-site interactions will lead to in accuracies in the determination of the energy information carried by the charge pulse.

4.2.1 Energy Resolution Performance and Characteristic Contributions

The summary of the analogue system results for the energy resolution performance of the SAGe well detector is presented in this section. The FWHM increases from 0.59 keV at 47 keV up to 1.86 keV at the maximum energy of 1408 keV (see Table C7 in Appendix C for energy resolution results for energy range evaluated). The values

measured for the FWHM at 122 keV and 1332 keV are 0.71 keV and 1.77 keV respectively. These are consistent with the values reported by the manufacturer and published in [Ade15]. The significant contributions to the total FWHM, ΔE are [Kno10]: statistical variation in the number of charge carriers created, Δ_S; incomplete charge collection, Δ_C; and contributions from electronic noise, Δ_N. The quadrature addition of these individual contributions gives the total measured FWHM, ΔE, i.e.

$$(\Delta E)^2 = (\Delta_C)^2 + (\Delta_S)^2 + (\Delta_N)^2 + \ldots \quad (4.1)$$

A plot of the measured total FWHM is presented in Figure 4.3. The various contributions to the energy resolution can be estimated from the measured total FWHM results. A second order polynomial fit of $(\Delta E)^2$ as a function of the gamma-ray photon energy, E yields Equation 4.2. The parameters from this polynomial fit can be used to assess the contributions [Owe85] to the detector resolution performance.

$$(\Delta E)^2 = (1.837 \times 10^{-7} E^2) + (2.1 \times 10^{-3} E) + 0.26 \quad (4.2)$$

where E is in keV. The terms in Equation 4.2 represent terms in Equation 4.1 as follows; $(\Delta_C)^2 = 1.837 \times 10^{-7} E^2$ is the contribution from incomplete charge collection; $(\Delta_S)^2 = 2.1 \times 10^{-3} E$ is the contribution from statistical variation in the number of charge carriers produced and $(\Delta_N)^2 = 0.26$ is the electronic noise contribution. The values of the individual contributions (Δ_C), (Δ_S) and (Δ_N) to the total energy resolution performance of the GSW120 detector calculated from the fit parameters of Equation 4.2 are plotted as a function of the gamma-ray photon energy in Figure 4.3.

These plots show that the fit parameters give a good description of the experimental data. The contribution from electronic noise, Δ_N, is estimated from the fit to be 0.51 keV. This can be experimentally verified by using a pulser signal as the preamplifier input and measuring the FWHM of the peak produced. However, this has not been experimentally verified.

At low energy below 122 keV, it is observed from the plot that the contribution from electronic noise dominates above which the inherent statistical fluctuation in the number of charge carriers produced dominates. The electronic noise will therefore pose problems in measurements that involve very low energy gamma radiation.

In this analysis, the contribution to the total FWHM from charge collection efficiency, Δ_C, is treated as linearly dependent on energy. From the plot in Figure 4.3, it shows that this contribution is negligible at energies below 1173 keV but greater than that of electronic noise above this energy. According to [Kno10], the dominant contribution is determined by the size of the detector, energy of the radiation and the quality of the detector. The detector electrode geometry is also a contributing factor to the overall detector resolution performance. The statistical fluctuation in the number of charge carrier produced is the primary factor contributing to the overall energy resolution performance of the GSW120 SAGe well detector.

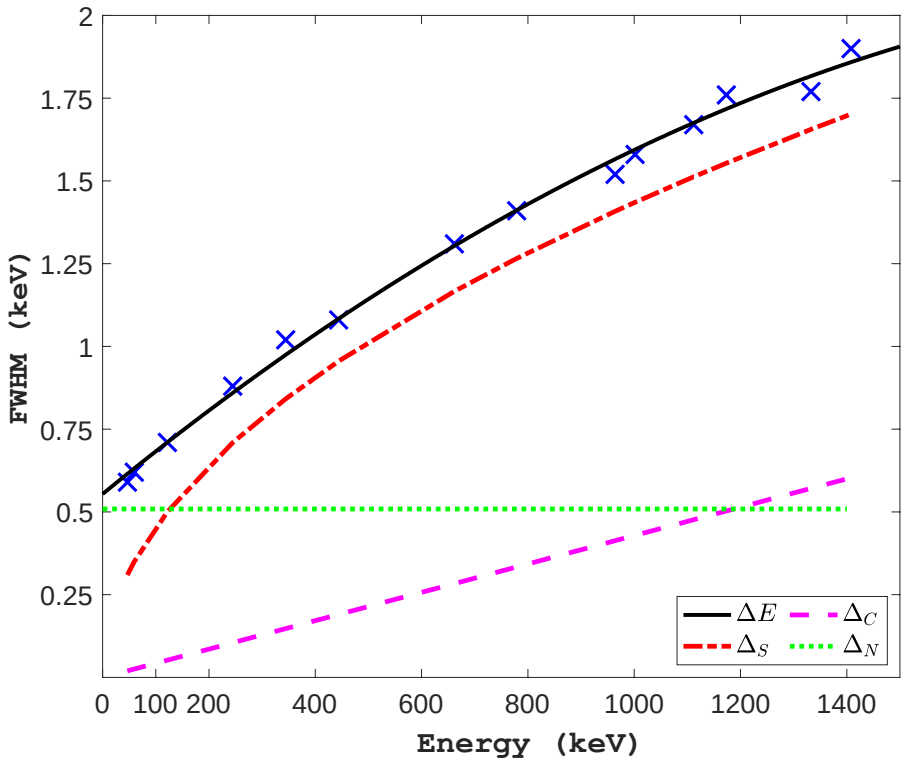

Figure 4.3: Measured energy resolution (FWHM) as a function of energy at nominal bias for GSW120. Errors are about 2% or less and as such error bars are not included for clarity purposes. Included in the plot are curves showing calculated contributions to the total energy resolution, ΔE. Δ_S, Δ_C, Δ_N are contributions from the statistical fluctuation in the number of charge carriers, charge collection efficiency and electronic noise respectively.

The Fano factor, F, which accounts for the departure of the observed variance in the number of charge carriers from the Poisson predicted variance can be calculated from the relationship between F and Δ_S given by [Ale02]:

$$(\Delta_S)^2 = (2.355)^2 F\epsilon E \quad (4.3)$$

where ϵ ($= 2.96 \times 10^{-3}\ keV\ at\ 77\ K$) is the energy required to produce an electron-hole pair in germanium. By evaluating Equation 4.3 with the $(\Delta_S)^2$ obtained from the polynomial fit parameters of Equation 4.2, a Fano factor of 0.128 is obtained from this experiment. This value is within range of published values in [Lut99 and Kno10], however it sits on the higher end of the range.

4.3 Bias Voltage Investigation

The detector response was investigated while varying the bias voltage. The results of observing the SAGe well detector's response to bias voltage variation are presented in this section. The results for measurements below $1\ kV$ are not included in the report because the ^{241}Am peak was below the channel range. It should be noted that the bias voltage for this detector is negative. All presentations and plots on bias voltage refers to a negative applied bias voltage.

4.3.1 Energy Resolution

The energy resolution (FWHM%) of the ^{241}Am and ^{137}Cs photopeaks measured as a function of bias voltage are plotted in Figure 4.4. The plots for both photopeaks' FWHM show an improvement in the energy resolution performance of the SAGe well detector. The improved performance is as a result of an improvement in the charge collection efficiency as the bias voltage is increased. The ^{241}Am peak FWHM improved by about 90% from its value of 15.5% at 1000 V to 1.6% at $3\ kV$. There is a gradual improvement to approximately 1% at 4400 V with no further improvement observed after that. At the full operating bias voltage of $5\ kV$, the energy resolution performance of the SAGe well detector for the ^{241}Am photopeak improved by approximately 93% from its value when the bias voltage was $1\ kV$.

4.3.2 Peak Centroid Position

The peak centroid position of the ^{241}Am and ^{137}Cs peaks obtained from an uncalibrated energy spectrum are analysed for different bias voltage. The peak centroid shift with reference to the centroid position at the detector bias voltage of $5\ kV$ is calculated

using Equation 3.8. Figure 4.5 shows how the peaks of both distributions have shifted with variations in the bias voltage with reference to its position at full detector bias. The centroid position shifts by as much as 64% for both peaks at a bias voltage of $1\ kV$. However, the position decreases as the voltage increases. As the voltage increases to $4.5\ kV$ no further shift in peak centroid position is observed. This bias voltage from which no peak centroid position shift occurs suggest that the full depletion voltage of the detector is likely in the region of $4.5\ kV$.

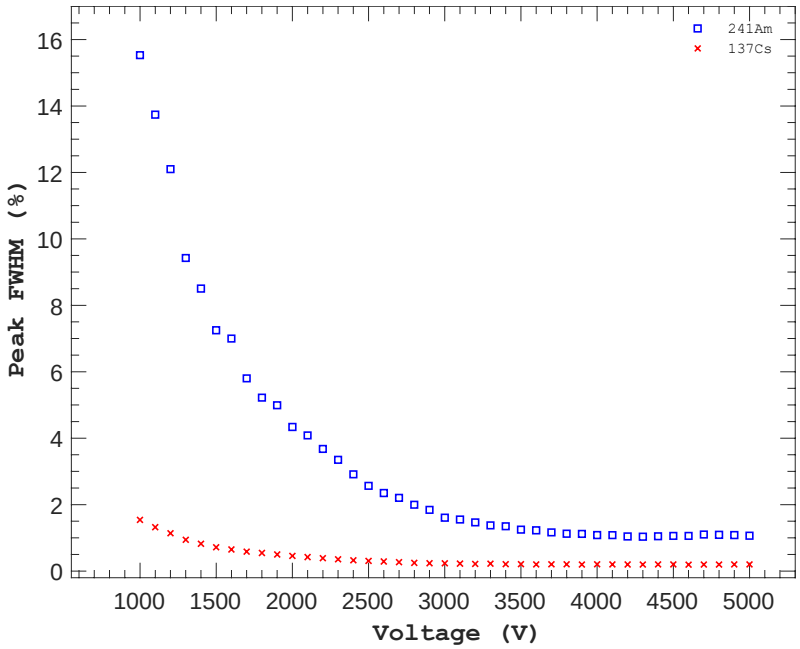

Figure 4.4: Effect of bias voltage change on the energy resolution of the GSW120 SAGe well detector. Measurements taken using ^{241}Am and ^{137}Cs gamma sources individually placed centrally on the detector axis 10 cm from the endcap. The resolution of the 60 keV peak deteriorates at low voltage but the 662 keV is only slightly affected.

4.3.3 Peak Count Rate

The results of the calculated net count rate of the ^{241}Am and ^{137}Cs peaks are presented in Figure 4.6. The result shows that the count rate for the ^{241}Am peak is independent of the detector bias voltage. However, the result also shows that the ^{137}Cs peak count rate increases as a function of the detector bias. At about $2.5\ kV$, the count rate for the ^{137}Cs peak approaches a plateau. The explanation for these differences in the detector count rate behaviour in the plot is as a result of the different locations in the crystal where interaction occurs. Since the detector depletes inwards from the surface

where the contacts are placed, the constant count rate for the low energy photons is due to a weighting potential that enhances charge transport for surface interactions more than bulk interactions [Har14]. For the ^{241}Am, a 2 – 3% error is estimated for the voltage range below $2\ kV$ while ~ 1% above. An error < 0.5% is estimated for the ^{137}Cs measurement.

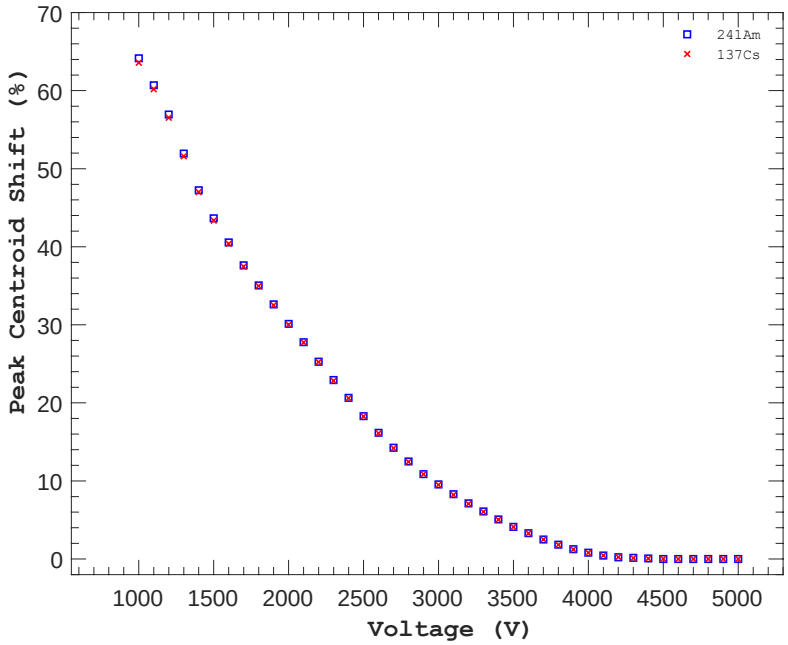

Figure 4.5: Effect of bias voltage change on the energy peak centroid position. The peak centroid is recorded from an uncalibrated energy spectrum of ^{241}Am and ^{137}Cs. The peak position changes as much as 64% for both ^{241}Am and ^{137}Cs energy peak compared to its position at the operating bias voltage.

4.4 SAGe Well Efficiency

The detection performance of the detector when carrying out measurements inside the detector well with samples containing radionuclides that emits gamma-ray photons has been examined. The results of the efficiency performance of this detector are presented. The plots in Figure 4.7 show the detector efficiency performance as a function of energy. As expected, in the low energy region, the efficiency increases as the gamma-ray energy increases. This trend was observed irrespective of the height of sample in the detector well. The analysis of this SAGe well efficiency performance carried out in this work does not cover energies greater than 60 keV and less than 662 keV. This is because the sample content of all radionuclides emitting energies within this range had undergone more than 10 half-lives (see Appendix B for sample

information) and are all decayed or are at the same level as the background. An assessment of the efficiency can still be done especially at the low energies available since these energies are relevant in environmental studies.

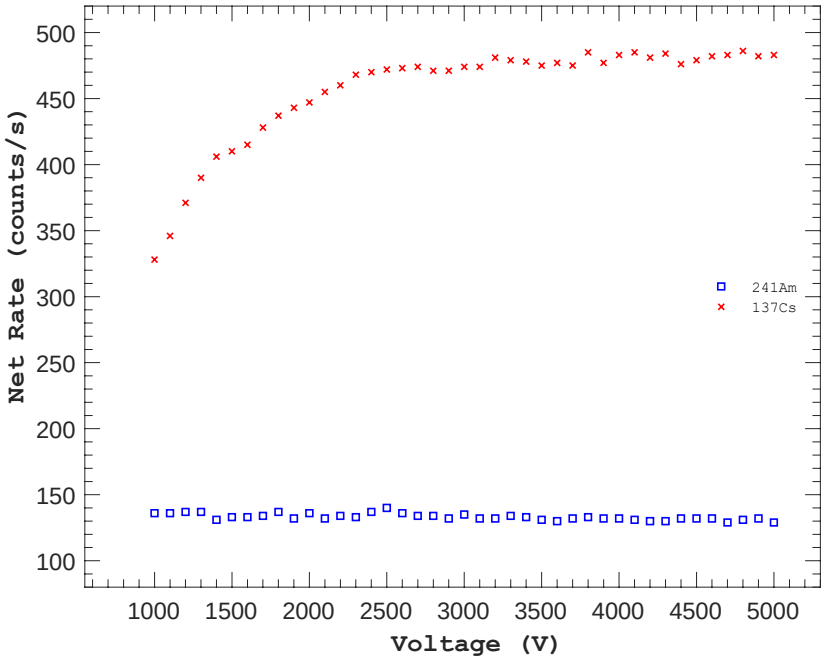

Figure 4.6: Net count rate measured at different detector bias voltage using ^{241}Am and ^{137}Cs uncollimated gamma sources individually positioned 10 cm from the endcap along the detector axis. The 60 keV peak count rate is unaffected by the bias voltage but the 662 keV is affected. Estimated error for 60 keV is about 1 – 3% for 60 keV while <0.5% for 662 keV count measurements.

It has been shown [App04] that the practical detection efficiency of a well detector is dependent on the geometry of the sample. A plot of the dependence of the efficiency of the SAGe well on the sample fill height is shown in Figure 4.8. In all cases, irrespective of the gamma-ray energy, it is observed that the efficiency decreases as the sample fill height increases in the well. If it is assumed that the sample is transparent to the gamma-ray energies, i.e. self-absorption has negligible effect on the counting efficiency of the detector, the sample fill height would be suggested to be responsible for the drop in the efficiency. The non-countable region of the geometric arrangement [Bel15] increases as the sample height increases resulting in a significant number of the photons not directed towards the detector crystal.

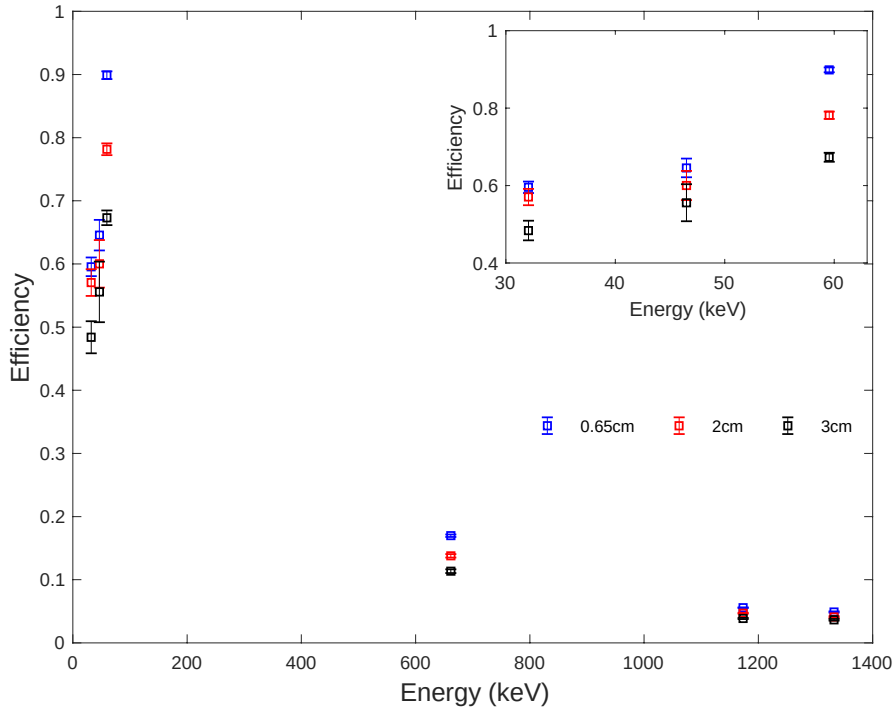

Figure 4.7: Efficiency – Energy relationshiop plots of samples of various heights placed in the SAGe detector well. The insert is a zoom in of the low energy region of 30 keV to 60 keV. The plot shows that in the low energy region, the efficiency increases with energy as expected but decreases as more sample fills the well.

The diagram in Figure 3.5 showed a cross section of the SAGe well geometry with different sample heights in the detector's well used for the measurements. The results show that at a sample fill height of 0.65 cm the efficiencies are $(59.5 \pm 1.4)\%$, $(64.6 \pm 2.4)\%$ and $(89.9 \pm 0.6)\%$ for 32 keV, 47 keV and 60 keV respectively in the low energy region. These values however drop to $(48.4 \pm 2.5)\%$, $(55.6 \pm 4.8)\%$ and $(67.3 \pm 1.2)\%$ for 32 keV, 47 keV and 60 keV respectively at a sample height of 3.5 cm about the plane of the crystal top. The same efficiency behaviour is observed for the high energy region.

The efficiency values of $(16.9 \pm 0.2)\%$ and $(4.9 \pm 0.1)\%$ decrease to $(11.4 \pm 0.3)\%$ and $(3.7 \pm 0.1)\%$ for 662 keV and 1332 keV respectively when the sample height increases from 0.65 cm to 3.5 cm. The efficiency loss as a function of the sample fill height is evaluated and plotted in Figure 4.9. These are normalised against the highest efficiency obtained from the measurements, that is, the efficiency response of the detector with a 0.65 cm sample fill in the well.

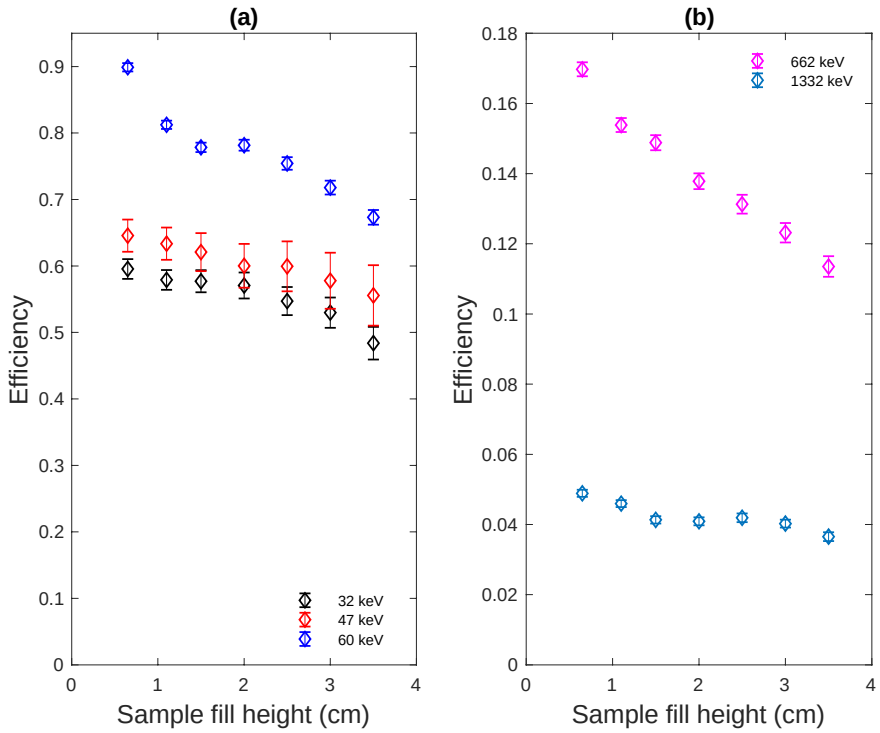

Figure 4.8: Efficiency variation with the amount of sample in the well shown as the sample fill height. The corresponding masses for the fill heights; 0.65 cm, 1.10 cm, 1.50 cm, 2.00 cm, 2.50 cm, 3.00 cm, 3.50 cm are 0.779 g, 1.374 g, 1.890 g, 2.526 g, 3.210 g, 3.858 g, 4.489 g, respectively (refer to Figure 3.5 for diagram showing the geometry). These plots show that for all energies, the efficiency decreases as the volume (mass) of sample increases in the well.

In Figure 4.9, it is observed that the efficiencies of the low energy gamma-rays are the least affected. The efficiency reduces as much as 19%, 14%, 24% for 32 keV, 47 keV and 60 keV for an increase in the sample height from 0.65 cm to 3.5 cm. The efficiency of the 662 keV is the most affected by the sample height by as much as 33 % loss.

Apart from the contributions from the foregoing geometric arrangement to the efficiency reduction, the crystal thickness of the SAGe well detector plays an important role for the high energy measurements. The detector crystal thickness on the well sides reduces towards the top of the detector; less than 1 cm at its thinnest. It is suggested that the reduction in the crystal thickness contributes significantly to the efficiency decline at high energy.

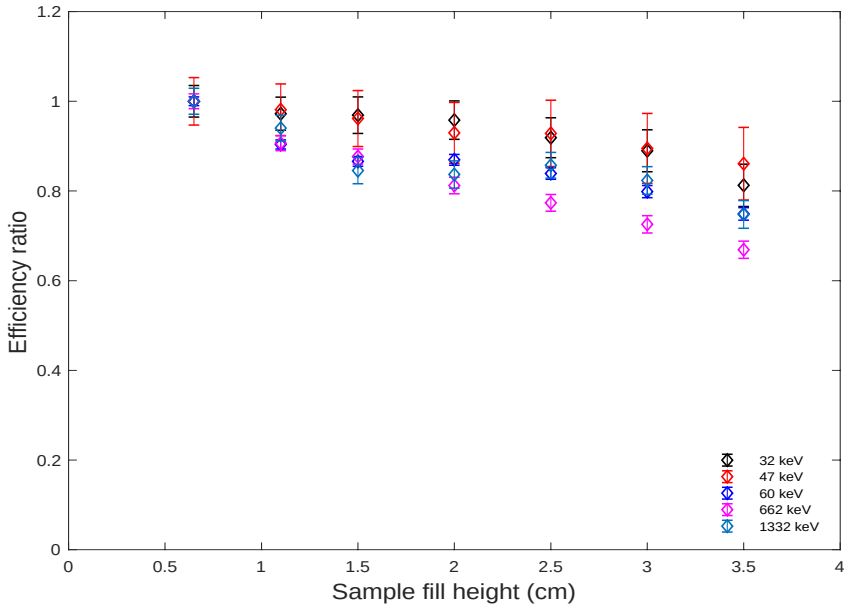

Figure 4.9: Efficiency loss as a function of sample fill height in the detector well. The corresponding masses for the fill heights; 0.65 cm, 1.10 cm, 1.50 cm, 2.00 cm, 2.50 cm, 3.00 cm, 3.50 cm are 0.779 g, 1.374 g, 1.890 g, 2.526 g, 3.210 g, 3.858 g, 4.489 g, respectively (refer to Figure 3.5 for diagram showing the geometry).. The plot shows that the efficiency is also dependent on the amount of sample in the detector well. As the amount of sample increases, efficiency decreases.

4.5 Comparison of SAGe well and BEGe Performance

The results of the comparison between the GSW120 detector under study and a BE2825 model BEGe detector is presented on the basis of absolute efficiency and peak quality. In Figure 3.7, the relative size and geometry of the SAGe well detector crystal to that of a BEGe detector was shown. The positioning of the sample on both detectors was also shown in the same figure.

The absolute efficiency calculated for the detectors (see results on Tables C8 – C11 in Appendix C) is plotted in Figure 4.10 as a function of the sample mass. The plot reveals how the SAGe well compares to a BEGe detector in terms of their absolute efficiency measured with samples placed on the endcap of each detector. At low energies up to 60 keV, the measured absolute efficiency of the BEGe detector outperforms the SAGe well detector for all sample mass measured. However, for higher energies such as 662 keV and above used in this work, the SAGe well performance is comparable to that of the BEGe with samples placed on both detector's endcap.

These performances measured can be explained based on the detector size and composite materials. The SAGe well is not optimised for measurements (low energy)

on the detector endcap since its intended use is with samples inserted in the well whereas the BEGe detector's entrant window is made of carbon composite allowing for low energy measurements. As radiation from the sample placed on the detector face penetrates and traverses through a thicker amount of germanium material in both detectors, the efficiency of obtained for both detectors are expected. However, for very high energy gamma rays, SAGe well detector with a crystal length of about 6.5 cm may perform well against a BEGe of 2.5 cm thickness. Apart from the 32 keV energy where no defined absolute efficiency trend is observed, the absolute efficiency decreases with increasing amount of sample measured for all energies analysed.

The analysis of the full energy peak measured with both the SAGe well and the BEGe detectors reveal further how both detectors perform against each other. Table 4.1 gives the ratio of the net to gross count within the photopeak region for each energy analysed.

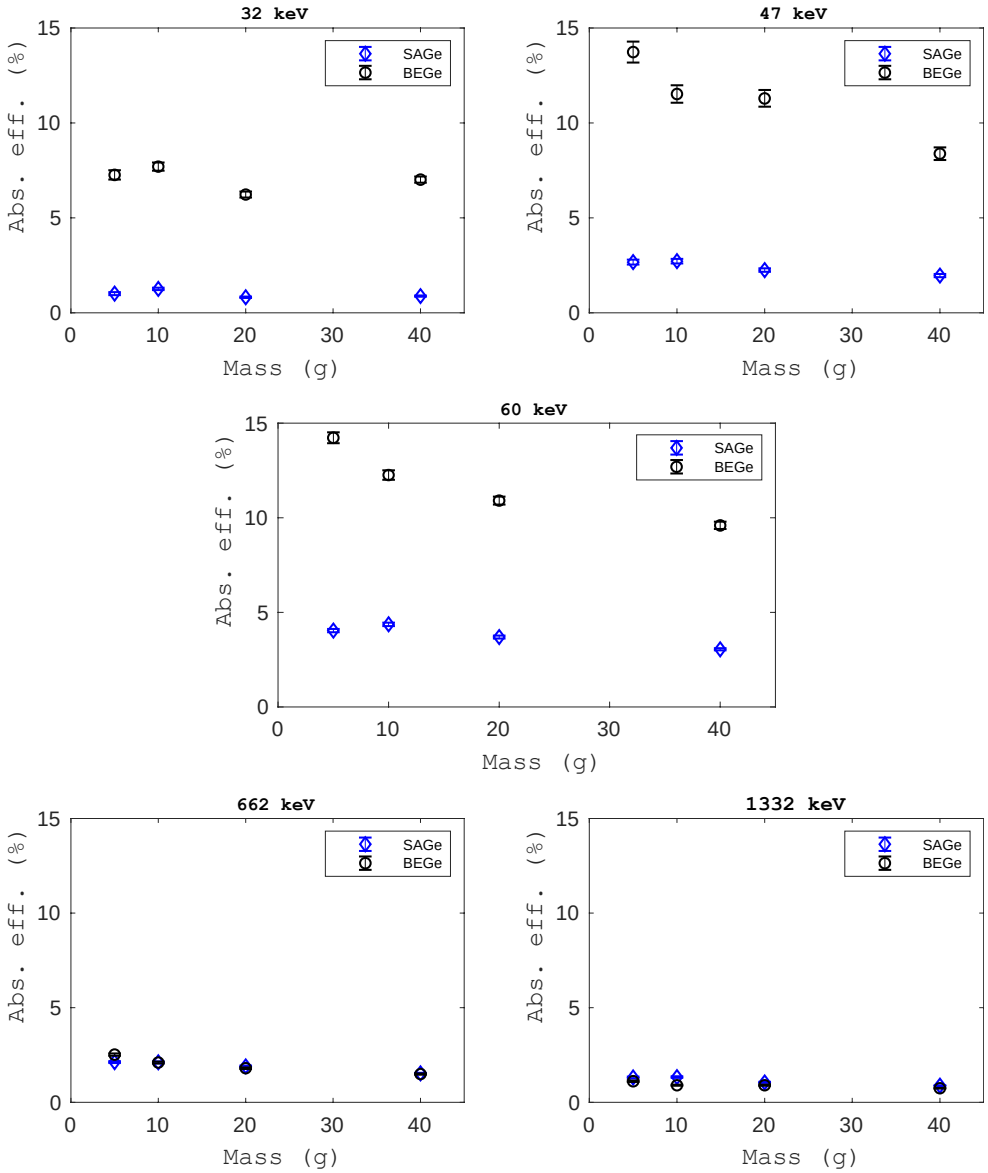

Figure 4.10 Energy efficiency performance of GSW120 SAGe well and a BE2825 model BEGe detector as a function of sample mass when a 4 cm diameter sample is placed on the endcap of each detector. The BEGe's efficiency performance is better than the SAGe well at low energy.

The energy peak net to gross area shows that less background affects the photopeak when samples are placed in the well than when it is on the end cap. A 5 g sample placed inside the detector well is compared with results from measurements with 40 g placed on both the SAGe well and BEGe detector end cap. The net peak area of the 5 g sample in the well is higher than that of 40 g sample placed on the endcap of both the SAGe well and BEGe detector. The 40 g sample measurement on the SAGe detector well endcap fared worse for 32 keV energy, otherwise, the SAGe well net to gross area ratio is comparable to BEGe's with samples on the endcap.

The results from the measurements with sample on the endcap and inside the SAGe detector well further supports the fact that the detector's well is enhanced for low energy measurements.

Table 4.1: Peak net to gross area measurement for SAGe well and BEGe.

Energy (keV)	Net area/Gross area					
	SAGe well				BEGe	
	Well		Endcap (top)		Endcap (top)	
	(5 g)	±	40 g	±	40 g	±
32	0.790	0.012	0.390	0.012	0.760	0.010
47	0.930	0.008	0.740	0.011	0.790	0.006
60	0.980	0.004	0.930	0.006	0.950	0.004
662	0.990	0.008	0.980	0.008	0.970	0.008
1332	0.960	0.023	0.960	0.019	0.940	0.020

4.6 MCNP Simulated Efficiency Results

The results of SAGe well detector efficiency simulated with MCNP is plotted in Figure 4.11. The results show that the efficiency for all energies decreases with height of the sample in the detector well. These results follow the same trend as the experimental results discussed in Section 4.4. In order to appreciate the differences in the results obtained from the experiments and MCNP simulation of the SAGe well response, Figure 4.8 and Figure 4.11 are plotted together in Figure 4.12. The MCNP simulated results are much higher than the response measured from the experiment with the exception of the 32 keV energy response for the 0.65 cm sample fill height. This discrepancy between the experiment and the MCNP simulation is thought to be a result of not inputting a detailed detector material composition and dimensions.

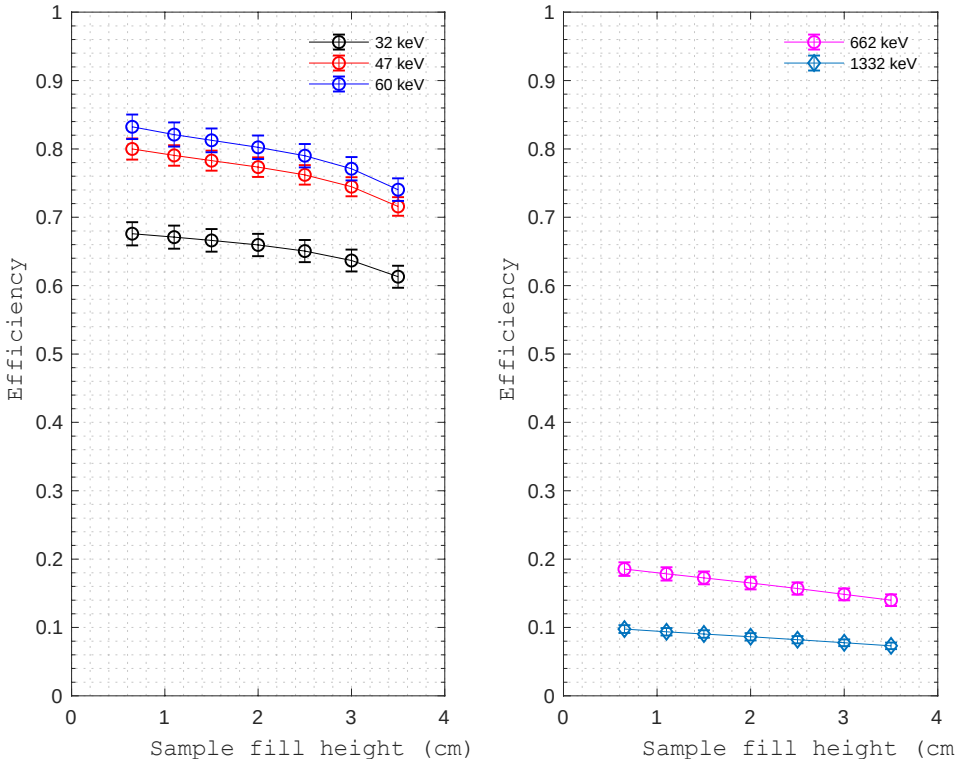

Figure 4.11: MCNP simulated efficiency of the SAGe well detector with different sample fill height. The efficiency for all energies is directly proportional to the height of sample in the well.

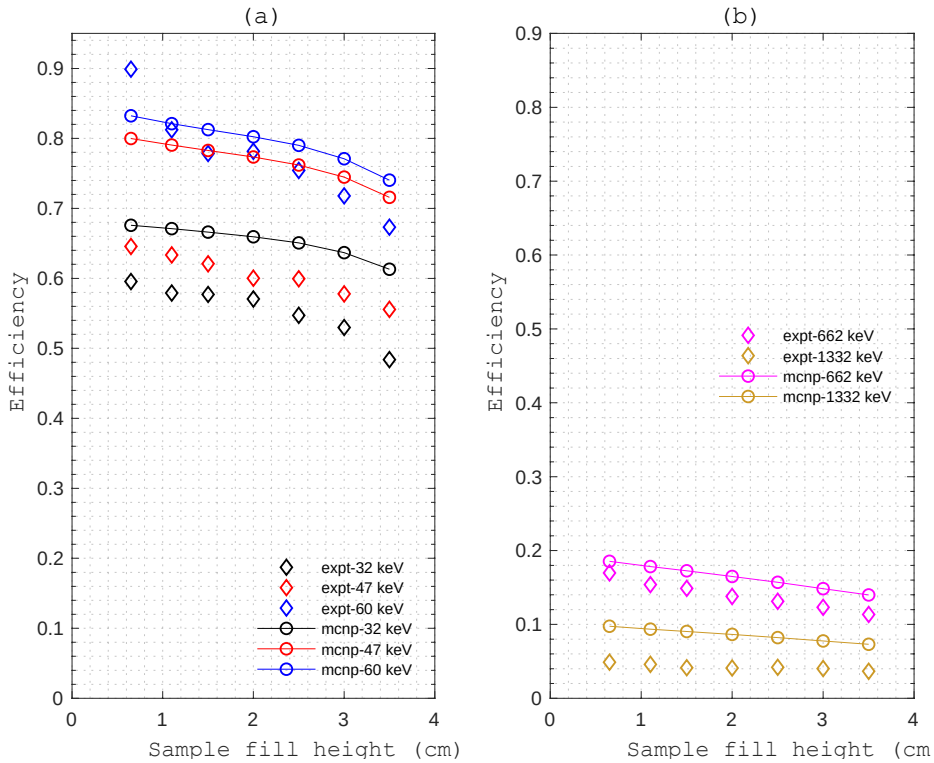

Figure 4.12: Experimental and MCNP simulated efficiency of the SAGe well detector. (a) Detector efficiency in the low energy region for 32 keV (black), 47 keV (red) and 60 keV (blue). (b) Efficiency in the higher energy region for 662 keV and 1332 keV. The simulated results are higher than experimental results. Errors are not plotted for clarity.

Some of the detector material composition and dimensions are proprietary and as such were not provided by the manufacturer. Notwithstanding this setback, MCNP simulation still show the expected efficiency response curve trend (Figure 4.13) for a semiconductor-based detector.

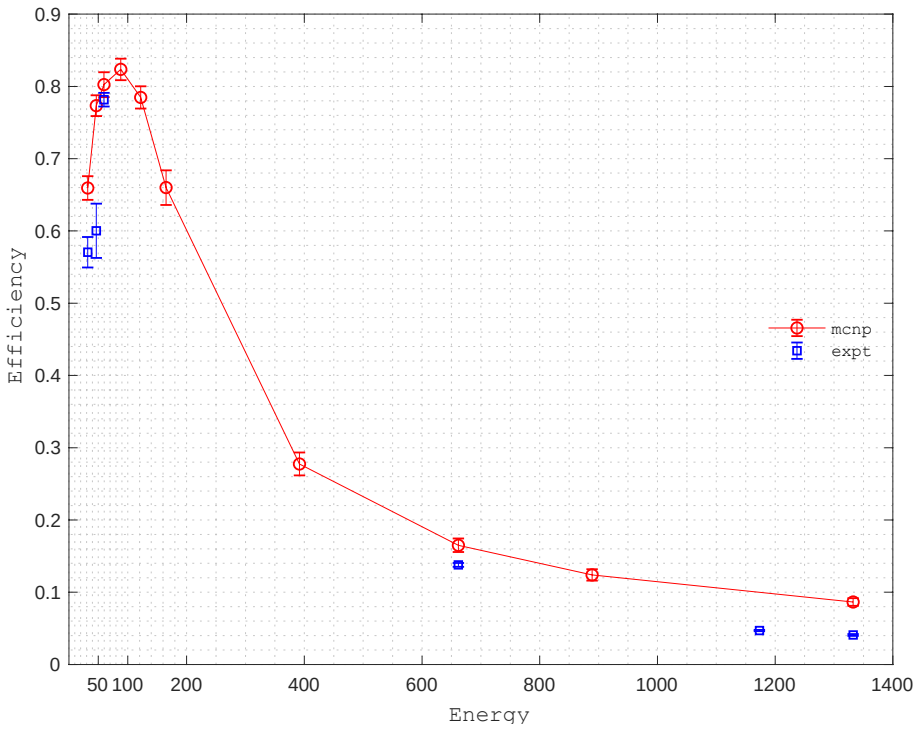

Figure 4.13: Simulated efficiency curve (red) of the SAGe well detector for a 2 cm sample fill height. The experimentally measured energy efficiency response for the same sample fill height is shown in blue.

Chapter Five

PULSE SHAPE ANALYSIS AND PERFORMANCE OPTIMISATION

5.0 Pulse Shape Discrimination

The advancement in high-purity germanium (HPGe) detector technology, data acquisition and processing instrumentation have led to an improvement in the investigation and understanding of pulse shape topology in detector volume [Bru16]. This has enabled the acquisition of detector signals' pulse shape through digitisation with high resolution and high sampling frequency. The information from the pulse shape can be exploited to provide adequate timing information of interactions throughout the detector volume. The signal pulses from interactions in the SAGe well detector were measured as described in Section 3.8 of this thesis. Pulses measured from irradiating the detector in singles scanning mode and coincidence mode are investigated and the results are presented in this chapter.

In order to understand the results obtained from the pulse shape measurement, the electric field and the weighting potential has been simulated using the AGATA Detector Library (ADL). The detector response is also simulated for interaction positions of interest for the purpose of this study.

The analysis and discrimination of the charge pulse is reliant on interactions at different positions producing signals. Pulse shape discrimination will be done for charge pulses generated for interactions on the basis of the detector depth and radial variation profile.

5.1 Detector Front and Side Singles Scan

The photopeak interaction measurement from the singles scan of both the front and side irradiation of the detector is shown in Figure 5.1. The intensity matrix clearly shows the variation in photopeak counts in the SAGe well detector. The top pane images in Figure 5.1 are obtained from the irradiation of the detector front face with an ^{241}Am collimated gamma-ray source emitting 60 keV photons while the bottom pane images are those of the 662 keV gamma-ray irradiation of the detector side with a collimated ^{137}Cs source. The source was held for 2 s and 1 s for the front and side singles scan respectively for the irradiation of the detector. Images on the right of each

pane are energy gated to eliminate interactions from other sources. It is worthy to note that the position information recorded while performing the singles scan is the collimator position provided by the scanning table. The coordinates of the plot in Figure 5.1 have been translated into the SAGe well detector coordinate frame having the origin at the centre of the p+ contact. Two low photopeak intensity bands can be seen on the bottom pane images around z = 0 – 10 mm and z = 20 – 30 mm. These low intensity bands result from gamma-ray interaction with attenuating materials used for structural support of the crystal.

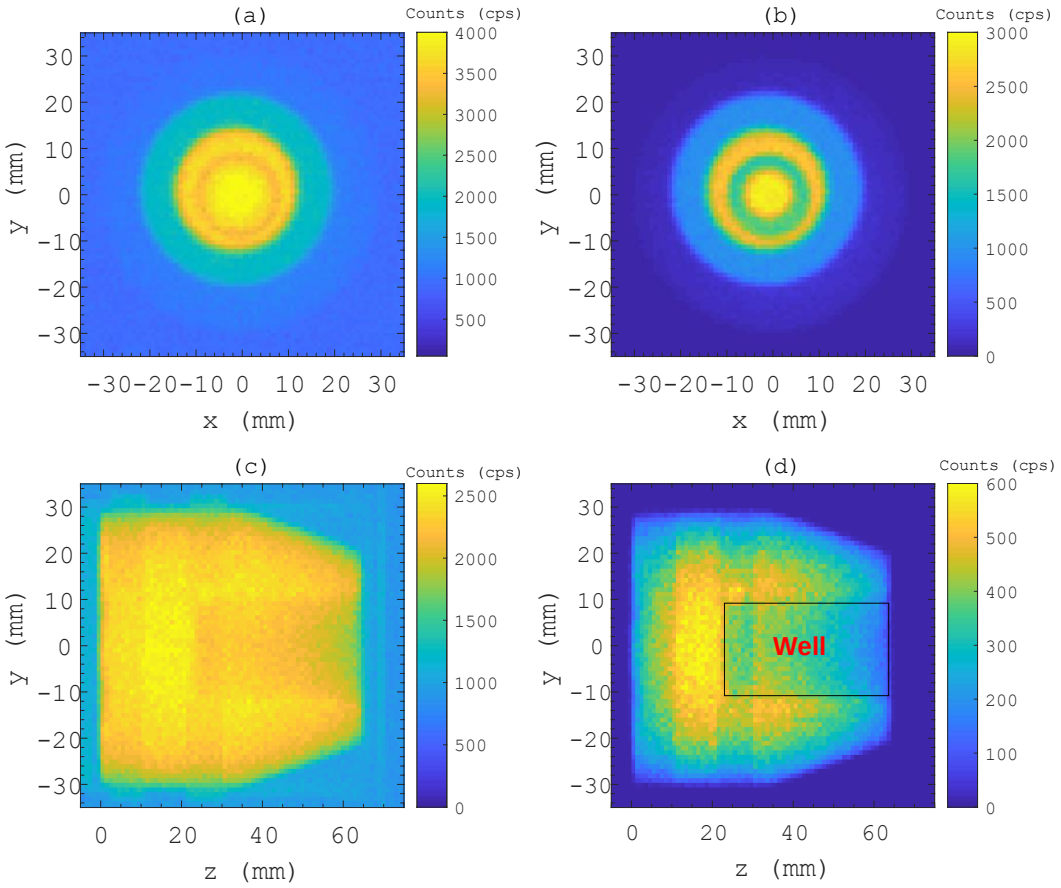

Figure 5.1: Photopeak counts as a function of collimated source position for the front face scan (a and b) with ^{241}Am and side scan with ^{137}Cs (c and d). The events in (a) and (c) are energy gated around 60 keV and 662 keV respectively to obtain (b) and (d). The profile of the detector crystal inside the cryostat is revealed on the side scan intensity matrix. The coordinates have been translated into the detector frame where the origin is at the centre of the p+ electrode and the x, y, and z axes run parallel to the ⟨100⟩, ⟨010⟩, and ⟨001⟩ crystal axes respectively.

In Figure 5.1, the intensity of the front face scan shows poor resolution due to the tapered edges of the detector crystal and thick dead layer on the outer surface of the

crystal therefore, not favourable for low energy penetrations. Also, since Compton scattering is the major interaction mechanism of the 662 keV gamma-rays in germanium, full energy deposition would occur after 2 or more scattering processes. This increases the likelihood of scattering out of the detector active volume for photons that interacted near the crystal surface. This is evident in the low intensity on the edges of the crystal in the bottom right pane image.

5.1.1 Pulse Shape and Risetime Distribution

As interactions occur throughout the active volume of the detector crystal, there is a need to investigate the distribution of the pulse shape and rise times for interactions at different regions in the detector volume. Information extracted from the singles scan is an effective tool to study these distributions.

Pulse Shape Distribution

The shape of some pulses measured from two irradiation positions on the side scan; one near the top (furthest from the p+ contact) and the other near the bottom of the detector crystal (near the p+ contact) are shown in Figure 5.2. These positions translate to points on the detector *yz* coordinate frame at y = 9 mm, z = 6 mm (top pane) and y = 19 mm, z = 51 mm (bottom pane). These positions were chosen so that the beam passes through coincidence points R1 and D6 defined in Section 5.2 and Table 5.1.

The top and bottom left pane in Figure 5.2 show the charge pulses recorded for 50 random full energy photopeak events from 662 keV photon deposition, in the detector active volume when the collimated source pointed at the coordinates described above. It is observed from the figure that both multi-site events (MSE) and single site events (SSE) are present in these measurements as expected for a 662 keV photon scattering germanium. To appreciate the pulse shape distribution when the photon beam passes through the detector material, a MSE discrimination filter technique that was designed for coincidence scan data analysis has been applied (pulses shown on the right panel). A qualitative observation of the SSE charge pulse shape on the top righthand pane of Figure 5.2 show a distribution of both fast and slow leading pulse edges for photon beam coordinates (at y = 9 mm and z = 6 mm). This pulse shape

distribution indicates the expected pulse shapes for SSE for interactions on a plane near the p+ contact as opposed to interactions in the upper volume of the detector. On the bottom right pane of Figure 5.2, the pulse shape tends to be uniform with a slow leading edge. This is an indication that other than MSE energy deposition, there is minimal variation in the shape of pulses created by interactions in the upper volume of the SAGe well detector. The investigation of pulse shape variations as a function of the interaction position in the detector crystal volume will be revisited in the presentation of coincidence scan result in Section 5.3.

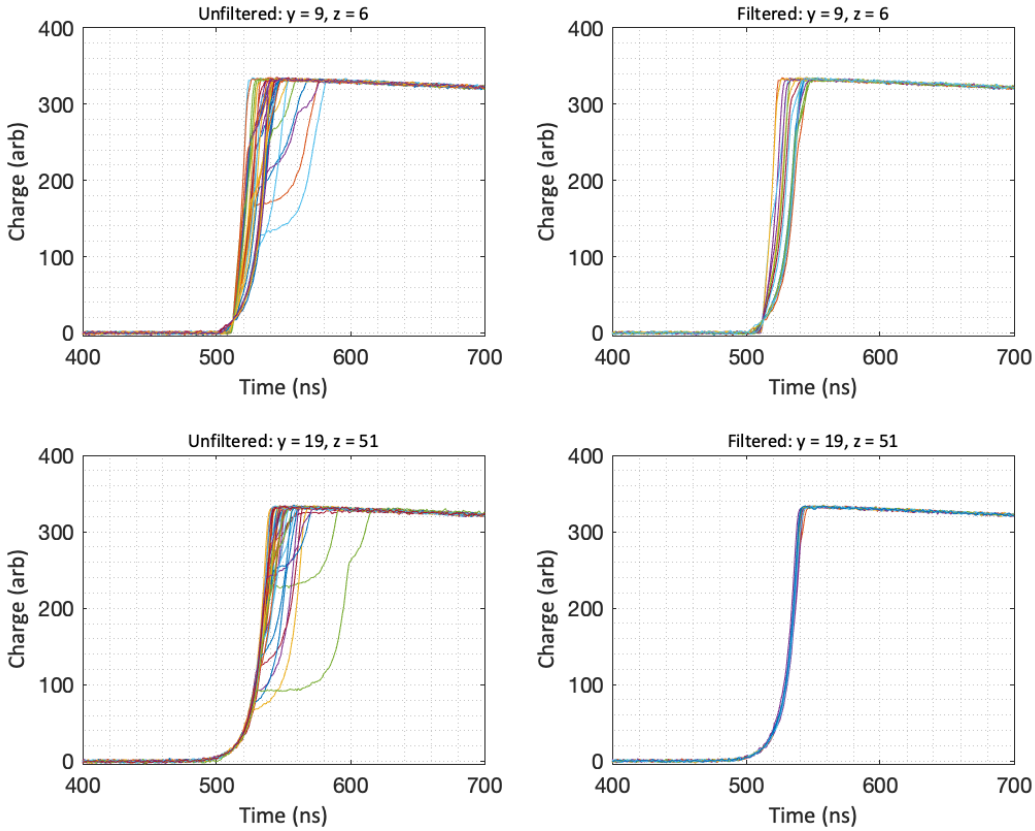

Figure 5.2: Charge pulse collected when a 662 keV collimated beam of gamma-rays passes through position R1 and D6 (see Table 5.1 for coordinates) along the *y-z* plane. The charge pulses extracted are for events within 4 keV energy gates around 662 keV. The left panels (Top and bottom) shows a set of 50 charge pulses from both single and multi-site interactions and the right panels (top and bottom) shows events that multi-site interactions have been filtered out using an algorithm.

Mean Rise Time Distribution

Mean rise time maps of pulses per scanning table position are shown in Figure 5.3 for the detector front face irradiation with ^{241}Am and Figure 5.4 for a side irradiation of

the detector with ^{137}Cs. The rise times T30 (ns) and T90 (ns) were calculated for all pulses at each scanning table position and the mean rise time formed. T30 is the interval between times at which the pulse reaches 10% and 30% of its maximum height and T90 interval time between 10% and 90% pulse amplitude. These were calculated for all energy gated pulses at each scanning position.

Since the front face irradiation was performed with 60 keV energy, the rise time in Figure 5.3 represents a mean distribution for near surface gamma-ray interaction on the top end on the SAGe well detector. The time distribution on the map shows that an interaction in the crystal beneath the detector well has lower values than other surfaces irradiated from the top of the detector. This is expected because the charge carriers created at those positions would travel the shortest distance to both the n+ and p+ electrodes. The values of the mean T30 < 90 ns for interactions near the well surface and T30 > 100 ns for charges created on the top end of the detector. T90 < 180 ns in the well and T90 > 196 ns from pulses created on the top surface.

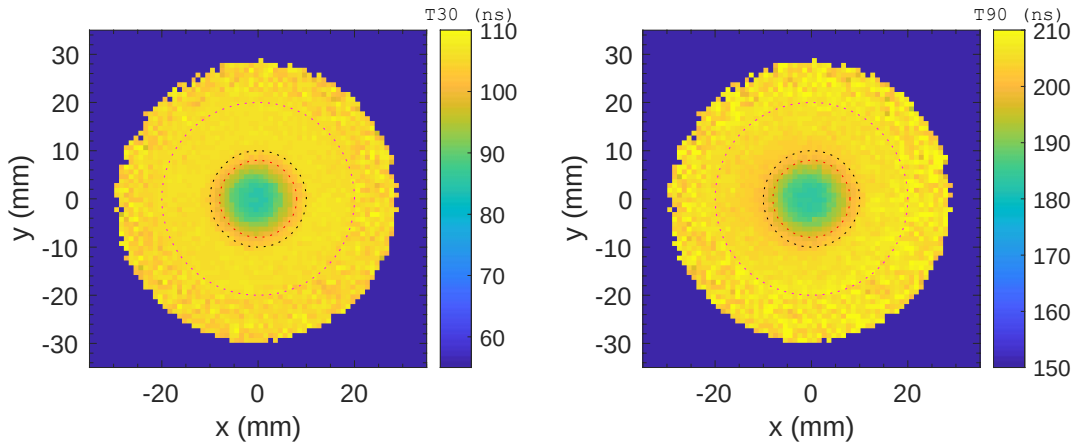

Figure 5.3: Mean [left] T30 (ns) and [right] T90 (ns) rise time distribution as a function of scanning table position when the detector front face was irradiated with a collimated ^{241}Am gamma-ray source. A 4 keV wide energy gate at 60 keV has been applied. The T30 values range from about 85 ns to 106 ns while the T90 range from about 180 ns – 210 ns. Values for rise times are lower for events beneath the well base. The concentric lines show the well and the tapered crystal edge boundaries.

Again, there is minimal evidence from the T30 and T90 mean rise time distribution to suggest any radial relationship in charge collection for events that occur at or near the surface on the front face of the detector. The crystal axis profile observed in the rise time map of BEGe detectors in similar measurements procedures by [Bar11] and

[Har14] was not seen for the SAGe well detector. Since 60 keV gamma-rays energy would interact and deposit all of its energy at shallow depths in the crystal at the front face of the detector, it is asserted that the geometry of the SAGe well and the electrical field profile in the detector are the reason for the non-observation. This assertion is the subject of the simulation that will be presented in a later part of this work.

The map of rise times calculated for charge pulses from deep interaction sites in the detector volume, created by high energy gamma irradiation of the front face would most probably suffice to reveal the crystal axis. However, this could not be done because the only high energy collimated source incorporated in the scanning table has a vertical gamma-ray beam profile while the detector crystal is horizontally oriented.

The mean T30 and T90 rise times calculated for charge pulses created when the detector's side was irradiated with ^{137}Cs is shown in Figure 5.4. For 662 keV photons full energy deposition dominated by Compton scattering, the gamma-ray will predominantly lose its energy at more than one interaction site before photoelectric absorption. This will result in measured pulses that are a superposition of the total charges collected from MSE interactions as earlier shown on the righthand panes of Figure 5.2. The calculated T30 rise time distribution from the side scan investigation has shown a unique mushroom shaped area (Figure 5.4a) fast times < 80 ns directly over the p+ contact. The remaining bulk volume of the detector have T30 rise times > 110 ns. The T90 calculated and presented in Figure 5.4b (right pane) have shown a random time distribution. This is expected since the interaction sites are scattered over the whole detector due to Compton scattering and most importantly, rise time is dependent on the electric field distribution in the detector. The influence of the electric field distribution on the rise time is discussed in Section 5.3.

At this point, it is worth reiterating that these pulse shapes and the rise times calculated for the singles scan do not give information on specific interaction positions in the detector volume. Rather, it is a function of the scanning table position for all events that occurred in the detector. In singles scan measurements, the two - dimensional information obtained is an average over the third dimension.

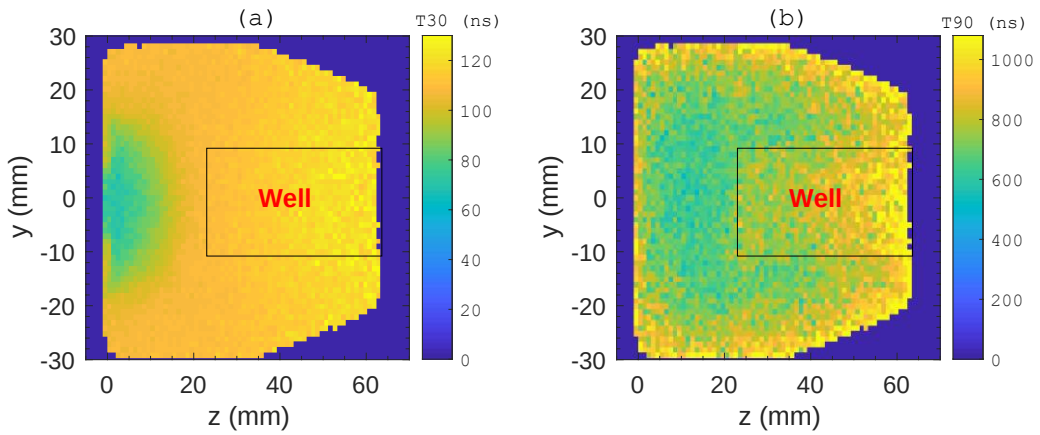

Figure 5.4: Mean [left] T30 (ns) and [right] T90 (ns) rise time distributions as a function of scanning table position when the detector was irradiated from the side with a collimated ^{137}Cs gamma-ray source. A 4 keV wide energy gate at 662 keV has been applied. The T30 rise time plot shows a region of relatively fast risetime (about 40 – 80 ns) near the p+ contact compared to other regions in the detector. Slight variations of T30 can be observed along the detector depth (z-axis). The T90 distribution (right pane) is strongly affected by MSE interactions.

5.2 SAGe Well Charge Pulse Characterisation

In the previous section, the properties of the charge pulse such as shape and rise time were presented as a function of the scanning table position. The information obtained is not sufficient for the detector pulse shape characterisation as no related position in the crystal is available from the singles scan. The position related information is obtained from the coincidence scan. In order to understand the charge carriers' properties such as the charge collection time, pulse shape and rise time as a function of the interaction position, other detector properties are needed in conjunction with the interaction position. These properties are the electric field and weighting potential in the detector material. The electric field and weighting potential have been simulated using the AGATA Detector Library (ADL) to investigate the rise times and charge collection characteristics. A brief description of ADL is therefore presented below.

5.2.1 AGATA Detector Library

The AGATA Detector Library (ADL) was designed for the AGATA project [Akk12] to enable the characterisation of position-dependent semiconductor detector response to gamma-ray interaction. The ADL script written in C computer language, implements

different routines shown in green in the block diagram of Figure 5.5 using user provided inputs shown in blue. The ADL scripts consists of two routines called the "Poisson Solver" and "Calculate Traces". These routines utilise input parameters to implement its functions described in the following subsections. The calculation of the charge carrier transit in time steps through the semiconductor detector volume is one of the three subroutines performed in the "Calculate Traces" routine. The other subroutines shown in Figure 5.5 are the estimation of the induced charges in electrodes and the convolution of the signal. Though ADL was created for AGATA detector geometries, this has been modified to implement the SAGe well detector geometry.

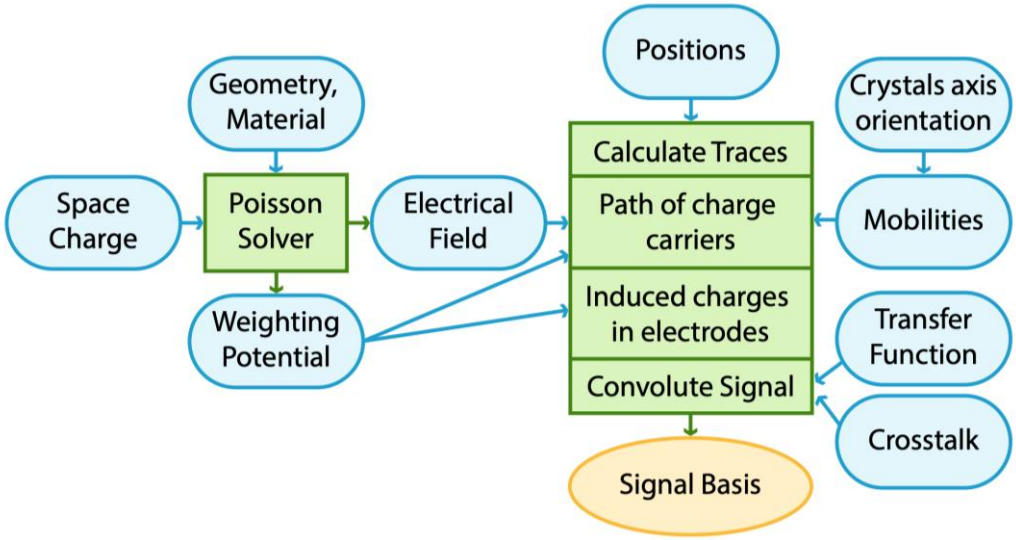

Figure 5.5: Block diagram showing the routines (green) and the input (blue) used in ADL simulation for a HPGe detector response [Bru16]. The blue arrows show the input required by each routine while the green arrows indicate the output of each routine.

5.2.1.1 Electric Field and Weighting Potentials Calculation in ADL

In order to simulate the detector response, the electrical field and the weighting potential in the entire detector volume needs to be calculated. This is implemented in ADL by the "Poisson Solver". This is based on the SIMION® [Sim19] software package that is primarily used to calculate electric fields. The trajectories of charged particles in the calculated fields are also calculated when the electrodes configuration, voltages and initial particle conditions are provided. The whole detector volume including the

electrodes are divided into 0.5 mm cubes called voxels. Each of these voxels is either electrodes or detector material.

In order to calculate the weighting potential for the SAGe well, the solver sets the potential of the p+ electrode to 1 V and that of the n+ electrode is set to 0 V before an iteration over all the voxels is performed to find the solution (the reader is referred to [Bru16] for details). The electric field is the sum of the field generated by the uncompensated net impurity charge density in the germanium crystal and the electrode weighting potential that is scaled by the bias voltage. The impurity profile provided by the manufacturer was used for the simulation of the SAGe well detector. The parameters for electron and hole mobilities used in ADL simulation of the SAGe well detector is given in [Bru16].

The ADL simulation of the SAGe well detector yielded the electric and weighting potentials calculated for the p+ electrode that is shown in Figure 5.6. The figure shows a rz slice of the electric potential and the weighting potential distribution in the SAGe well calculated by ADL for the p+ point contact. These rz slice for the potentials is invariant for any angle in the xy plane due to the detector's rotational symmetry along the detector axis (z- axis).

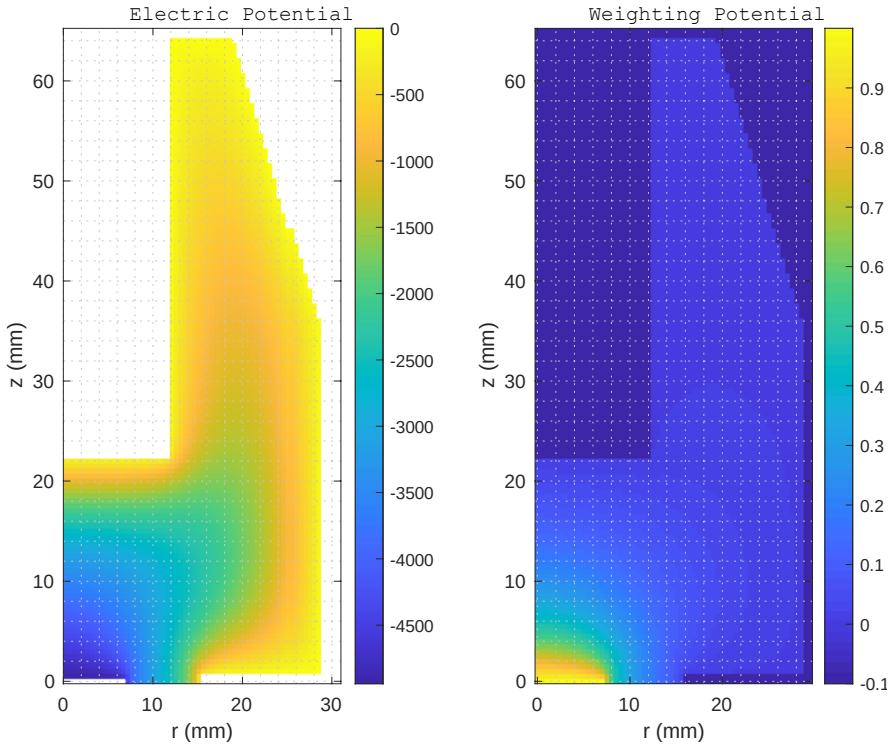

Figure 5.6: An rz slice of the electric potential (Volts) and the weighting potential calculated by ADL for the GSW 120 SAGe well detector.

The weighting potential calculated by ADL when the p+ contact is set to 1 V and 0 V for the n+ contact reveals that in the bulk detector volume, the potential is very weak with the only exception of the immediate area surrounding of the p+ contact.

5.2.1.2 ADL Signal Simulation

The ADL takes the position and energy of the interaction as input. The charges created in the active detector material in the simulation are given a defined time step as they travel through the calculated electric field in the volume to induce a signal in the electrodes. The charge carriers' transit to the electrodes is dependent on the impurity concentration of the detector material, the detector geometry and the bias voltage. The ADL employs the 5th-order Runge Kutta integration method to implement the routine that calculates the path taken by the charge carriers [Bru16]. A weighting field is evaluated for the location of electrons and holes for every time step. It then multiplies the charge created at each interaction to the difference between the evaluated electrons and holes position weighting field to get the signal produced for each interaction. The reader is referred to [Bru16] for detailed explanation of the ADL process.

5.3 Coincidence Scan and ADL Charge Pulse Characterisation Results

The coincidence scan results for gamma-ray interactions that deposited 374 keV in the SAGe well detector and 288 keV in the BGO detector are analysed in this section. This analysis is aimed at establishing the dependence of the measured charge pulses' characteristics on the interaction position in the active SAGe well detector volume. The signal pulses are simulated in ADL for each coincidence measurement coordinate positions.

In order to establish the aforementioned relationship, the signal pulse shape is investigated and risetime calculated. The charge collection time for each of the positions is also examined.

5.3.1 Interaction Position and Charge Carrier Drift Path

The positions in the detector coordinate frame that are investigated for the charge pulse characterisation in the coincidence scan is overlain on the slice of the electric

and weighting potentials that was previously shown in Figure 5.6. These positions are shown as 21 black dots on both the electric and weighting potentials in Figure 5.7. Two profiles are examined for the pulse characteristics: Profile 1 and Profile 2. All points on Profile 1 lie on the same depth plane in the detector relatively close to the p+ contact at z = 6 mm while Profile 2 points lie on the same radial line at various z positions. Profile 1, labelled R1 – R4, is used to investigate the radial dependence of the charge pulse characteristics while, Profile 2, labelled D1 – D7, is used to establish any depth dependency of the charge pulse characteristics. The coordinates of R1 – R4 and D1 – D7 are given in Table 5.1. R3 and D1 are the same points investigated as part of the radial and depth dependency of pulse shapes on interaction positions.

Table 5.1 Coordinates in the SAGe well detector frame of positions R1-R4 and D1-D7.

Position	x (± 0.5 mm)	y (± 0.5 mm)	z (± 0.5 mm)
R1	0.0	9.0	6.0
R2	0.0	15.0	6.0
R3/D1	0.0	19.0	6.0
R4	0.0	25.0	6.0
D2	0.0	19.0	16.0
D3	0.0	19.0	26.0
D4	0.0	19.0	34.0
D5	0.0	19.0	44.0
D6	0.0	19.0	51.0
D7	0.0	19.0	59.0

On the weighting potential map in Figure 5.7, the path of the electrons (white lines) and holes (red lines) are shown as the charge carriers drift to their respective collecting electrodes. It is seen on this potential map that the holes drift towards the p+ contact following a common trajectory. This common trajectory (potential valley) between the well surface and the outer surface of the detector lies at approximately r ≈ 18 mm and r ≈ 19 mm. The electrons however, drift towards the closest part of the n+ contact. The weighting potential is near zero everywhere in the entire volume of the detector

except at the region near the p+ electrode below z < 15 mm. From the figure, only position R1 lies within an area where the weighting potential is considerably higher compared to other interaction positions analysed.

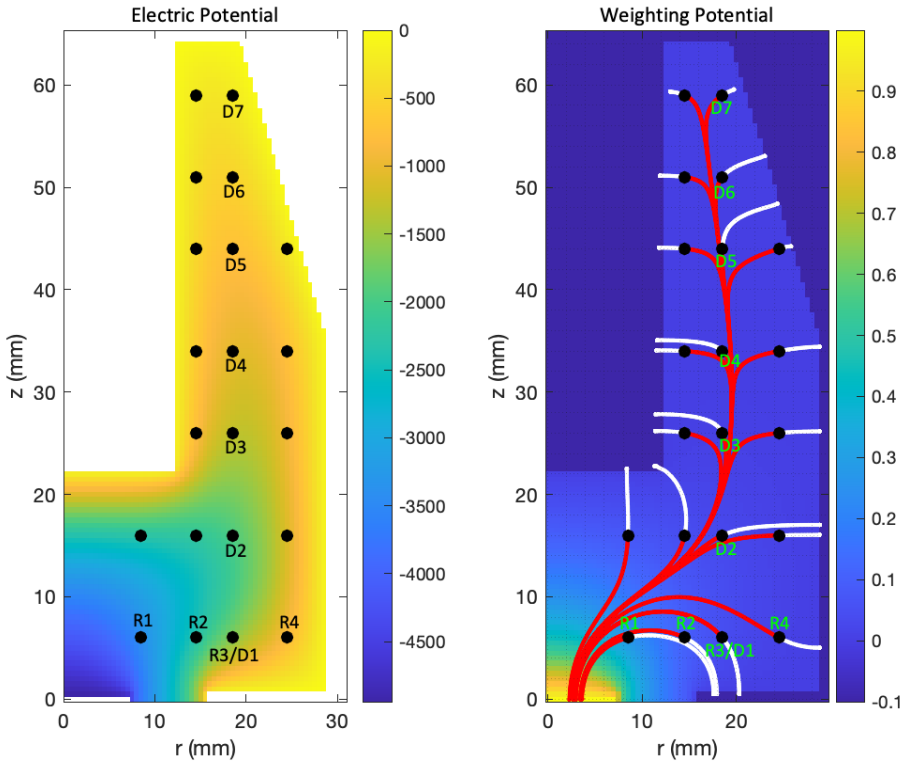

Figure 5.7: All 21 coincidence scan positions (black dots) superimposed on the ADL simulated electric (left) and weighting (right) potentials are marked with black circles. The holes (red) and electrons (white) trajectories for all positions are shown on the weighting potential map. Radial (R1 – R4) and depth (D1 – D7) are positions analysed.

5.3.2 Measured and Simulated Signal Pulse.

In Figure 5.8, the signal pulses simulated with ADL (top) and experimentally measured (bottom) from the coincidence scan of the detector are presented. The positions for each of the pulses corresponds to the positions listed in Table 5.1 with the exception of position D7. Though the signal pulse for this position has been simulated and presented here, that of coincidence scan for this position is conspicuously missing in the pulse plots. Repeated measurements at this position yielded no coincidence pulse. One plausible reason that can explain this lack of coincidence pulse is the thickness of the germanium crystal measured from the direction of the incident photons. This position is ~6 mm from the crystal top that is tapered off to a thickness of ~10 mm

resulting in a crystal thickness of <5 mm with respect to the photon direction and position D7. This potentially reduces the probability of interactions and coincidence events at the top end of the crystal.

The pulses for Profile 1 positions are shown with dashed lines for both simulated and measured detector response except for R3 which is shown as a solid line along with Profile 2 pulses since this position is also investigated for depth dependency. These pulses show a sequence consistent with increasing radial and/or depth positions for both the simulated and measured detector response.

The pulse shapes for the radial profile of R1 and R2 exhibit a steep rise while the leading edge of pulse shapes for positions R3 and R4 are slightly slower compared to R1 and R2. Also, analysis of pulse shapes for interactions in the depth profile positions D1 to D6 (excluding D7 since no measured information exist) show that pulses for positions D3 to D6 have very similar shapes with its rising edge much slower than positions D1 and D2. Pulse shapes for positions D3 to D6 represents the expected shapes for all interactions that occur above the detector well's base.

There is an obvious variation in signal pulse shape as a function of radial interaction position for Profile 1. Whereas in Profile 2, non or slight observable differences exist in the pulse shapes for D3 to D6. Qualitatively, the simulated pulse shape and the measured pulse shape show the same behaviour.

Matching the pulse shapes observed in Figure 5.8 to the interaction positions in Figure 5.7, the shape of the pulses can be described as a function of potential distribution in the detector active volume. The pulses from the radial profile lie in the region where the potential is relatively changing linearly with radius whereas, Profile 2 (D1 to D6) lies in a weak potential region compared to the potential near the p+ contact.

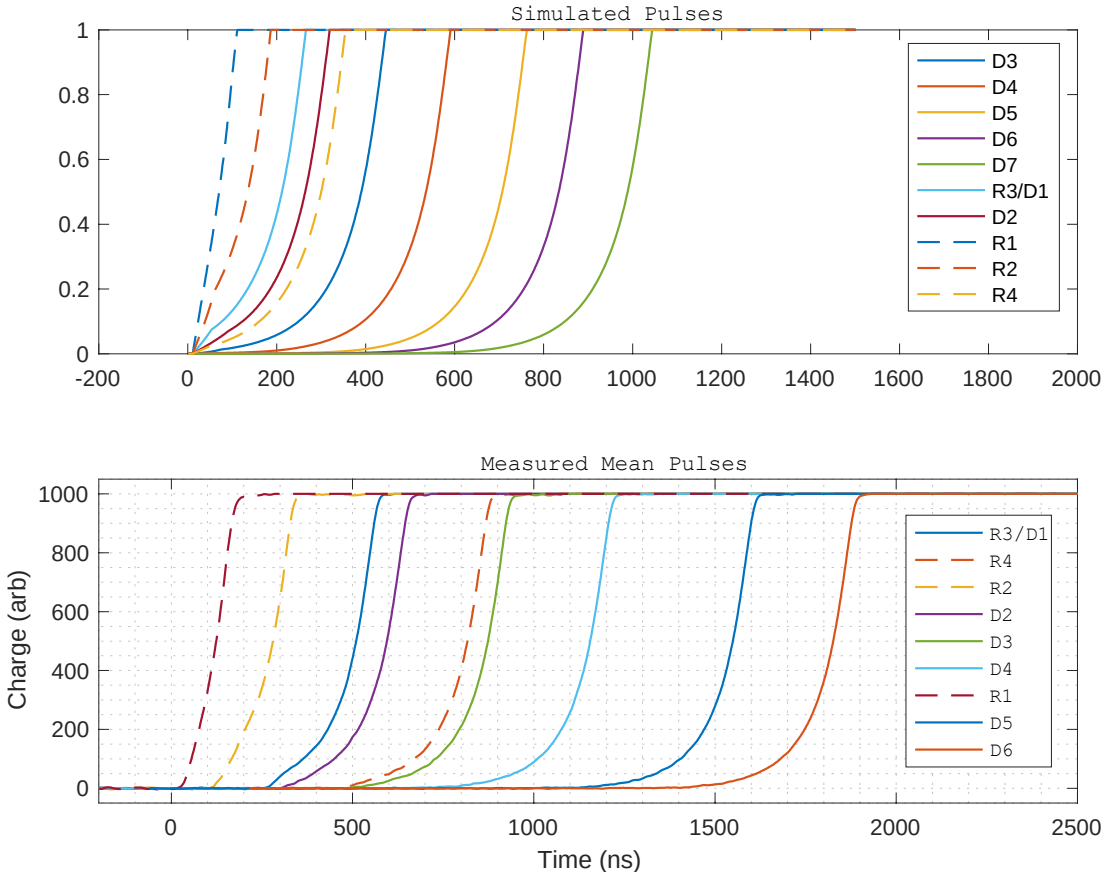

Figure 5.8: Simulated signals (top panel) using ADL and experimental mean signals (bottom panel) for selected positions investigated during coincidence scan measurement. The positions specified by the legends are given in Table 5.1.

5.3.3 Rise Time and Charge Collection Characteristics

The rise times of induced signals on the electrodes by the charge carriers and the charge carriers' collection times for the interactions that occurred at the positions described in Section 5.3.1 will now be investigated.

Five rise times have been calculated for corresponding mean signal pulses for positions of R1 to R4 and D1 to D6. The rise times calculated are:

- T95_5; time interval between 5% and 95% of maximum pulse
- T90_5; time interval between 5% and 90% of maximum pulse
- T90_10; time interval between 10% and 90% of maximum pulse
- T30_10; time interval between 10% and 30% of maximum pulse
- T30_5; time interval between 5% and 30% of maximum pulse

The rise times of measured mean signals calculated are tabulated in Table 5.2 and those from ADL simulated pulses are presented in Table 5.3. Included in each table is the charge drift times for charges from the point of its creation to the electrodes. The general observation of the rise times calculated from measured signal pulses and ADL show that the ADL simulated signals' rise times are lower than the measured value.
The T30_5 and T95_5 risetime are analysed here to understand the pulse characteristics. Both rise times increased with increasing distance radially and with increasing depth except for when position D1 and D2 are compared to each other. The rise time of position D2 is slightly lower than that of D1 because, a closer look at the potential shows the electric potential gradient at point D2 is slightly higher than that at position D1. The T95_5 rise time and the corresponding T30_5 rise time for the mean signal measured are plotted in Figure 5.9. The error in the rise time measurement is assumed to be less than 5 ns: that being the digitised sample size.

Table 5.2: Experimentally measured charge pulse rise time and BGO – SAGe Well trigger time difference. A maximum of 5 ns error is assumed for the rise times.

Position	T95_5 (ns)	T90_5 (ns)	T90_10 (ns)	T30_10 (ns)	T30_5 (ns)	Time difference (ns)
R1	134	124	112	40	52	602
R2	194	186	164	74	96	652
R3/D1	262	254	198	104	160	734
R4	274	266	200	106	172	882
D2	254	256	198	102	160	776
D3	268	260	198	104	166	913
D4	274	266	198	102	170	1051
D5	272	264	198	102	168	1249
D6	272	264	196	102	170	1387
D7	-	-	-	-	-	-

The results for the rise times show that it is dependent on the radial interactions position (R1 to R4) especially for positions close to the p+ contact where the potential is high. The rise time measured for the depth profile under consideration show position dependency for depths D1 and D2. The interactions at positions D3 to D6 has

not revealed any position sensitivity. Again, these findings can be explained using Figure 5.7 as a reference.

Table 5.3: Charge collection and charge pulse rise times from ADL simulation. A maximum of 2 ns error is assumed for the rise times.

Position	T95_5 (ns)	T90_5 (ns)	T90_10 (ns)	T30_10 (ns)	T30_5 (ns)	Charge collection time (ns)
R1	91	87	80	24	31	112
R2	159	154	140	55	69	187
R3/D1	221	217	181	93	129	266
R4	247	243	186	97	154	355
D2	245	240	188	99	151	320
D3	255	250	188	99	161	446
D4	255	250	188	99	161	591
D5	256	251	188	99	162	763
D6	256	251	188	99	162	890
D7	255	251	188	98	161	1044

The radial profile, R1 to R4 lie on a plane close to the p+ contact and as such the charge carriers created in this region are in a potential field greater than that of charge carriers produced in the bulk of the detector volume. Electrons and holes produced at positions R1, R2, and R3 both have significant contribution to the signal shape observed. For position R4, electrons are quickly collected at the n+ contact close by but the holes have to drift to the region where the potential is significantly high before being sensed at the p+ contact. This argument also suffices for the depth profiles examined. Apart from positions D1 and D2, where the events occur in a region of considerable high potential with respect to the detector volume excluding the immediate vicinity of the p+ contact, D3 to D6 events occur in a near zero potential region. The electrons contribute less to the overall signal characteristics observed because they are quickly collected at the n+ contact but the holes follow a path (potential valley) contributing very little response on the p+ contact until it approaches the region (z = 15 mm) where the potential is high.

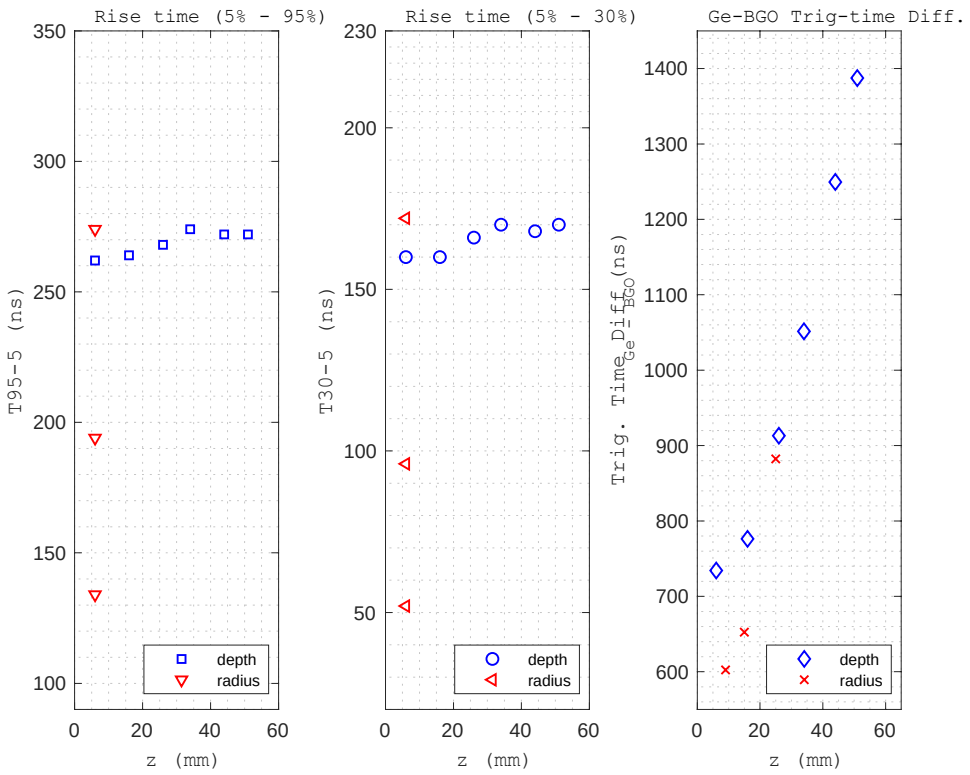

Figure 5.9: Rise time and SAGe well – BGO time difference as a function of gamma-ray interaction position in the detector. The rise time is more sensitive to radial position changes than depth. The time difference is a function of interaction distance to the electrodes. An error less than 10 ns is assumed.

To further support the foregoing arguments, T30-10, T30-5, T90-10 and T90-5 rise times for all the coincidence scan interaction points shown in Figure 5.7 are plotted in Figure 5.10. These gives rise time for different axial depth profiles on 9 mm, 15 mm, 19 mm and 25 mm radii separations. The results show that across the region below the detector well (that is, on a parallel plane less than 20 mm from the p+ contact plane), the rise time is a function of interaction position but there is no significant variation in rise time between different radial positions on the same depth plane in the region above the base of the well.

Similar argument is also presented for the charge collection time in the SAGe well detector. The charge collection time is found to be dependent on the interaction position. The results have shown a time collection of 602 ns to 882 ns for positions R1 to R4 while 734 ns for D1 rising to 1.4 µs for position D6 as indicated on the Ge-BGO Trigger Time difference plot in Figure 5.9. The same observation on the rise time results is also supported by the charge collection time. The charge collection time measured for all the measured coincidence scan point in Figure 5.7 is plotted in Figure

5.11. These has also shown variations within the region close to the p+ contact where the field strength is considerably high compared to the bulk detector.

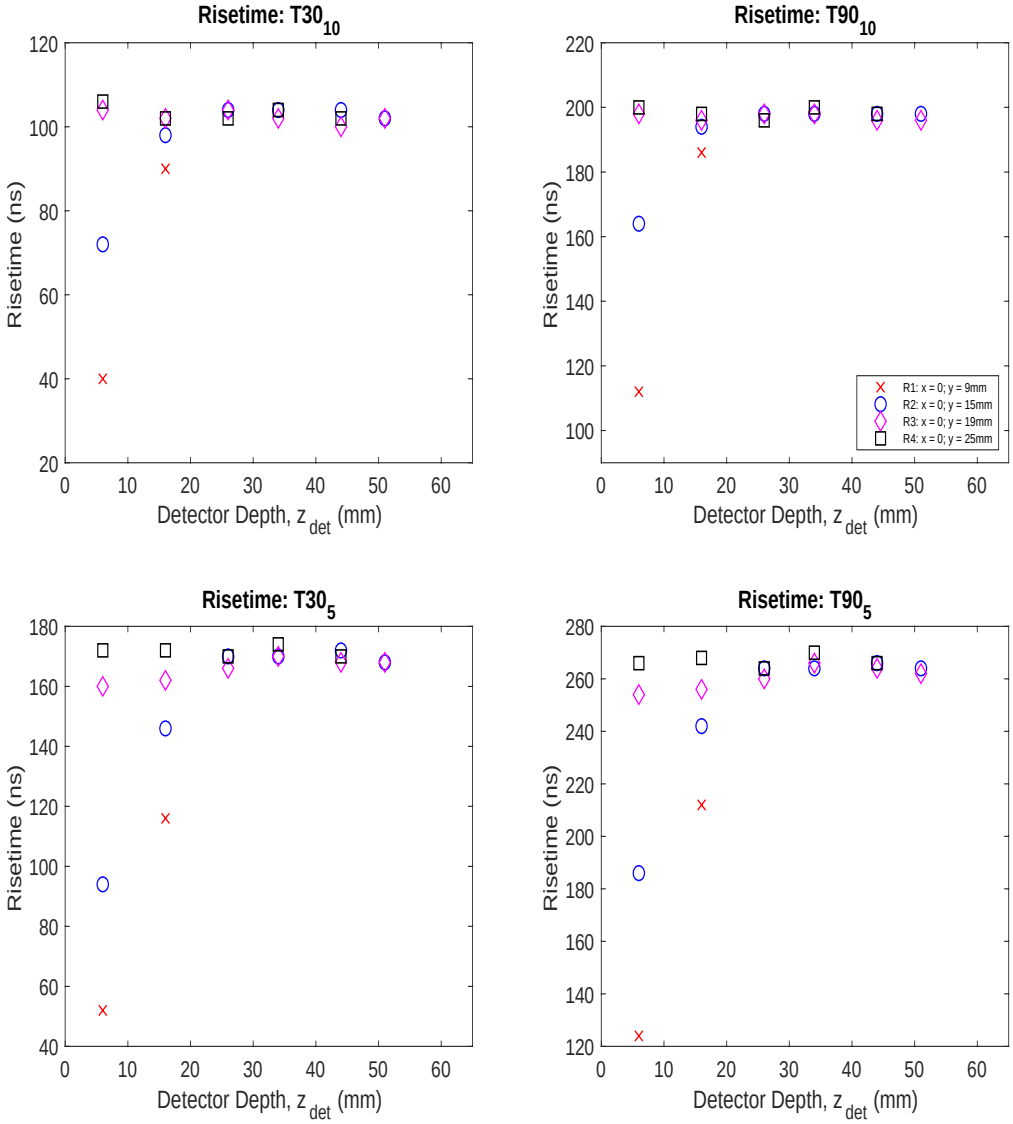

Figure 5.10: Risetime as a function of interaction position inside the detector. As observed with the charge collection time, there is no significant variation in both axial and azimuthal locations except at regions (>20 mm from p+ contact) where the electric and weighting potential inside the detector is high. This is observed for all risetimes measured.

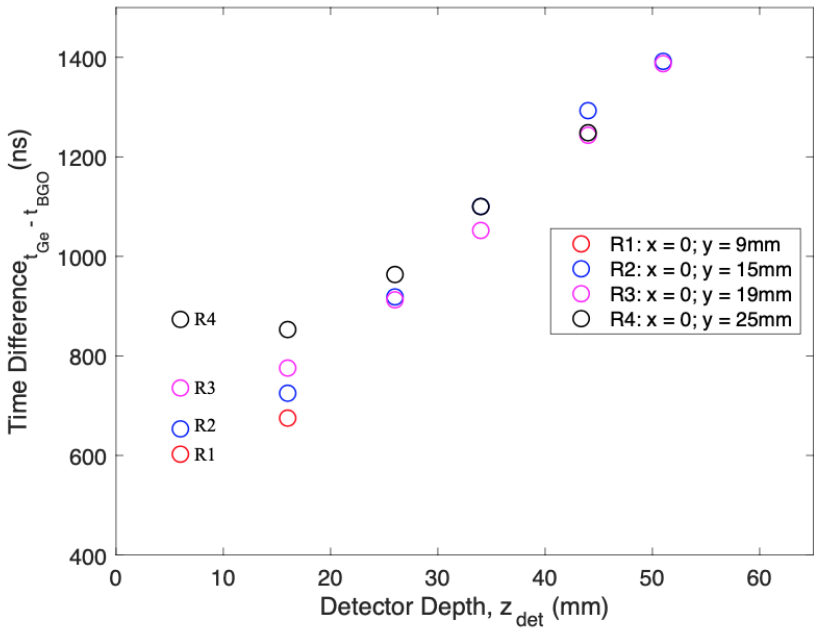

Figure 5.11: BGO – Ge Trigger showing axial and radial variations in the charge collection time in the detector. For interaction positions at the same depth but at different radius, the charge collection time varies significantly at depths near the p+ electrode while very small or no variation is observed near the top of the detector. These observations are attribute to the distribution of the electric field in the detector being strong near the p+ contact region and very weak at the detector top.

Chapter Six

SUMMARY

Well detectors such as the Small Anode Germanium (SAGe) well detector utilised for this body of work, are particularly suitable for environmental nuclear applications where only small samples are available to measure the radionuclide contents of samples. With small sample sizes, higher counting statistics can be achieved by placing the sample in the well for maximum detector coverage. In the case of most environmental samples the radionuclides present decay with the emittance of low energy photons. Measurement of these low energy photons is usually affected by background radioactivity from cosmic sources or other radionuclides' presence in close proximity to the area where the measurement is being carried out. The traditional way of eliminating these background effects on the sample measurements has always been the used of lead shields. However, Compton suppression techniques using secondary detectors have also been developed to veto background events in some nuclear applications. Due to the cost implications of this electronic vetoing system this technique may not be available everywhere.

Characterisation work has been successfully completed in other studies with different types of detectors such as the BEGe in order to study its charge collection and timing properties which can be used to develop a digital Compton / background elimination algorithm.

This characterisation work has now been extended to the SAGe well detector with the aim of understanding its timing properties in order to investigate the feasibility of developing a digital background elimination algorithm for this well detector. The underlying premise is that, for every interaction in the detector active volume, there should exist a unique pulse shape associated to the charges created at that position. For environmental samples placed in the detector well emitting low energy photons, interactions would occur a few millimetres within the crystal surface surrounding the well. Charges created in the bulk volume of the detector would likely be Compton scattered events from gamma-rays external to the sample measured. These can be suppressed if a distinction of pulse shape can be achieved based on interaction position in the active detector volume.

The SAGe well detector properties has been determined experimentally. Simulations of the charge collection and timing properties has also been performed using ADL software package. The results of these experimental measurements and simulations presented in Chapters Four and Five are summarised in this chapter.

6.1 SAGe Well Detector Resolution and Efficiency Performance

The energy resolution measurement has reinforced the claims of the manufacturer for the SAGe well having excellent energy resolution due to the "point-like" p+ contact. The "point-like" p+ contact technology reduces the capacitive noise addition to the detector, hence the excellent resolution measured. The FWHM energy resolution performance for a 47 keV gamma photon is measured to be 0.59 keV, 0.71 keV for 122 keV gamma-rays and 1.77 keV for 1332 keV photons. The effect of this excellent resolution performance can be seen in Figure 3.3 as the complex ^{152}Eu energy spectra clearly shows all the fine energy peaks. The implication of this resolution performance is its ability to resolve closely spaced gamma-rays and therefore facilitating the identification of radionuclides with such gamma-ray signature.

The SAGe well detector has also shown high energy efficiency especially for low energy gamma-rays that are of importance in environmental measurement. The measurement efficiency analysis shows that small samples at the bottom of the detector well have a much better efficiency response than when the detector well is filled: $(59.5 \pm 1.4)\%$, $(64.6 \pm 2.4)\%$ and $(89.9 \pm 0.6)\%$ for 32 keV, 47 keV and 60 keV respectively at 0.65 mm decreasing to $(48.4 \pm 2.5)\%$, $(55.6 \pm 4.8)\%$ and $(67.3 \pm 1.2)\%$ for 32 keV, 47 keV and 60 keV respectively at a sample height of 3.5 cm. SAGe well also performs better than plana detectors such as BEGe detector for small sample well; for example a 5 g sample in the well has an absolute efficiency of (48.4 ± 2.5)%, (55.6 ± 0.4.8)%, (67.3 ± 1.2)% for 32 keV, 47 keV and 60 keV respectively, whereas, the BEGe's absolute efficiency is (7.26 ± 0.24)%, (13.7 ± 0.55)%, and (14.2 ± 0.29)% for 32 keV, 47 keV and 60 keV respectively for the same mass of sample. However, when the measurement is for a sample large enough not to fit into the well, then measurements using another type of detector such as a BEGe detector, if available, may be desirable. This is particularly important for low energy measurements considerations. For low energy gamma-ray measurements, compared

to BEGe detector efficiency, the SAGe well detector performance is poor when the measurement is performed on the endcap. For a 40 g sample, the net to gross area ratio of a 32 keV gamma ray is 39% for SAGe compared to 76% for the BEGe detector. Efficiency measurements for the low energies in this work have shown the BEGe having more than double the absolute efficiency performance of the SAGe well detector when the sample is placed on the detector endcap: (7.01 ± 0.16)%, (8.38 ± 0.33)%, (9.60 ± 0.19)% for 32 keV, 47 keV and 60 keV respectively for BEGe and (0.88 ± 0.03)%, (1.96 ± 0.08)%, (3.05 ± 0.06)% for 32 keV, 47 keV and 60 keV respectively for SAGe well. However, for medium to high energy (662 keV to 1332 keV) measured in this work, the SAGe well absolute efficiency as measured from the end cap, is comparable to the BEGe detector absolute efficiency value. These observations in the absolute efficiency performance can be explained as due to the optimisation of the BEGe detector's end cap with a carbon entrant window, allowing for low energy penetration. Whereas, for the SAGe well detector, the end cap is made of 1 mm thick aluminium material and a 0.5 mm thick lithium n+ contact facilitating the attenuation and absorption of low energy photons.

6.2 Ambiguity in SAGe well Signal Pulse Discrimination

The geometry of the SAGe well detector (Figures 3.1 and 3.5), the electric field and the weighting potential introduces an ambiguity to the discrimination of the signal pulse shape based on gamma-ray interaction position in the active volume of the detector. This ambiguity arises from:

- the charge carrier collecting electrodes configuration
- the weak electric field in the bulk of the detector's active volume relative to the region near the p+ contact (Figure 5.6a).
- the near zero weighting potential in the bulk of the detector's active volume except for within 15 mm radius region around the p+ contact (Figure 5.6b) where it is relatively high but rapidly changes linearly.
- the contributions to the early part of the induced signal pulse shape which is a function of the interaction position. The ambiguity here arises from the fact that either or both charge carriers (electrons and holes) can produce the same

effect in the early part of the induced signal shape during the charge collection process.

The effects of all these ambiguities listed above is such that interactions of gamma-rays in different regions in the active volume of the SAGe well detector can induce signals having the same or intermediate pulse shape. The ambiguity is seen in the risetime measurements for the profiles analysed in this work. As an example, the experimentally measured rise times at positions R4, D3 to D6 (refer to Figures 5.7 for position and Tables 5.2 and 5.3 for rise times) are about the same even though R4 lies in a different region in the detector volume. The induced signals from these positions cannot be distinguished based on the interaction position in the detector.

6.3 Conclusion

The SAGe well detector is quite suitable for small sample measurements with samples placed inside the detector's well to achieve a high efficiency performance enjoyed by well detectors due to the near 4π counting efficiency. The energy resolution of the SAGe well detector is in agreement with values reported by the manufacturer.

The characterisation of the SAGe well was aimed at a possibility of extending the measurement capability of the SAGe well detector by relying on selective pulse shape discrimination to develop a digital Compton suppression algorithm. The success of this would have led to the suppression of background events without the need of the traditional lead shields.

However, the pulse shape analysis shows that selective elimination of events cannot be achieved due to the ambiguity earlier discussed.

It is therefore recommended to continue using lead shielding for measurement with the SAGe well detector.

APPENDIX A

Data Acquisition System Settings

The user input settings for the Field Programmable Gate Array (FPGA) filter used for the digital data capture in the digital pulse processing (DPP) explained in Section 3.8 of this thesis are presented in Table A1. These values are tuned for best digitising performance that preserves the resolution of the energy spectrum.

Table A1: FPGA filter settings for digital data acquisition system.

Parameters	Value
Trapezoid Rise Time (ns)	385
Trapezoid Flat Top (ns)	200
Peak Averaging Window (ns)	64
Peak hold off (ns)	16
Averaging Window (ns)	45
Input Risetime (ns)	50
Decay time (ns)	4300
Peaking time (ns)	100
Digital Gain	3
Threshold	60
BaseLine Averaging Window	6
Trigger Width	50
Pre-Trigger	256
Baseline holdoff	173
Decimation	0

A.1 Canberra model 2002C charge-sensitive preamplifier

A block diagram which illustrates the layout of the Canberra model 2002C charge-sensitive preamplifier attached to the SAGe well detector is shown below.

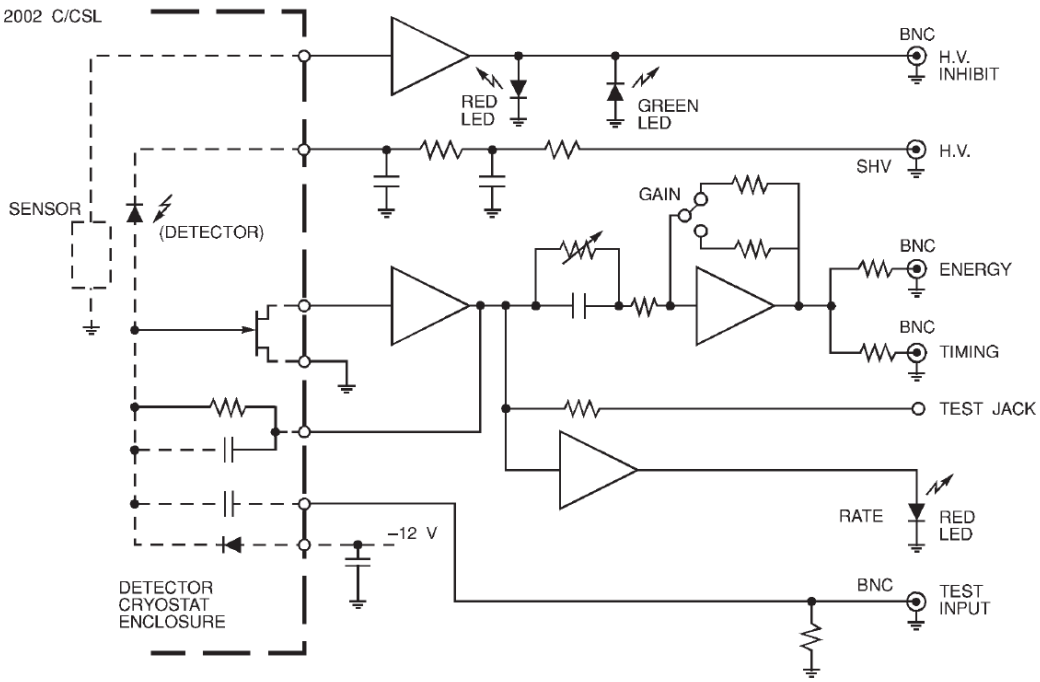

Figure A.1: Block diagram showing the components of the Canberra 2002C charge sensitive preamplifier module on the SAGe well detector. The diagram also shows the various input and outputs leads of the preamplifier including monitor indicators for safe operation of the detector.

This preamplifier has gain settings of x1 and x5. The gain setting of x5 is particularly important for low energy measurements where electronic noise tends to affect the measured detector pulse signal. The system gain and noise performance measurements are presented in Chapter five of this thesis.

APPENDIX B

SOURCE INFORMATION

The source information used for measurements carried out in this research work a tabulated below.

Table B1: NPRL source information used for FWHM measurement.

Radionuclide	NPRL no.	Activity (kBq)
^{241}Am	466	179
^{60}Co	504	37
^{137}Cs	192	164
^{152}Eu	461	119

Table B2: Nuclear data for ERRC standards as at 16th May 2003.

Radionuclide	Gamma Peaks keV	Yield	Half life years	Half life days
^{137}Cs	661.66	0.851	30.07	10983.07
	36.58	0.058		
	32.06	0.013		
^{210}Pb	46.50	0.0425	22.26	8130
^{241}Am	59.54	0.359	432.2	157861.1
^{60}Co	1173.24	0.9997	5.2714	1925.379
	1332.50	0.9999	5.2714	1925.379
^{109}Cd	88.04	0.0361	1.267	462.6
^{139}Ce	165.86	0.800	0.377	137.64
^{57}Co	122.06	0.856	0.744	271.79
	136.47	0.1068		
^{203}Hg	279.20	0.81	0.128	46.612
^{113}Sn	391.69	0.64	0.315	115.09
^{85}Sr	514.01	0.957	0.178	64.84
^{88}Y	898.04	0.927	0.292	106.65
	1836.06	0.9935	0.292	106.65

Table B3: Calibrated activities of LCW well detector standards as at 16th May 2003.

Nuclide	LCW1 (1.667 g) Activity		LCW2 (1.659 g) Activity		LCW3 (1.703 g) Activity		LCW4 (1.633 g) Activity		LCW5 (1.623 g) Activity		LCW6 (1.654 g) Activity	
	Bq kg^{-1}	±	Bq kg^{-1}	±	Bq kg^{-1}	±	Bq kg^{-1}	±	Bq kg^{-1}	±	Bq kg^{-1}	±
^{137}Cs	1199.9	25.0	1183.0	24.6	1195.2	24.9	1171.6	24.4	1174.5	24.5	1178.6	24.5
^{210}Pb	4663.2	179.1	4597.7	176.6	4645.0	178.4	4553.4	174.9	4564.7	175.3	4580.6	176.0
^{241}Am	1284.2	25.1	1266.1	24.7	1279.2	25.0	1253.9	24.5	1257.0	24.5	1261.4	24.6
^{60}Co	1584.0	35.2	1561.8	34.7	1577.9	35.0	1546.8	34.4	1550.6	34.4	1556.0	34.6
^{109}Cd	3348.0	125.0	3300.9	123.2	3334.9	124.5	3269.1	122.0	3277.2	122.3	3288.7	122.8
^{139}Ce	27.6	0.7	27.2	0.6	27.5	0.7	26.9	0.6	27.0	0.6	27.1	0.6
^{57}Co	68.2	1.5	67.2	1.4	67.9	1.5	66.6	1.4	66.7	1.4	66.9	1.4
^{113}Sn	51.4	1.1	50.7	1.1	51.2	1.1	50.2	1.0	50.3	1.0	50.5	1.1
^{85}Sr	6.0	0.1	6.0	0.1	6.0	0.1	5.9	0.1	5.9	0.1	5.9	0.1
^{88}Y	172.5	3.0	170.1	3.0	171.8	3.0	168.4	2.9	168.8	2.9	169.4	2.9

Table B4: Attenuation coefficients for ERL powdered well standards.

Energy (keV)	Attenuation coeff. ($cm^2\ g^{-1}$)
32.06	0.3283
36.58	0.2820
46.50	0.2317
59.54	0.2028
88.03	0.1757
122.06	0.1588
136.47	0.1534
165.83	0.1445
391.69	0.1062
514.00	0.0950
604.71	-
661.66	0.0851
795.87	-
898.70	0.0739
1173.24	0.0648
1332.50	0.0607
1836.08	0.0513

APPENDIX C

Data Information

The data used for discussions and plots in this thesis are presented here.

Table C1: Calibrated activities of LCW well detector standards (calibration date 16th May 2003).

	LCW1 Bq kg^{-1}	err ±	LCW2 Bq kg^{-1}	err ±	LCW3 Bq kg^{-1}	err ±	LCW4 Bq kg^{-1}	err ±	LCW5 Bq kg^{-1}	err ±	LCW6 Bq kg^{-1}	err ±
^{137}Cs	1200	25	1183	25	1195	25	1172	24	1175	25	1179	25
^{210}Pb	4663	179	4598	177	4645	178	4553	175	4565	175	4581	176
^{241}Am	1284	25	1266	25	1279	25	1254	26	1257	25	1261	25
^{60}Co	1584	35	1562	35	1578	35	1547	34	1551	34	1556	35

Table C2: Decay Corrected Calibrated Activities (22nd March 2017).

	LCW1 Bq kg^{-1}	err ±	LCW2 Bq kg^{-1}	err ±	LCW3 Bq kg^{-1}	err ±	LCW4 Bq kg^{-1}	err ±	LCW5 Bq kg^{-1}	err ±	LCW6 Bq kg^{-1}	err ±	mean	err ±
^{137}Cs	871	18	859	18	868	18	851	18	853	18	856	18	860	11
^{210}Pb	3027	116	2985	115	3015	116	2956	114	2963	114	2974	114	2987	70
^{241}Am	1256	25	1238	24	1251	24	1226	24	1229	24	1234	24	1239	15
^{60}Co	256	6	252	6	255	6	250	6	250	6	251	6	252	3

Table C3: Sample height and its mass equivalent.

Sample height (cm)	0.65	1.1	1.5	2.0	2.5	3.0	3.50
Mass (g)	0.779	1.374	1.890	2.526	3.210	3.858	4.489

Table C4: SAGe well energy efficiency for samples filled to a height of 4 cm in six different sample vials (labelled LCW1 to LCW6) with a 1 cm diameter.

	Efficiency													
Energy	LCW1	±	LCW2	±	LCW3	±	LCW4	±	LCW5	±	LCW6	±	mean	±
32.06	0.479	0.016	0.441	0.015	0.458	0.015	0.484	0.016	0.477	0.016	0.478	0.016	**0.469**	0.006
46.50	0.524	0.021	0.535	0.021	0.508	0.020	0.526	0.021	0.555	0.022	0.520	0.021	**0.528**	0.009
59.54	0.627	0.013	0.608	0.012	0.617	0.013	0.610	0.012	0.593	0.012	0.607	0.012	**0.610**	0.005
661.66	0.104	0.003	0.102	0.003	0.104	0.003	0.109	0.003	0.102	0.003	0.104	0.003	**0.104**	0.001
1173.24	0.035	0.002	0.037	0.002	0.038	0.002	0.037	0.002	0.042	0.002	0.037	0.002	**0.038**	0.001
1332.5	0.040	0.002	0.035	0.003	0.037	0.002	0.037	0.002	0.036	0.003	0.035	0.002	**0.037**	0.001
Mass (g)	**1.667**		**1.659**		**1.703**		**1.633**		**1.623**		**1.654**		**1.657**	

Table C5: SAGe Well detector energy efficiency dependence on sample fill height (volume) in a 1.6 cm diameter sample vial.

Energy (keV)	Yield	Height (cm)													
		0.65	±	**1.1**	±	**1.5**	±	**2.0**	±	**2.5**	±	**3.0**	±	**3.5**	±
32.06	0.0580	0.5955	0.0148	0.5790	0.0166	0.5771	0.0196	0.5705	0.0212	0.5472	0.0227	0.5298	0.0245	0.4839	0.0253
46.5	0.0425	0.6456	0.0242	0.6335	0.0286	0.6208	0.0330	0.6002	0.0376	0.5994	0.0422	0.5778	0.0455	0.5557	0.0479
59.54	0.3590	0.8989	0.0062	0.8123	0.0071	0.7784	0.0082	0.7816	0.0094	0.7542	0.0104	0.7179	0.0111	0.6731	0.0116
661.66	0.8510	0.1697	0.0020	0.1538	0.0021	0.1488	0.0023	0.1378	0.0027	0.1313	0.0028	0.1232	0.0030	0.1135	0.0030
1173.24	0.9997	0.0557	0.0006	0.0454	0.0008	0.0488	0.0007	0.0469	0.0008	0.0465	0.0009	0.0428	0.0009	0.0386	0.0010
1332.5	0.9999	0.0489	0.0010	0.0460	0.0010	0.0413	0.0012	0.0409	0.0012	0.0419	0.0011	0.0403	0.0013	0.0366	0.0013
Mass (g)		**0.779**		**1.374**		**1.890**		**2.526**		**3.210**		**3.858**		**4.489**	

Table C6: SAGe well detector efficiency ratio.

Energy (keV)	Height (cm)						
	0.65	1.1	1.5	2	2.5	3	3.5
32.06	1	0.972	0.969	0.958	0.919	0.890	0.813
46.50	1	0.981	0.962	0.930	0.928	0.895	0.861
59.54	1	0.904	0.866	0.870	0.839	0.799	0.749
661.66	1	0.906	0.877	0.812	0.774	0.726	0.669
1173.24	1	0.814	0.875	0.842	0.834	0.769	0.693
1332.50	1	0.940	0.845	0.837	0.857	0.823	0.748

Table C7: FWHM values of full energy peaks from analogue, moving window deconvolution (MWD) and baseline difference energy calculation method. Estimated errors for these measurements are about 2%.

Energy (keV)	Analogue (keV)	MWD (keV)	BLD (keV)
46.50	0.59	0.68	0.69
59.54	0.62	0.71	0.73
121.78	0.71	0.92	0.83
244.70	0.88	1.02	0.98
344.28	1.02	1.12	1.19
443.97	1.08	1.24	1.28
661.67	1.31	1.49	1.70
778.90	1.41	1.57	1.75
964.10	1.52	1.76	2.01
1112.07	1.67	1.91	2.13
1332.50	1.77	2.05	2.30
1408.01	1.86	2.09	2.59

Table C8: Absolute efficiency results of 5 g mass in 4 cm diameter sample holder placed on detector face.

mass (g) 5.04 ± 0.01				Count rate				abs eff (%)			
Energy (keV)	Yield	Activity (Bq)	.+/-	SAGe	.+/-	BEGe	.+/-	SAGe	.+/-	BEGe	.+/-
32.06	0.0580	0.241	0.005	0.002	0.001	0.018	0.001	1.01	0.08	7.26	0.24
46.50	0.0425	0.609	0.023	0.016	0.001	0.084	0.001	2.67	0.13	13.73	0.55
59.54	0.3590	2.205	0.043	0.089	0.001	0.314	0.002	4.04	0.09	14.23	0.29
661.66	0.8510	3.539	0.073	0.075	0.001	0.089	0.001	2.12	0.05	2.52	0.06
1173.24	0.9997	1.078	0.024	0.014	0.001	0.014	0.001	1.28	0.05	1.31	0.05
1332.50	0.9999	1.078	0.024	0.014	0.001	0.012	0.001	1.31	0.05	1.11	0.04

Table C9: Absolute efficiency results of 10 g mass in 4 cm diameter sample holder placed on detector face.

mass (g) 10.08 ± 0.03				Count rate				abs eff (%)			
Energy (keV)	Yield	Activity (Bq)	.+/-	SAGe	.+/-	BEGe	.+/-	SAGe	.+/-	BEGe	.+/-
32.06	0.0580	0.483	0.010	0.006	0.001	0.037	0.001	1.26	0.06	7.70	0.21
46.50	0.0425	1.218	0.047	0.033	0.001	0.140	0.001	2.72	0.12	11.52	0.46
59.54	0.3590	4.411	0.086	0.193	0.002	0.541	0.001	4.37	0.09	12.26	0.25
661.66	0.8510	7.080	0.147	0.150	0.001	0.149	0.001	2.11	0.05	2.10	0.05
1173.24	0.9997	2.156	0.048	0.025	0.001	0.024	0.001	1.13	0.04	1.12	0.04
1332.50	0.9999	2.156	0.048	0.029	0.001	0.020	0.001	1.33	0.04	0.90	0.03

Table C10: Absolute efficiency results of 20 g mass in 4 cm diameter sample holder placed on detector face.

mass (g) 20.20 ± 0.04				Count rate				abs eff (%)			
Energy (keV)	Yield	Activity (Bq)	.+/-	SAGe	.+/-	BEGe	.+/-	SAGe	.+/-	BEGe	.+/-
32.06	0.0580	0.966	0.020	0.008	0.001	0.060	0.001	0.82	0.04	6.23	0.16
46.50	0.0425	2.439	0.094	0.055	0.001	0.275	0.002	2.25	0.09	11.29	0.44
59.54	0.3590	8.834	0.171	0.327	0.002	0.964	0.003	3.70	0.08	10.91	0.21
661.66	0.8510	14.180	0.293	0.269	0.002	0.256	0.002	1.90	0.04	1.80	0.04
1173.24	0.9997	4.318	0.096	0.043	0.001	0.040	0.001	0.99	0.03	0.92	0.03
1332.50	0.9999	4.318	0.096	0.046	0.001	0.040	0.001	1.05	0.03	0.90	0.03

Table C11: Absolute efficiency results of 40 g mass in 4 cm diameter sample holder placed on detector face.

mass (g) 40.23 ± 0.04				Count rate				abs eff (%)			
Energy (keV)	Yield	Activity (Bq)	.+/-	SAGe	.+/-	BEGe	.+/-	SAGe	.+/-	BEGe	.+/-
32.06	0.0580	1.925	0.040	0.017	0.001	0.135	0.001	0.88	0.03	7.01	0.16
46.50	0.0425	4.858	0.187	0.095	0.001	0.407	0.002	1.96	0.08	8.38	0.33
59.54	0.3590	17.594	0.339	0.537	0.003	1.688	0.005	3.05	0.06	9.60	0.19
661.66	0.8510	28.239	0.582	0.433	0.003	0.420	0.003	1.53	0.03	1.49	0.03
1173.24	0.9997	8.598	0.190	0.076	0.001	0.069	0.001	0.89	0.02	0.80	0.02
1332.50	0.9999	8.599	0.190	0.076	0.001	0.064	0.001	0.88	0.02	0.74	0.02

Table C12: MCNP SAGe well detector efficiency simulation for different sample height well.

Energy (keV)	Sample Fill Height (cm)													
	0.65	±	1.1	±	1.5	±	2	±	2.5	±	3	±	3.5	±
32.01	0.6759	0.0170	0.6710	0.0168	0.6662	0.0166	0.6595	0.0164	0.6506	0.0163	0.6367	0.0160	0.6130	0.0160
46.5	0.7998	0.0154	0.7904	0.0149	0.7828	0.0146	0.7733	0.0144	0.7621	0.0143	0.7446	0.0140	0.7159	0.0136
59.54	0.8323	0.0179	0.8210	0.0177	0.8126	0.0174	0.8024	0.0173	0.7900	0.0171	0.7710	0.0170	0.7404	0.0166
661.66	0.1853	0.0100	0.1783	0.0097	0.1725	0.0095	0.1650	0.0093	0.1570	0.0090	0.1485	0.0088	0.1398	0.0085
1332.5	0.0976	0.0057	0.0937	0.0056	0.0905	0.0055	0.0864	0.0053	0.0821	0.0052	0.0776	0.0050	0.0731	0.0048

Table C13: Measurement of photo peak position as a function of detector bias voltage.

	60 keV				662 keV			
HV (V)	Peak Centroid (chan)	Net Count Rate (/sec)	FWHM (chan)	error (%)	Peak Centroid (chan)	Net Count Rate (/sec)	FWHM (chan)	error (%)
5000	1361	129	14.5	0.78	15137	483	30.23	0.29
4900	1361	132	14.75	0.88	15137	482	30.21	0.31
4800	1361	131	14.86	0.93	15137	486	29.97	0.31
4700	1361	129	14.97	0.80	15137	483	29.85	0.31
4600	1361	132	14.41	0.92	15137	482	29.27	0.31
4500	1361	132	14.42	0.80	15134	479	30.17	0.32
4400	1360	132	14.25	0.90	15129	476	30.48	0.32
4300	1359	130	14.06	0.84	15120	484	29.68	0.31
4200	1358	130	14.16	0.82	15100	481	29.99	0.33
4100	1355	131	14.67	0.84	15068	485	29.99	0.32
4000	1350	132	14.63	0.91	15016	483	30.64	0.32
3900	1344	132	15.04	0.83	14951	477	29.39	0.34
3800	1336	133	15.03	0.85	14861	485	30.59	0.32
3700	1327	132	15.45	0.84	14758	475	30.29	0.33
3600	1316	130	16.15	0.84	14639	477	29.52	0.33
3500	1305	131	16.29	0.91	14516	475	30.4	0.34
3400	1292	133	17.42	1.03	14374	478	29.76	0.34
3300	1278	134	17.57	1.01	14222	479	31.62	0.33
3200	1264	132	18.52	0.96	14066	481	30.46	0.30
3100	1248	132	19.37	1.06	13892	474	31.26	0.34
3000	1231	135	19.79	1.00	13699	474	31.91	0.33
2900	1213	132	22.34	0.95	13492	471	31.89	0.33
2800	1191	134	23.79	1.06	13253	471	32.83	0.34
2700	1167	134	25.72	1.09	12988	474	34.83	0.31
2600	1141	136	26.8	1.08	12699	473	36.7	0.32
2500	1112	140	28.53	1.24	12371	472	37.72	0.30
2400	1080	137	31.46	1.39	12020	470	38.88	0.32
2300	1049	133	35.14	1.37	11681	468	41.28	0.33
2200	1017	134	37.39	1.30	11317	460	43.84	0.37
2100	983	132	40.15	1.35	10938	455	46.05	0.33
2000	951	136	41.25	1.55	10591	447	48.32	0.36
1900	917	132	45.78	1.55	10216	443	51.07	0.34

1800	884	137	46.16	1.84	9842	437	53.67	0.34
1700	849	134	49.25	1.88	9465	428	55.33	0.36
1600	809	133	56.62	1.81	9024	415	58.73	0.38
1500	767	133	55.6	1.98	8574	410	61.47	0.39
1400	718	131	61.06	2.19	8022	406	65.87	0.41
1300	654	137	61.64	2.65	7326	390	68.94	0.42
1200	586	137	70.9	2.59	6581	371	74.89	0.51
1100	535	136	73.5	2.81	6025	346	79.59	0.55
1000	488	136	75.79	3.13	5513	328	85.06	0.61

Appendix D

MCNP Simulation Script

The script presented below is a MCNP simulation script for the GSW120 SAGe well detector. This script can be saved in a text format and run on any mcnp platform with little adjustment to match the dimensions of the SAGe well detector's dimension, sample's geometry and size. The script starts after the line.

==========

```
SAGe Well - Al cryostat - 2cm sample
C
C material densities
C m1 =-2.7g/cm3 (Al), m2 = 0.96g/cm3 (C4H6 - poly), m3 = 5.323g/cm3 (Ge)
C  m6 = 0.8g/cm3 (sample matrix)
C
C ########### Define Cells #########
C
6 2 -0.96 -5 7                    imp:pn 1 $ poly sample holder
5 6 -0.835 -8                     imp:pn 1 $ sample matrix
4 1 -2.7 -6 5                     imp:pn 1 $ Aluminum cryostat
3 0 -4 #(-6 5) #(-5 7) #(-8)          imp:pn 1 $ vacuum
2 3 -5.323 -3 4                   imp:pn 1 $ Detector dead layer
1 3 -5.323 (-1 3):(-2 3)              imp:pn 1 $ Detector
45 0 100                          imp:pn 0 $Define world
50 0 -100 #1 #(-3 4) #(-4) #(-6 5) #(-5 7) #(-8) imp:pn 1     $ #11 #12 #25 #30 #35 #40 imp:p 1 $ #(-9 10)
#(-8 9) #(-10) #(-7 8) #(-3 7) #(-2 3) #(-1 2) imp:p 1 $Define world

C
C ########### Define Surfaces #######
C
1 RCC 0 0 0 0 3.4 0 3                 $Define detector
2 TRC 0 3.4 0 0 3.1 0 3 2             $sage tapered end
3 RCC 0 2.4995 0 0 4.001 0 1.0005   $dead layer/detector
4 RCC 0 2.5 0 0 4.001 0 1             $dead layer/vacuum
5 RCC 0 2.8 0 0 3.701 0 0.8           $ Al inner radius
6 RCC 0 2.7 0 0 3.801 0 0.85          $ Al outer radius
7 RCC 0 2.9 0 0 3.501 0 0.7           $polythene holder
```

```
8 RCC 0 2.91 0 0 2 0 0.68              $ sample matrix 2cm --- vary height as desired
9 RCC 0 2.905 0 0 3.5005 0 0.69          $ source round source cell
100 RCC 0 -5 0 0 15 0 5                $Define world

mode p                                 $Photon
C ########### Define Source ########
SDEF CEL 5 POS 0 0 0 AXS 0 1 0 RAD d1 EXT d2 ERG=d3   $ define CELL source
SI1 0 0.69                             $ radial sampling limit for src
SP1 -21 1                              $ radial sampling weight for src
SI2 2.905 6.4055                       $ axial sampling limits for src
SP2 -21 0                               $ axial sampling weight for src
SI3 L 32.01E-3 46.5E-3 59.5E-3 661.66E-3 1.3325
SP3  1 1 1 1 1
C ############ Define Tallies ######
f8:P 1 $ 35 T
e8 0 8191I 1.5                         $0.5 keV bin size
ft8 geb 2.41e-4 1.32e-4                $SAGe detector coeffs
m6 6000 4 1000 6                       $ sample matrix C4H6 – vary composition as desired
m3 32000 1                             $ Ge Detector
m2 6000 2 1000 4                       $ poly (C2H4)
m1 13000 1                             $ Al cyostat
C ####### Define Run Time #############
nps 50000000
=========================================================================
```

References

[Ade15] Adekola, A.S. et al. "*Characteristic performance evaluation of a new SAGe well detector for small and large sample geometries*." 4th International Conference on Advancements in Nuclear Instrumentation Measurement Methods and their Applications (ANIMMA) (2015): p1-7.

[Ade16] Adekola, A.S. *Private Communications*, (2016).

[App92] Appleby, P.G., Richardson, N. and Nolan, P.J., *Self-absorption corrections for well-type germanium detectors.* Nuc. Instr. Meth. Phys. B71:228 – 233. (1992)

[App04] Appleby, P.G. and Piliposian, G.T., *Efficiency corrections for variable sample height in well-type germanium gamma detectors*. Nuc. Instr. Meth. Phys. B225:423 – 433 (2004)

[Ago11] Agostini, M., et al. *Characterization of a broad energy germanium detector and application to neutrinoless double beta decay search in ^{76}Ge.* JINST 6 P04005 (2011)

[Akk12] Akkoyun, S. *et.al*. *AGATA—Advanced Gamma Tracking Array.* Nuc. Instr. Meth. Phys. A668:25 – 58, (2012).

[Bar11] Barrientos, D., et.al., *Characterisation of a Broad Energy Germanium (BEGe) detector*, Nuc. Instr. Meth. Phys. A648:S228 – S231, (2012).

[Baz91] Bazzacco, D., Cederwall, B., Cresswell, J., Duchêne, G., Eberth, J., et. al. *AGATA, Technical Proposal for an Advanced Gamma Tracking Array for the European Gamma Spectroscopy Community*. Gerl, J., and Korten, W., AGATA collaboration, pp.87, (1991).

[Bos09] Boston, A.J., Dimmock, M.R., Unsworth, C., Boston, H.C., Cooper, R.J., Grint, A.N., Harkness, L.J., Lazarus, I.H., Jones, M., Nolan, P.J., Oxley, D.C., Simpson, J. and Slee, M. *Performance of an AGATA asymmetric detector*, Nuc. Instr. Meth. Phys. A604:48 – 52, (2009).

[Bri15] Britton, R. and Davies, A.V. *Characterisation of a SAGe well detector using Geant4 and LabSOCS.* Nuc. Instr. Meth. Phys. A786:12-16, (2015).

[Bru06] Bruyneel, B., Birkenbach, B., and Reiter, P, *Characterization of large volume HPGe detectors. Part I: Electron and hole mobility parameterization.* Nuc. Instr. Meth. Phys. A569:764 – 773, (2006).

[Bru16] Bruyneel, B., Birkenbach, B., and Reiter, P. *Pulse shape analysis and position determination in segmented HPGe detectors: The AGATA detector library.* Eur. Phys. J. A 52: 70, (2016)

[Bel15] Belgin, E.E. and Aycik, G.A. *Derivation of an efficiency-calibration simulation for a well-type HPGe detector using the Monte Carlo approach and analytical techniques*. Radiation Measurements, 73:36-45, (2015).

[Ca13] CAEN Electronics Instrument Manual: *UM2088 DPHA User Manual*, rev.3 – 03 (2013)

[Can04] Canberra Industries Inc, *Model 2002 Spectroscopy Preamplifier*: User's Manual (2004).

[Cre10] Crespi, F.C.L., Vandone, V., Brambilla, S., Camera, F., Million, B., Riboldi, S. and Wieland O., *HPGe Detectors Timing using Pulse Shape Analyis Techniques*. Nuc. Instr. Meth. Phys. A620:299-304, (2010).

[Coo11] Cooper, R.J., Radford, D.C., Hausladen, P.A. and Lagergren, K., *A Novel HPGe detector for Gamma-ray Tracking and Imaging*. Nuc. Instr. Meth. Phys. A665:25-32, (2011)

[Dav52] Davisson, C.M. and Evans, R.D., *Gamma-Ray absorption coefficients,* Rev. Mod. Phys, Vol.24 p79 (1952).

[Dha10] Dhanaraj, G., Byrappa, K., Prasad, V. and Dudley, M., eds., *Springer Handbook of Crystal Growth.* Heidelberg, Springer, (2010).

[Dim09] Dimmock, M.R., *et al*., *Validation of Pulse Shape Simulations for an AGATA Prototype Detector*, IEEE Trans. Nuc. Sci., vol. 56, no. 4, pp. 2415-2425. (2009). doi: 10.1109/TNS.2009.2021842

[Dob05] Dobson, J.L. *The Characterisation and Position Resolution of a Planar Germanium Strip Detector*. University of Liverpool Thesis (2005).

[Eng89] England, J.B.A., Field, G.M. and Ophel, T.R., *Z-identification of charged particles by signal risetime in silicon surface barrier detectors.* Nuc. Inst. Meth. Phys. A280:291-298, (1989).

[Fan47] Fano, U., *Ionization yield of radiations. II. the fluctuations of the number of ions*, Phys Rev, Vol.72, p26 (1947).

[Fur13] Furci, H., Arribére, M., and Guevara, S.R., *Self-shielding corrections in cylindrical samples in gamma spectrometry with germanium well-type detectors.* Nuc. Instr. Meth. Phys. A705:132 – 139 (2013)

[Geo13] Goel, N., Domingo-Pardo, C., Habermann, T., Ameil, F., Engert, T., Gerl, J., Kojouharov, I., Maruhn, J., Pietralla, N., Schaffner, H., *Characterisation of asymmetric AGATA detector using the γ-ray*

imaging scanning technique. Nuc. Instr. Meth. Phys. A700:10–21, (2013).

[Gil08] Gilmore, G. *Practical gamma-ray spectroscopy*. (2008)

[Har14] Harkness-Brennan, L.J. et.al. *An experimental characterisation of a Broad Energy Germanium detector.* Nuc. Instr. Meth. Phys. A760:28-39, (2014).

[Jor93] Jordanov, V. and Knoll, G.F. *Digital Pulse Processor Using A Moving Average Technique*. IEEE Trans. Nuc. Sci. NS-40, pp 764, (1993).

[Jor94] Jordanov, V.T., and Knoll, G.F., Digital synthesis of pulse shapes in real time for high resolution radiation spectroscopy, Nuc. Instr. and Meth. Phys. A345:337-345 (1994).

[Kno10] Knoll, G.F. *Radiation detection and measurement 4th ed*. John Wiley (2010)

[Leo94] Leo, W.R., *Techniques for Nuclear and Particle Physics Experiments: A How-to Approach*. Springer, (1994).

[Lut99] Lutz Gerhard, *Semiconductor Radiation Detectors* first edition. Springer Berlin-Heidelberg-New York (1999).

[Iur18] Iurian, A.R., Millward, G.E., Sima, O., Taylor, A. and Blake, W. *Self-attenuation corrections for Pb-210in gamma-ray spectrometry using well and coaxial HPGe detectors.* Applied Radiation and Isotopes vol.134:151-156 (2018)

[Mi16a] Mirion Technologies (Canberra). *Small Anode Germanium Well Detector.* Available at: URL< https://mirion.s3.amazonaws.com/cms4_mirion/files/pdf/spec-sheets/sage-well-small-anode-germanium-well-detectors.pdf? 1523631429

[Mi16b] Mirion Technologies (Canberra). *Broad Energy Germanium Detectors (BEGe).* Available at: URL<https://www.mirion.com/products/bege-broad-energy-germanium-detect>

[Mi16c] Mirion Technologies (Canberra). Available at: URL<https://www.mirion.com/products/lege-low-energy-germanium-detectors>

[Ord10] Orduna, R.G., et.al, *Pulse Shape Analysis for Background reduction in BEGe detectors.* JRC Scientific and Technical Reports, EUR 24521 EN (2010).

[Ort1] ORTEC, *671 Spectroscopy Amplifier* Available at: URL< https:/www.ortec-online.com/products/electronics/amplifiers/671>

[Ort 2] ORTEC, *ASPEC-927 Dual Input MCB*. Available at: URL<https://www.ortec-online.com/products/electronics/multichannel-analyzers-mca/basic-analog/aspec-927>

[Ort3] ORTEC, *MAESTRO Multichannel Analyzer Emulation Software*. Available at: URL<https://www.ortec-online.com/products/application-software/maestro-mca>

[Owe85] Owens, A. *Spectral Degradation Effects in an 86cm3 Ge(HP) Detector*. Nuc. Inst. Meth. Phys. A238:473-478 (1985)

[Pau94] Pausch, G., Bohne, W. and Hilscher, D. *Particle Identification in Solid-State Detectors by Means of Pulse-Shape Analysis - Results of Computer Simulations*. Nuc. Inst. Meth. Phys. A337:573 – 587, (1994).

[Phi98] Philhour, B. et.al. *Simulations of pulse shape discrimination (PSD) techniques for background reduction in germanium detectors*. Nuc. Instr. Meth. Phys. A403:136-150, (1998).

[Roo50] Van Roosbroeck, W., *Theory of flow of electrons and holes in germanium and other semiconductors*, Bell System Tech. J., vol. 29, pp. 560-607 (1950).

[Sch11] Schlarb, M., Gernhäuser, R., Klupp, S. and Krücken, R. *Pulse shape analysis for γ-ray tracking (Part I): Pulse shape simulation with JASS*. Eur. Phys. J. A 47: 132. (2011)

[Sim19] SIMION®, Scientific Instrument Services, Inc. <url> https://simion.com [accessed on 2th Jan. 2019]

[Spi98] Spieler, H. *Semiconductor Detectors, Part 2, SLUO Lectures on Detector Techniques*, (1998). [Available online: http://www-physics.lbl.gov/~spieler /SLAC_Lectures]

[Sze01] Sze, S.M. *Semiconductor devices physics and technology*, 2nd Edition, Argosy Publishing, (2001).

[Uec14] Uecker, R., *The historical development of the Czochralski method.* J. Cryst. Growth, 401, pp. 7-24, (2014).

[Uns19] Unsworth, C. et.al. *Characterisation of a Small Electrode HPGe Detector.* Nuc. Instr. Meth. Phys. A927:293–300 (2019).

[Var09] di Vacri A., *et al*., "*Characterization of Broad Energy Germanium (BEGe) detector as a candidate for the GERDA experiment*. IEEE Nuclear Science Symposium Conference Record (NSS/MIC), Orlando, FL, 2009, pp.1761-1767.doi: 10.1109/NSSMIC.2009.5402217.

[Wan15] Wang, G., Mei, H., Mei, H. Guan, D. and Yang, G., *High purity germanium crystal growth at the University of South Dakota.* J. Phys.: Conf. Ser. 606 012012, (2015).

[Wer17] Werner, C.J. (ed.), "*MCNP Users Manual - Code Version 6.2*", LA-UR-17-29981 (2017).

[Yac04] Yacobi, B.G. *Semiconductor Materials: An Introduction to Basic Principles*. Kluwer Academic Publishers, New York, Boston, Dordrecht, London, Moscow, (2004).

[Yan15] Yang, G., Mei, H., Guan, Y.T., Wang, G.J., Mei, D.M. and Irmscher, K *Study on the Properties of High Purity Germanium Crystals*. J. Phys.: Conf. Ser. 606 012013, (2015).

[Zeg11] Zeghbroeck, B.V., *Principles of Semiconductor Devices*, (2011). Available at: URL<http://ece-www.colorado.edu/~bart/book/>.

…….. The cup was bitter, but I drank it nonetheless ……

.....concluding this with my favourite quote of all times, “In God I Trust.”

..this was not in any way a “puff of quantum mechanical smoke”, it took years of pains..